Master's thesis

NTNU
Norwegian University of Science and Technology

Leik Bjelland Isdal

Developing 2.5D Nanotopographical *in vitro* Neural Network Recording Platform to Mimic the Physical Environment of the Brain

Master's thesis in Nanotechnology
Supervisor: Prof. Pawel Sikorski
Co-supervisor: PhD(c) Nicolai Winter-Hjelm
June 2021

NTNU
Norwegian University of
Science and Technology

Leik Bjelland Isdal

Developing 2.5D Nanotopographical *in vitro* Neural Network Recording Platform to Mimic the Physical Environment of the Brain

Master's thesis in Nanotechnology
Supervisor: Prof. Pawel Sikorski
Co-supervisor: PhD(c) Nicolai Winter-Hjelm
June 2021

Norwegian University of Science and Technology

NTNU
Norwegian University of
Science and Technology

Abstract

Despite its incredible complexity, the nervous system is a part of the human anatomy that is particularly vulnerable. Neurodegenerative diseases such as Alzheimer's and Parkinson's disease wreak havoc on this vulnerable system, causing irreparable and extensive damage to the ones affected, and casting heavy economical burdens on society. In pursuit of greater insight into detection and treatment of such neurodegenerative diseases in early onset, novel disease model systems are in dire need.

In recent years, advancements within microfabrication and stem cell technologies have given rise to powerful *in vitro* model systems of the human nervous system and its pathologies. By culturing neurons in microfluidic compartments embedded with microelectrode arrays, growth of neural networks can be carried out in controlled environments and network activity recorded and analysed to determine state of function or dysfunction. Critical to the clinical relevance of such model systems is their ability to recapitulate the small-world network architecture of the nervous system – an architecture enabling complex thought but also rapid disease spread. Traditional *in vitro* neural network systems have been based on planar substrates, neglecting the important role of the physical micro- and nanoscale environment of the brain in guiding network organization. Consequently, grown networks have exhibited architecture diverging from the important small-world principles of the nervous system.

In an effort to improve network architecture and, by extension, clinical relevance, this project set out to develop a novel *in vitro* neural network recording platform with nanotopographies mimicking the physical environment of the brain at the nanoscale. A plasma etch based roughening process for nanotopographical structuring of SU-8 resist was established, demonstrating excellent flexibility in achieving a range of nanotopographies by tuning of etching parameters. Nanotopographical SU-8 was further demonstrated to be a viable direct replacement for the previously used planar Si_3N_4 base substrate on neural network recording platforms. Herein, it was proved compatible with bonding of microfluidic structures, and as insulation for electrodeposition of platinum black electrodes and during neural network recording. Crucially, nanotopographies were found to promote clustering of neurons and axon fasciculation, as well as lower synchrony in global network activity – characteristic structural and functional features of small-world networks. While further optimization and investigation with larger sample sizes are needed before definitive conclusions can be drawn, the developed nanotopographical platform have, in conclusion, shown promise in improving clinical potential of *in vitro* neural disease model systems.

Sammendrag

På tross av sin vanvittige kompleksitet er nervesystemet en del av menneskets anatomi som er spesielt sårbar. Nevrodegenerative sykdommer som Alzheimers og Parkinsons forårsaker omfattende og uopprettelig skade hos de som blir rammet, og ut over de emosjonelle kostnadene for individ og familier pålegger det også samfunnet store økonomiske kostnader. Nye sykdomsmodellsystemer trengs sårt i utviklingen av bedre behandling og mer effektiv diagnostisering av nevrodegenerative sykdommer.

De siste årene har fremskritt innen mikrofabrikasjon og stamcelle-teknologier gitt grobunn for kraftige *in vitro*-modellsystemer av det menneskelige nervesystemet og dets patologier. Ved å dyrke nevroner i mikrofluidiske kammer spedd med mikroelektroder kan vekst av nevrale nettverk utføres innenfor kontrollerte rammer, mens målt nettverksaktivitet gir indikasjon på nettverkets tilstand av funksjon eller dysfunksjon. Avgjørende for den kliniske relevansen til slike modellsystemer er deres evne til å gjenskape nervesystemets småverksnettverksarkitektur – arkitektur som muliggjør komplekse tanker, men også rask spredning av sykdom. Tradisjonelt har *in vitro* nevrale nettverks-systemer vært basert på plane substrater, og neglisjert den viktige rollen hjernens fysiske mikro- og nanoskala-miljø spiller i å lede nettverksorganisasjon. Resultatet har vært nettverksarkitektur som har fraveket de viktige småverdensprinsippene i nervesystemet.

I et forsøk på å forbedre nettverksarkitektur, og derav klinisk relevans, satt dette prosjektet som mål å utvikle en ny *in vitro* nevral nettverksplattform med nanotopografier som etterligner hjernens nanoskala fysiske miljø. En plasmaetsingsbasert ruprosess for nanotopografisk strukturering av SU-8-resist ble etablert, og viste utmerket evne til å oppnå en rekke forskjellige nanotopografier ved modifisering av etseparametre. Nanotopografisk SU-8 ble videre vist å kunne erstatte det tidligere brukte plane Si_3N_4-basesubstratet på nevrale nettverksplattformer. Her ble det vist å være kompatibelt med binding av mikrofluidstrukturer, og som isolasjon for elektrodeponering av platinum sort-elektroder og under målinger av nevral nettverksaktivitet. Et avgjørende funn var at nanotopografier kan fremme klynging av nevroner og aksonfascikulasjon, samt lavere grad av global synkronisering i nettverksaktivitet - karakteristiske strukturelle og funksjonelle trekk for småverdensnettverk. Samtidig som det er behov for ytterligere optimalisering og eksperimenter med større utvalgstørrelser før endelige konklusjoner kan trekkes, viste den utviklede nanotopografiske plattformen således potensiale for å forbedre kliniske relevans av *in vitro* nevrale sykdomsmodellsystem.

Preface

This project thesis is submitted in partial fulfilment of the requirements for the degree Master of Science in Nanotechnology at the Norwegian University of Science and Technology (NTNU). The work presented has been performed during the spring of 2021 at the department of physics, as part of the course TFY4905 - Master's Thesis in Nanotechnology. Experimental work has been carried out in the cleanroom of NTNU NanoLab.

It should be mentioned that the project was originally envisioned to be somewhat different than how it turned out. The original project was centered around patterning SU-8 with micropillars using electron beam lithography and testing resulting neuronal response. However, two months in to the project, the electron beam lithography machine broke down without prospects of recovery. Thus, the project had to pivot to its final format based on plasma etch roughening of SU-8. With two months less time to complete the project, the amount of experiments conducted had to be reduced.

It should also be mentioned that some parts of the theory, primarily in the fabrication section, were adapted from the work of the author in his specialization project revolving around optimization of platinum black deposition.

Acknowledgements

First and foremost, my warmest gratitude has to be extended to my supervisor, professor Pawel Sikorski, for arranging the project, serving as an incredible sparring partner in discussing experimental results and for general guidance throughout the project. Throughout the project I have come to realize that the intuition and gut-hunches of seasoned academics are spookishly correct more often than not.

For great co-supervision of the project, I have to thank Nicolai Winter-Hjelm. Particularly, he has shown incredible patience in meticulously going over newly written and poorly polished parts of the thesis with a fine comb, providing thoughtful input.

I also have to express my gratitude to the process engineers working at NanoLab for working tirelessly to fix machines that seemed increasingly eager to break down. Without their swift help, several of the experiments conducted would not have been possible. Especially, I would like to thank Jens Høvik for also providing invaluable insight into both photolithography and plasma etching.

Last, but not least, I want to thank my incredible classmates for making lunch breaks THE daily event to look forward to, and for offering shoulders to cry on when project work was delayed by lab equipment breaking for the hundredth time.

Contents

Figures

Acronyms

AFM atomic force microscopy. 25–27, 38, 39, 44, 46, 47, 50–52, 54, 67, 68, 70

AIS axon initial segment. 9

AP action potential. 7–10

BSE back-scattered electron. 27

CNS central nervous system. 10–13

DIV days *in vitro*. 45, 52, 59, 60, 65

ECM extracellular matrix. 13, 14, 63, 64, 73

HMDS hexamethyldisilazane. 31, 35, 42

ICP inductively coupled plasma. 18, 51

IPA isopropanol. 31–33, 35

MEA micro-electrode array. ix, 20, 33, 34, 41, 54–58, 64

PAG photoacid generator. 22–24, 68

PDMS polydimethylsiloxane. 19, 38, 39, 54, 55, 58, 59, 62–66, 70, 71, 73

PEB post-exposure bake. 22, 42

PVD physical vapor deposition. 18

RIE reactive ion etching. 18, 23–25, 51, 53, 62, 65, 68

RPM rotations per minute. 32, 35, 37

SE secondary electron. 27, 28

SEM scanning-electron microscope. 19, 27, 39, 40, 44, 46–52, 54–57, 65, 67, 68

Chapter 1

Introduction

Comprised of approximately 86 billion neurons, each forming thousands of connections with others, the human nervous system is an incredibly complex machine [1]. Despite its breathtaking complexity, however, the nervous system is also a part of our anatomy that is particularly vulnerable to chronic damage. With the exception of certain regions in the hippocampus, the neurons that make up the human nervous system lack the ability to proliferate after maturation [2]. In other words, the death of neurons constitutes a permanent loss, without the potential for regeneration. Neurodegenerative diseases that spread throughout the nervous system, such as Alzheimer's disease, cause irreversible damage as they progress, and wreak havoc on the vulnerable nervous system. With an aging global population, the prevalence of neurodegenerative diseases increases, along with the weight of their extensive societal and economic burdens. Evidently, understanding how to detect and treat these diseases in early onset is of vital importance, and the subject of numerous recent research efforts [3, 4].

Across various fields of biomedical research, including neuroscience, animal models have historically been considered the golden standard in studies of both disease conditions and potential treatment. Apart from the ethical concerns associated with using animal models in neuroscience research, cross-species genetic and systemic differences of the nervous system raises questions about the validity of animal models in reflecting neurodegenerative diseases in humans. Illustrating the limitations of animal models, no non-human species, including other primates, have thus far been found to develop Alzheimer's disease [5]. With the advents of microfabrication and stem cell technologies, increasingly sophisticated reductionist *in vitro* model systems have emerged as a promising alternative. Forming the fundament of such *in vitro* neural network model systems is the culturing of human neural cells, derived from *induced pluripotent stem cells*, on microfluidic chips [6]. Microfluidics represent a controlled and confined environment – a venue on which to study neurons, networks and disease in isolation from the myriad of unrelated biological processes in a living organism. Expanding on this blank canvas, relevant mechanical, biological and chemical cues can be incorporated to mimic conditions of the *in vivo* brain [7, 8]. Importantly, these platforms can further be fitted with arrays of microelectrodes for recording of the all-important electrical activity in neural networks, a key indicator of the state of function and dysfunction [9].

1.1 Project Background

In recent years, several *in vitro* neural network model systems have surfaced with demonstrated ability to recapitulate several aspects of the human nervous system [10, 11]. Nonetheless, important discrepancies between neural networks grown on these platforms and those growing naturally *in vivo* have also been uncovered, compromising the reliability of these platforms as models of both brain function and degeneration. Electrical recording of *in vitro* neural networks have exposed activity patterns largely incompatible with the complex so-called *small-world* architecture of the *in vivo* nervous system. Crucially, small-world architecture has been shown to facilitate the spread of disease to a greater extent than other network architectures, raising questions about the validity of neural network disease models that diverge from these architectural principles. So how can we better capture the network architecture of the *in vivo* brain in *in vitro* neural network models? Evidence suggest that the answer to recapitulating the network architecture of the nervous system lies in the architecture of the physical scaffolding surrounding it [12].

To understand the importance of the physical scaffolding of the brain in shaping its network architecture, we need to look at its process of construction. Leaving little to chance, the incredible process of human nervous system development is a tightly orchestrated one. Individual building blocks – neurons – and circuitry between them demonstrate an extraordinary ability to organize in to the complex, but purposeful, architecture that drives sensing, motion and consciousness. In the developing brain, newly born neurons trek across the brain, relying on guidance cues from their environment to arrive at the right place, at the right time [13]. Once there, similar cues direct the neurons to form circuitry with the right partners.

Traditional *in vitro* neural network model systems have been based on planar two-dimensional substrates, neglecting and missing out on the guiding effects of physical environments in formation of small-world neural networks [14, 15]. In recent years, however, researchers have sought to replicate these guiding effects by engineering environments on *in vitro* neural network platforms that mimic the physical environment of the brain [16]. The sensing apparatus of the neuron, the environmental features by which it is guided and the components through which they interact are all on the low micro-/nanoscale [17]. Hence, it is clear that nano- and microfabrication tools must be applied in the pursuit to mimic the physical environment of the brain.

1.2 Aim and Structure of Project

In this project, the goal was to develop a nanotopographically surface structured neural network recording platform. With introduction of nanotopographies on the platform, the aim was to induce neuronal organization into network architecture with a higher degree of the small-world characteristics found in the nervous system. Specifically, a plasma etch-based roughening effect on the photoresist SU-8 would be utilized and tuned to develop surfaces with nanotopographies promoting small-world topology in networks of neurons grown on the surface. Processes would then be established for incorporating these surfaces on an advanced neural network recording platform.

The progression of the project was structured into three phases, each with their own primary **aims** and objectives.

1. **Establishing photolithography protocols and small-scale platform for testing of surfaces with neurons.** Photolithography protocols for would be established for SU-8 photoresist films adhering to a 24x24 mm glass cover slip substrate interfaced with a petridish, forming a neural culturing platform. The photolithography and culturing platform would be evaluated on two criteria – ability of the SU-8 film to maintain adhesion to the glass throughout culturing and absence of adverse effects on neurons not related to the topography of the SU-8 surface. Progressing further in the project, the platform would be used for testing of neuronal culturing on SU-8 surfaces with different nanotopographies.
2. **Optimizing nanotopographies for small-world neural networks.** Utilizing the photolithography protocol and testing platform established in phase one, phase two would focus on optimizing the SU-8 plasma etch-based roughening process for topographies ranging across the nanoscale. Optimization of plasma etch process would be carried out by tuning of five parameters, which would be gas composition, gas release rate, chamber pressure, etch time and bias power, while keeping all other parameters constant. Achieved surface nanotopographies would be characterised qualitatively with microscopic imaging and quantitively by measurements of surface roughness metrics. Surfaces would subsequently be cultured with neurons and evaluated on two criteria – biocompatibility and ability to induce in grown neural networks structural characteristics adhering to small-world network principles.
3. **Incorporation on complete neural network recording platform.** From phase two, the etch condition and resulting nanotopographies found to induce the most promising effects on cultured neural networks would be selected. Using the selected etch condition, nanotopographical roughened SU-8 surfaces would be incorporated on a complete neural network recording platform, replacing the planar Si_3N_4 previously used as the base of the platform. In replacing Si_3N_4, nanotopographical SU-8 would have to be proved compatible with fabrication processes necessary for the complete neural network recording platform that had previously relied on Si_3N_4. Herein, bonding of a microfluidic structure to the SU-8 and use of SU-8 as an insulating layer during electrodeposition of platinum black microelectrodes would have to be proved viable. Finally, the complete platform would be cultured with neurons and used for electrophysiological recording to determine whether activity patterns could be observed that would imply improved small-world architecture.

While this particular project focused on the aspect of development, fabrication and characterisation of SU-8, nanotopographies and neural network recording and culturing platforms, a complimentary project focused on the neuronal cell work. All neuronal cell culturing as well as imaging and electrophysiological recording of neurons on the developed and fabricated platforms was performed in a simultaneous project conducted by Edevard Hvide. Therefore, the reader is encouraged also to read the thesis written by Hvide for more extensive descriptions and analysis related to that aspect of this double-faceted project [18].

Chapter 2

Theory

2.1 Neurobiology and *in vitro* Neural Networks

Neurons (nerve cells) are the fundamental functional units of the nervous system, exhibiting a wide variety of morphological, molecular, functional and connectional properties [19]. No two neurons are exactly the same, and classifying neurons into distinct categories has challenged neuroscientists since their discovery by Purkinje in 1837 [20, 21]. Critically, however, they all share the ability to interconnect and form functional networks capable of transmitting and processing information, forming the basis of the incredible and vastly complex machinery called the brain.

The following section will give a brief overview on select neurobiology topics. Sections on the anatomy, electrophysiology and signaling of a neuron should provide a basic understanding of how the fundamental building blocks of the brain function and how they can be monitored using extracellular recording techniques. Expanding beyond individual and connected pairs of neuron, an introduction to the establishment of neural networks and characteristics of the *in vivo* networks of the brain will be given, followed by a description of how neurons sense and utilize the physical environment in the formation of networks. More thorough coverage of these topics can be found in a number of excellent pieces of literature [22–24].

2.1.1 Anatomy of the Neuron

Although morphology varies between individual neurons, certain key features are found in all. Like any eukaryotic cell, neurons have a cell body (called a *soma*), containing its nucleus. Distinguishing the neuron from other cells, projections called *neurites* extend from the soma into the extracellular matrix. These projections allow neurons to form complex networks, branching out and establishing connections with up to thousands of other neurons whose soma are not in the immediate vicinity of the neuron from which the neurites originate [25]. Neurites are subdivided into *axons* and *dendrites*, which in broad strokes act as transmitter and receiver ends, respectively, of communication between neurons. While most neurons have several thousand dendrites, they commonly only have one axon, with the ability to branch out and form connections with numerous other neurons. During signaling events, electrical

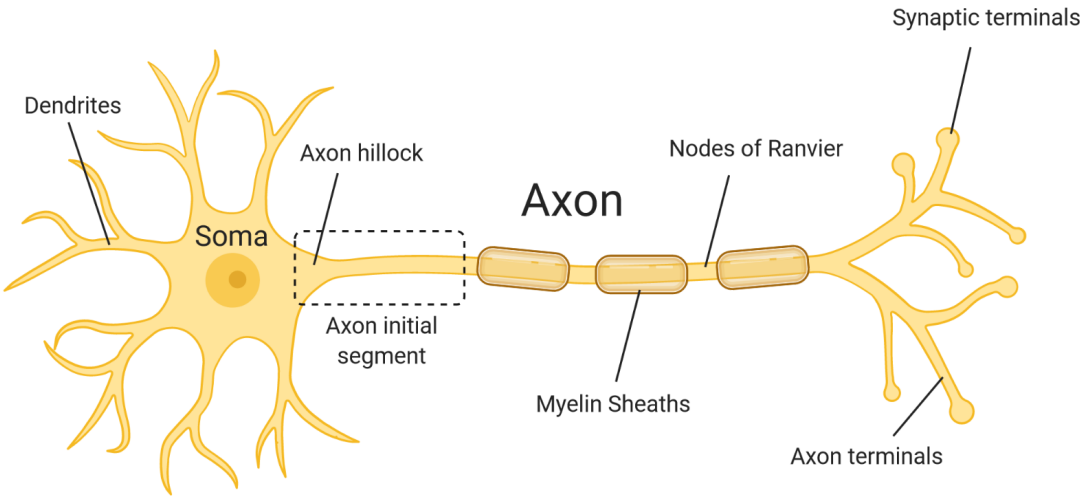

Figure 2.1: Illustration of a neuron, showing the protruding neurites. Dendrites branch off from the soma, along with a single axon. Starting at the axon hillock, the axon initial segment is a protein dense uninsulated segment of the axon. Beyond the axon initial segment, insulating sheaths of myelin wrap around the axon, interrupted by exposed patches of membrane called Nodes of Ranvier. The axon terminates at the axon terminals, with synaptic terminals situated at the very tip of axon terminals to form synaptic connections with other neurons.

signals flow along the axon of one neuron and are transmitted through connecting junctions (termed *synapses*) between the axon terminals of the transmitting neuron and the dendrites, soma or axon of receiving neurons. In recent years, several non-synaptic signaling mechanisms between certain neurons have been uncovered [26, 27], but synaptically transmitted signals remain the primary means of communication in the nervous system, and the primary signaling mechanism studied with the neural network recording platform this work aims to advance.

Providing a semi-permeable barrier to the extracellular environment, a plasma membrane consisting of a lipid bilayer and integrated proteins encloses the cytoplasm of the soma and protruding neurites. The plasma membrane barrier enables the neuron to maintain an intracellular environment that is chemically and electrically distinct from the extracellular environment. As will be discussed further in the sections below, this chemical and electrical distinction from the surrounding environment is of vital importance to the function of the neuron.

2.1.2 The Membrane Potential

By now it has been established that neurons are adept at forming networks of complex circuitry, and somehow rely on the ability to distinguish themselves electrically and chemically from their environment to perform their role in these networks. In order to understand the way in which neurons communicates with its connected partners, and how this communication can be recorded extracellularly on a neural network recording platform, a description neuron membrane polarization is warranted. Herein, two concepts are of particular importance and will be presented throughout, namely *resting membrane potential* and *action potential*.

In order to store energy (and thus information), the neuron utilizes separation of charges, analogous to a battery. Charges, in the context of neurons, refers to ions present in the intra- and extracellular fluid. Specifically, sodium, potassium, chloride and calcium ions make up the bulk of the charge separation efforts of the neuron [28]. Although the bulk solutions of both cytoplasm and extracellular fluid are net neutral in charge, large concentration differences of individual ion species between the intra- and extracellular solutions gives rise to a polarizing effect locally at the semi-permeable membrane separating the two. The establishment of local charge imbalances, and thus a potential difference, over the membrane is driven and controlled by two opposing forces. Entropic forces drive ions down their concentration gradient, while electrostatic forces drive ions down their electrostatic potential gradient. Movement of ions down their concentration gradient, driven by entropic force, leads to an increasing charge imbalance across the membrane resulting in a stronger electrostatic force counteracting the movement, and a steady state potential is reached where there is no net movement of ions in either direction. The movement is however limited to membrane bound *ion channels*, which are specific to certain ion species and by their opening and closing – in response to electrical, chemical or mechanical cues – determine the rate of movement of specific ions, and thus the degree by which they contribute to the polarization of a patch of membrane.

When uninterrupted by internal or external stimuli, a steady state potential is maintained, called the *resting membrane potential*. At the resting membrane potential, a large amount of potassium channels called "leak" ion channels are open, providing a high basal permeability of potassium. While other basal ion conductances occur, they are far lower than that that of potassium, and hence the resting membrane potential of approximately $-70\,\text{mV}$ is chiefly determined by the concentration gradient of potassium [29, 30]. Voltage-gated ion channels, on the other hand open upon depolarization of the membrane from internal or external depolarizing stimulus, and are responsible for the sudden spikes in potential we call *action potentials (APs)*. Voltage-gated Na^+ channels open in large numbers once a threshold depolarized potential of approximately $-55\,\text{mV}$ is reached, suddenly drastically increasing the permeability to Na^+, causing a vast influx. The membrane potential shoots up, switching polarization and approaching a positive value of around 40 mV, determined primarily by the concentration gradient of Na^+. As the potential approaches the peak value, the voltage-gated sodium channels become inactivated, while voltage-gated potassium channels open. Potassium permeability once again dominates, and the membrane quickly repolarizes to a negative potential, even dipping below the resting membrane potential and

becoming *hyperpolarized* before the voltage-gated potassium channels become inactivated and the membrane settles back to the resting membrane potential determined by basal conductances.

Although fluxes of ions take place both during resting membrane potential and an AP, concentration gradients of ions over the membrane are kept virtually constant, thus maintaining a constant level of resting membrane potential. Making up one of the pieces of the membrane machinery, a family of proteins called *ion pumps* consume chemical energy in the form of ATP to pump ions against their concentration gradients. As the largest contributor, the Na^+/K^+-pump exports 3 sodium ions and imports 2 potassium ions in a cycle, using a single molecule of ATP.

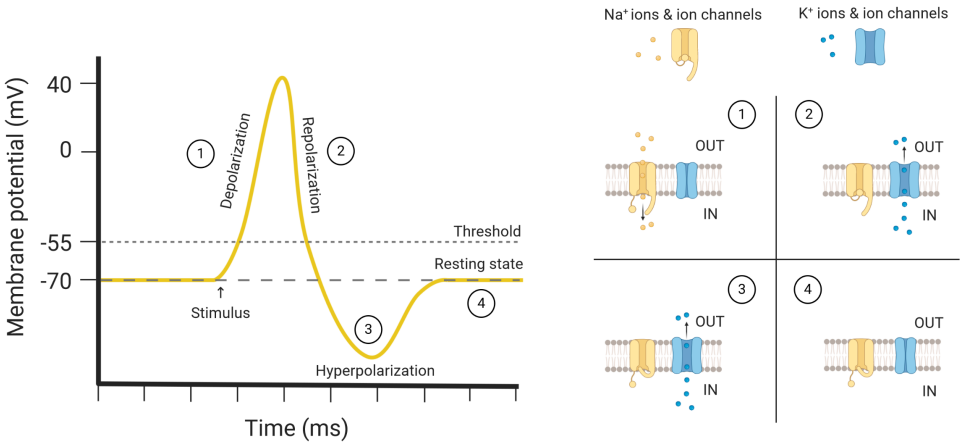

Figure 2.2: Schematic of the cycle of events occurring throughout an AP. Initial depolarization stimulus above the threshold potential results in opening of Na^+-channels, and subsequent depolarization up-shoot of the membrane potential. Approaching the Nernst potential for Na^+, the Na^+-channels close and K^+-channels open. Thus the membrane repolarizes, and reaches a hyperpolarized state before settling back to the resting potential.

Forming the basis of extracellular neuron recordings, the sudden explosive fluxes of ions that make up the AP cause detectable charge disruptions and current flows in the extracellular solution. While these extracellular charge disruptions dissipate quickly with distance from the neuron, electrodes situated within approximately $<100\,\mu m$ from the neuron source can pick up the signals [31]. A single electrode picks up signals from multiple neurons in its proximity simultaneously, but the activity can be discerned and traced back individual neurons by spike sorting algorithms [32]. In this way, neural network recording platforms – such as the one this work aims to improve – monitor the all-important electrical signalling activity of neural networks.

2.1.3 Signal Transmission

Crucial to the function of neurons, the event referred to as an AP does not occur in isolation at one patch of membrane, but rather initiates or partakes in a chain reaction traversing the axon of the neuron. APs propagate down the axon to the synapses at the axon terminals, constituting a traveling neural signal. An AP is initiated at the axon initial segment (AIS), an event referred to as *firing*, and propagates towards the terminal ends of the axon by means of a domino effect. An AP at one patch of membrane causes a large local influx of sodium. The surplus of sodium ions diffuses in all directions, depolarizing adjacent patches of membrane sufficiently to open voltage-gated sodium channels there. Temporary inactivation of voltage-gated ion channels following a depolarization-repolarization cycle, disabling the channels from opening immediately after regardless of membrane potential, ensures that the AP travels unidirectionally.

Propagation of an AP strictly by means of continuous depolarization of adjacent ion channels is comparatively slow, propagating at a speed of 0.5-10 $\mathrm{m\,s^{-1}}$. In order to transmit signals over large distances more rapidly, neurons with long axon projections overcome this limitation by insulating large parts of the axon. Rather than having the entire length of the axon membrane covered by ion channels, ion channels are located densely in non-insulated nodes, termed *nodes of Ranvier*, separated by long sections of insulated membrane. Patches of membrane from supporting non-neuronal cells in the nervous system wrap around the axon forming insulating sheaths called *myelin*. Signals propagate along the insulated axon sections at a speed of up to 150 $\mathrm{m\,s^{-1}}$ and are re-innervated at the nodes of Ranvier to ensure that the signal does not dissipate as it is traveling down the length of the axon.

Upon reaching the axon terminals where the neuron synapses on to another, the AP is translated to a stimulus of the postsynaptic neuron. Two categories of synapses facilitate the translation of a presynaptic AP to a postsynaptic stimulus, namely electrical and chemical synapses. In the case of electrical synapses, the AP is conducted directly from one neuron to another via conducting channels coupling the neurons. In the far more numerous chemical synapses, the presynaptic AP triggers release of chemicals dubbed *neurotransmitters* into the extracellular gap, the *synaptic cleft*, separating the pre- and postsynaptic structure. Neurotransmitters bind to ligand-gated ion channels on the post-synaptic structure of the receiving neuron, triggering the opening of the channel and subsequent fluxes of ions in to or out of the postsynaptic neuron. Depending on the type of neurotransmitter and the channel it binds to, this stimulus can either be excitatory or inhibitory, ie. causing ion fluxes that depolarize or inhibit depolarization of the neuron. Furthermore, the amount of neurotransmitters released modulates the strength of the stimulus on the postsynaptic neuron. Thus, the chemical synapse, in contrast to the electrical, contributes a modulated and flexible mode of signal transmission that is crucial for the complex computations of the brain [33]. While depolarization from a single synaptic transmission is generally not enough to single-handedly cause firing of the postsynaptic neuron, the combined depolarization from thousands of synapses or rapid successive transmission from a single neuron integrating at the soma can be.

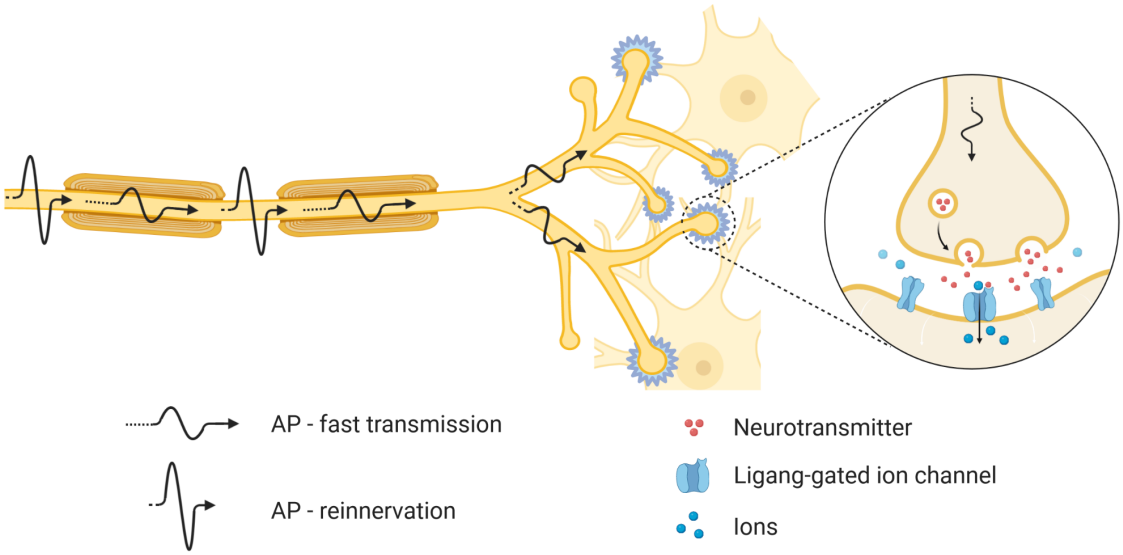

Figure 2.3: Illustration of AP propagation through a neuron and subsequent signal transmission via a chemical synapse to a postsynaptic neuron. The AP propagates quickly through myelinated patches of the axon, and is reinnervated at regular intervals at the nodes of Ranvier. Reaching the synaptic terminal, the AP induces release of neurotransmitters binding to ligand-gated ion channels on the postsynaptic neuron, resulting in fluxes of ions in to the postsynaptic neuron.

2.1.4 From Neuron to Network

By now it should be clear what makes up the base components of a neuron, how its electrical state is established and tuned, and how communication between pairs of neurons occurs. However, as mentioned in the introduction (Ch. 1), the extraordinary complexity and vulnerability of the brain arises not primarily from single neurons or neurons connected in pairs, but from the formation of intricate networks composed of billions of neurons each connected to thousands of others [34]. It is at the scale of networks we find the characteristic differences of *in vivo* and *in vitro* neural networks this project aims to help bridge the gap between.

During the development of the central nervous system (CNS), three major processes occur in sequence and are neatly orchestrated to form intricate networks of high computational efficiency – neurogenesis, neuronal migration and circuit formation. Progenitor cells in epithelium around the neural tube proliferate and differentiate to neurons and glia – an umbrella term for supporting non-neuronal cells of the brain. Newly differentiated neurons, in turn, migrate and disperse throughout the CNS under tight guidance by mechanical and chemical cues to arrive at their designated location in the network [35]. Arriving at their destination, neurites begin to protrude from the neuron to form signalling circuitry, integrating the neuron into the wider neural network.

Axon outgrowth and expansion in to the surrounding environment is preceded by a fan-shaped structure at the tip of the axon called the *growth cone*. Responding to attractive and repulsive stimuli the growth cone senses environmental cues and steer

the growth and branching of the axon towards its target. Among possible guiding environmental cues is other axons; in a process called *fasciculation* an axon zips together with one or a bundle of axons to grow towards a common target region [36]. Once the axon reaches its targets, it finalizes the connection between the originating and target neurons by forming synapses.

Adhering to this sequence of events, the connected network in the CNS is formed. During development, neurons extend axons to more targets than required in the mature network, and undergo *axon pruning* to reduce the amount of connections. Additionally, the mature CNS undergoes continual restructuring in various processes collectively referred to as *plasticity*. However, in the interest of brevity, the curious reader is referred to other elaborate works on these topics [37, 38].

Matured, connected neural network can be examined in terms of structural and functional connectivity. Structural connectivity refers to the anatomical connectivity – synaptic and physical connections between neurons on a small scale or brain regions on a larger scale. Functional connectivity captures the temporal correlation in firing activity – i.e. close and distal neurons or regions often firing together. The two aspects of network connectivity are however closely interrelated [39]. Directness and strength of structural interconnections between neuron ensembles have been shown to determine and constrain the funtional interactions they can form [40]. Conversely, functional connectivity patterns can induce plasticity, reshaping the structural connectivity of a network – hence the old saying "neurons that fire together wire together" [41]. In the field of network neuroscience, both structural and functional connectivity on different scales are commonly analysed using the framework of *graph theory* [42]. In accordance with graph theory, neural networks are topologically represented by nodes – individual neurons, groups of neurons or brain regions – connected by edges – structural or functional connections.

Two major principles govern the organization of the *in vivo* brain – functional segregation and integration. As an example of functional segregation, in the visual cortex, separate brain areas are functionally specialized for perception of different visual aspects, such as color, shape and motion [43]. Building on the visual example, functionally segregated areas responsible for color, shape and motion must be integrated to make out a pedestrian crossing the road and appropriately respond by stepping on the brakes while driving. Advances in network neuroscience have in recent years identified important topological network characteristics that promote segregation and integration in the brain [12]. Exhibiting *small-world* attributes, *in vivo* neural networks are characterised by prominent local clustering and short average path length, with highly interconnected nodes within clusters and sparse long-range connections linking the clusters globally [44]. Here, path length between two arbitrary nodes in the network is defined as the minimum number of edges that must be crossed to get from one node to the other. Emergence of richly connected hub nodes, which integrate signals from clusters and are strongly interconnected to each other to further integrate signals from separate specialized regions, is another characteristic accompanying small-world networks [42]. By theoretical modeling, these attributes have been demonstrated to be strongly associated with functional segregation and integration [45]. An illustration of the small-world characteristic of the brain is displayed in fig. 2.4.

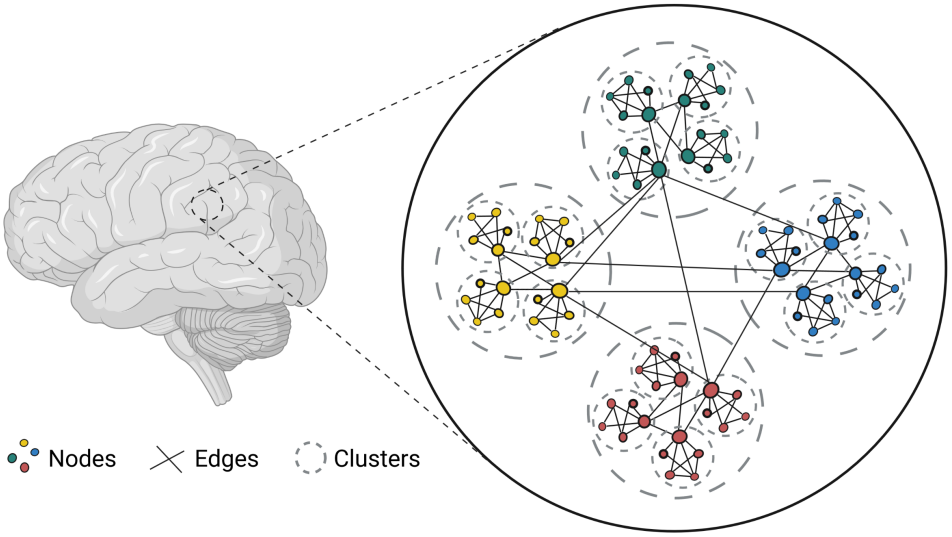

Figure 2.4: Illustration of the small world network topology found in the brain, represented with nodes and edges in accordance with graph theory. Outlined with gray dashes, clusters of highly interconnected nodes are found on multiple scales – smaller and larger dashed circles. Connections between clusters are few and largely concentrated to richly connected hub nodes.

Hallmarks of small-world network topology manifest on both a structural and functional level, and on the scale of neurons and groups of neurons as well as larger brain regions. On the structural level at the scale of neurons, extensive clustering of neurons is an intuitive indication of small-world networks. Fasciculation forming stable and strong connections – axon bundles – between local clusters can indicate the emergence of hubs [46]. Functionally, small world networks are characterised by local and within-cluster activity, with low to intermediate synchrony in activity on a larger network scale [47].

Conversely, electrophysiological recording of many neural networks cultured *in vitro* have pointed towards emergent behaviour that is largely incompatible with the small world topology of the brain. *in vitro* neural networks have shown a propensity for highly synchronous burst activity across the entire network, indicating a topology that deviates from the small world principles [48, 49]. This discrepancy in network characteristics from the *in vivo* neural networks limits the accuracy of *in vitro* networks as models for conditions of the human brain. Particularly, small world networks have been demonstrated to facilitate spread of neurodegenerative diseases, such as Alzheimer's and ALS, emphasizing the importance of network topology in *in vitro* brain disease models [50, 51].

Clearly there is a need to improve the topological similarity of *in vitro* networks to those of the *in vivo* brain. One key ingredient missing from the culturing platforms for *in vitro* could be surface topography – a physical landscape mimicking the extracellular environment the neurons experience in the brain [16]. As mentioned in the start of this section, several developmental processes of the CNS rely in part on physical and mechanical cues for guidance. Inspiring this project, mimicking these physical and

mechanical cues in neural network culturing platforms might induce topology more similar to the brain, and thus improve relevance as function and disease models. So how does the neuron sense the physical environment, and at what size scales?

2.1.5 Sensing the Physical Environment

In the CNS, developmental processes such as neuronal migration and neurite growth rely on a symphony of chemical and physical guidance cues. Guidance dependency for development of the neural networks in *in vitro* recording platforms is however likely skewed towards physical cues, as neurons are placed in a relatively homogeneous chemical environment. Neurons have been shown to utilize axons of other neurons, blood vessels and glial fibers for guidance [52, 53]. However, this introduction will be limited to interaction with the environmental landscape topographic network culturing platforms seek to mimic, namely the extracellular matrix (ECM). The ECM is the extracellular structural scaffold, composed primarily of a matrix of collagen fibers lined with interspersed proteins, as well as polysaccharides and water. Collagen forms the structure and the proteins the specific interaction sites making up the physical guidance cues.

Although the specific response to the physical cues of the ECM differ between different developmental processes and between different neuronal cell types, the sensing apparatus is largely the same [54]. As the primary mechanism of physical sensing, neurons interact with the ECM through adhesion complexes formed between transmembrane receptor proteins of the neuronal membrane and ligand molecules of the ECM. Specifically, the transmembrane protein integrin binds to ECM proteins such as fibronectin, vitronectin and laminin – the protein used to coat surfaces in the neural network cultures of this project [55].

On the side of the neuron, slender membrane protrusions called filopodia act as environment sensing probes. They are supported by dynamic actin fibre bundles oriented towards the tip of the filopodia, and extend rapidly outwards until they reach a threshold extension and collapse [56]. In growing axons they are situated at and protrude from the growth cone, as mentioned in section 2.1.4. Along with a thin actin fibre supported membrane sheat called lamellipodia, they form the characteristic "fan-shape". On migrating neurons they protrude densely from the tip of a larger membrane protrusion leading the migration called the leading edge, but also protrude less densely along the entire edge of the migrating neuron [57]. Actin bundles in the extended filopodia adhere to surfaces mediated by integrin, bound to the actin via adaptor proteins, binding to ligand proteins on the surface [58]. Depending on a complex set of mechanisms, involving molecular pathways and the neuron applying force, these adhesion complexes either dissolve or mature into larger *focal adhesions*. Focal adhesions, in turn, act as anchorage points and relay information about the environment to the neuron – inducing branching in or directing growing axons or guiding the locomotive migration of the neuron [59, 60]. Contact angle of the filopodia with the surface, the mechanical stiffness and rigidity of the surface and other surface properties induce different levels of force and stress exerted on the adhered filopodia [61]. Thus, filopodia are able to sense and relay a breadth of information about a surface,

such as its topographical features, to the neuron.

When considering the scale of the components involved – both intracellular and extracellular – in neurons sensing their physical environment *in vivo*, it becomes clear that micro- and nanofabrication are indispensable tools to replicate the effect *in vitro*. Probing filopodia are typically around 100-200 nm in width, while the collagen fibrils shaping the ECM they probe are tens to hundreds of nanometers [62, 63]. Adhesion complexes are on the scale of 5-200 nm, while focal adhesions are between 200 nm and 10 µm [64, 65]. The sensing apparatus of the neuron is finely tuned, and capable of detecting features with nanometer sensitivity.

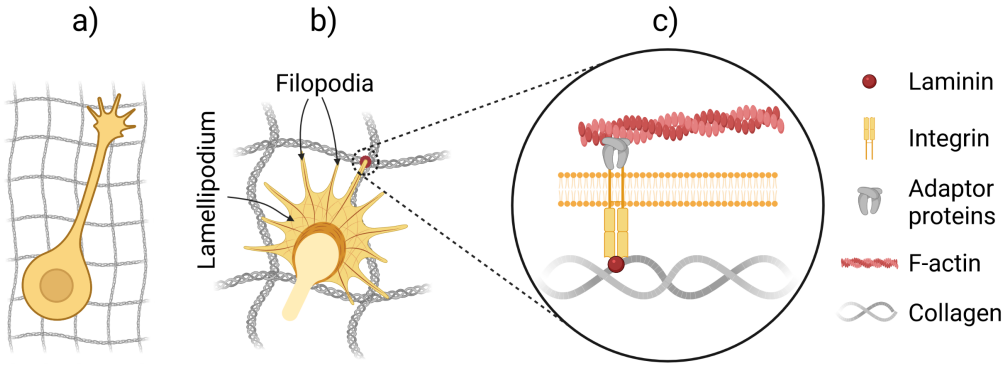

Figure 2.5: Illustration of a neuron growing an axon and sensing the ECM via probing filopodia. a) displays the neuron perched on the ECM collagen fibrous matrix. b) is a zoomed in view of the growth cone at the tip of the growing axon, composed of a lamellopodium and protruding filopodia, interacting with the ECM. c) overview of the main components in the interaction of the filopodia with ECM. Integrin is bound to the actin filaments (F-actin) of filopodia via adaptor proteins. Integrin also binds to an ECM protein – in this case laminin – on the ECM collagen matrix to form an adhesion complex which can mature into a focal adhesion and direct the growth of the axon.

Efforts to induce different behaviour in neurons by culturing on structured surfaces with features on the micro- and nanoscale have been numerous, and have employed a multitude of structuring strategies. For an extensive review of structuring experiments and induced effect, the interested reader is referred to the work of Marcus et al. in 2017 [16]. Anisotropic features, such as directed ridges, groves and parallel fibers have been demonstrated to enforce directionality on developmental processes. On the scale of a few micrometers down to tens of nanometers, anisotropic features on different substrates have directed both neuron migration and neurite growth, either parallel or perpendicular to the feature direction [66–68]. Isotropic features, such as roughened surfaces, fibers of random orientation and random or regular matricies of beads and pillars, have shown effects on degree of migration, neurite outgrowth and surface adhesion. Demonstrating the sensitivity of the sensing apparatus, isotropic features have switched form increasing to decreasing, and vice versa, all of the aforementioned effects by nanometer-scale changes in dimensions [64, 69, 70]. Important to this project, in their work in 2017, Onesto et al. found evidence of nanoscale surface roughness inducing small world topology in *in vitro* neural networks. In the low nanometer range, for surface roughness values of 0 to 30 nm, they found the small-worldedness of neural

networks to increase with increasing roughness of a silicon substrate. Based on these findings, this project set out to incorporate surface roughened nanotopography on a neural network recording platform by means of microfabrication.

2.2 Fabrication and Characterization Techniques

In the pursuit of establishing a novel *in vitro* neural network recording platform, a wide range of fabrication and characterisation techniques were applied. As they are presented in this section, a general description of each technique will be preceded by a short note of which part of the project they apply to.

2.2.1 Microfabrication

Microfabrication encompasses a variety of fabrication techniques aimed at producing features on the micrometer scale by means of patterning, deposition and etching techniques. Particularly defining of microfabrication, processes are often based on an initial patterning of a film on a substrate, which in turn acts as a mask in subsequent deposition or etching (removal) of material.

This sub-section will outline the theory behind the microfabrication techniques chosen for the project. A more thorough theoretical description of the techniques applied can be found in a variety of microfabrication literature [71–73].

Photolithography

At the heart of many microfabrication projects – including this work – is the patterning technique photolithography. In particular, photolithography was utilized to apply patterned SU-8 films on both the 24x24 mm glass cover slips of the reduced-scale neural culturing testing platform and the 4" glass wafers of the complete neural network recording platform. It was additionally used to create a mask for metal deposition of the wiring, electrode bases and contacts for recording of neurons on the complete platform.

Photolithography is a technique in which a photosensitive polymer solution called a *resist* is selectively exposed to light to imprint geometric patterns. Upon exposure to light of a wavelength within the sensitivity-regime of the resist, the polymer compounds in the resist are rendered either less or more soluble. These alterations in the solubility of the resist are owed to the forming or breaking of cross-linking chemical bonds between polymer strands, catalyzed by a sensitizer chemical in the resist activated by light. Depending on whether the solubility of the resist increases or decreases during exposure, the resist is classified as *positive* or *negative*, respectively. After exposure, the more soluble resist is removed with a solvent, while the less soluble resist remains, forming geometric patterns according to the design of the light exposure.

In practice, the photolithographic fabrication process is a multi-step one, in which several parameters and techniques can be tweaked at each step to modify the characteristics of the end-result. Although additional steps may be required when using

certain types of resist, or optionally added to further improve resist characteristics, the following steps make up the base of the process:

1. **Cleaning** – Prior to deposition of resist, the wafer is cleaned to minimize contaminants and improve the adhesion of resist to the wafer substrate. The initial cleaning of the wafer involves submerging the wafer in organic and/or inorganic solvents and cleaning it for a couple minutes to remove contaminants. Plasma cleaning is often used as an additional cleaning step, in which the substrate is exposed to high energy plasma (typically based on O_2 or Ar gas) capable of breaking most organic bonds, dissolving organic contaminants on the surface.
2. **Dehydration bake** – Following the cleaning procedure, a baking step is necessary to remove remaining humidity on the substrate. The presence of water on the wafer surface during deposition of resist could interfere with the adhesion of the resist to the substrate.
3. **Spin coating** — In order to obtain a layer of resist of uniform thickness across the entire substrate, centrifugal force is utilized to distribute the resist. After depositing drops of liquid resist in the middle of the substrate, the substrate is spun at high RPM, exerting centrifugal force on the resist that pulls it out towards the edges of the substrate. Eventually, a homogeneous layer forms across the entire substrate, the thickness of which is determined by the viscosity of the resist and the spinning RPM.
4. **Soft bake** — Typically carried out at 95 °C, the resist-covered substrate is baked to remove remaining solvent in the resist. Driving off solvent from the resist solidifies it and improves its stability [74].
5. **Exposure** — Inducing the solubility changing photo-activated chemical reactions of the resist, the resist is selectively exposed to light, typically in the UV-range (<400 nm). Traditionally, selective light exposure was performed by using a physical mask fabricated with the specific design to be imprinted on the wafers, through which light from a UV source shone onto the resist. In recent years, however, advances in photolithography have alleviated the need for a physical mask. Using either direct printing at the focal point of a laser and lens setup or a Spatial Light Modulator (SLM), which in essence acts as a dynamic and programmable mask, current maskless photolithography equipment is able to convert a computer generated design to an accurate photolithography exposure process on the substrate [75].

   An important parameter to consider for the exposure process is the exposure dose. Measured in energy per unit area (mJ/cm^2), the exposure dose determines the amount of light radiation the exposed parts of the resist will be subject to. Underexposure, a too low exposure dose, leads to insufficient solubility altering reaction towards the bottom of the resist, which will be exposed to light at a lesser extent than the surface. Severe overexposure, an excessive exposure dose, can cause solubility altering reactions beyond the edges of the designed exposure pattern, due to diffraction and reflection of light from the underlying substrate [76].
6. **Development** —- After exposure, the more soluble sections of the resist, i.e exposed or unexposed resist for positive or negative resist respectively, are removed

by means of dissolution. Specific to the resist, a solvent called a *developer* is used to dissolve the resist.
Of critical importance to the edge features of the final resist pattern, the development time is a parameter that must be optimized for any successful photolithographic process. Underdevelopment is characterised by incomplete dissolution of the more soluble resist, particularly at the edges of the resist pattern, creating an outward sloping edge profile. Overdevelopment, on the other hand, is characterized by partial dissolution of the less soluble resist at the edges of the resist pattern. Although unfavorable for most applications, overdevelopment is utilized to intentionally manipulate the edge profile of negative resist metallization masks. In negative resist, exposed resist is rendered less soluble, where the light exposure gradient from the surface of the resist to the bottom causes the bottom of the exposed resist to be slightly more soluble than towards the surface. Thus, limited overdevelopment preferentially causes dissolution of the bottom layers of the resist at the pattern edge, creating an overhanging structure called an *undercut*. Following metallization, the resist mask, along with the metal deposited on top of it, must be removed with a solvent. The process of mask and metal removal is called *lift-off*. As shown in figure 2.6, the undercut structure facilitates the removal of the resist mask in the solvent by leaving an open gap through which the solvent can reach the resist.

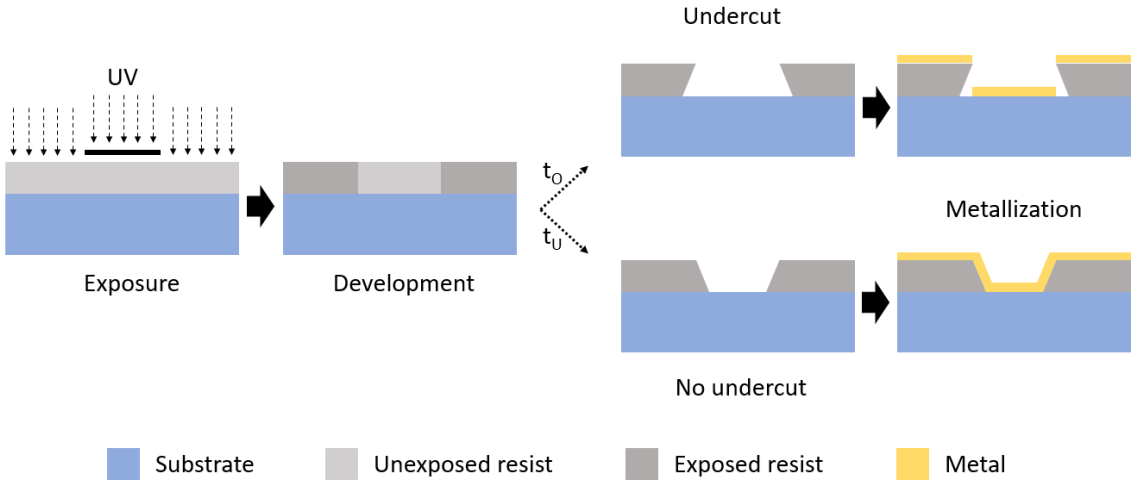

Figure 2.6: Illustration of photolithographic process for a negative photoresist metallization mask. When the resist is developed for time t_O (overdevelopment), the resulting metallization mask develops an undercut structure. When developed for time $t_U < t_O$ (underdevelopment), it does not. The undercut structure leaves a gap between deposited metal and resist, facilitating lift-off.

Metallization — Electron Beam Evaporation

Mentioned in the previous section, metallization was used, in conjunction with a photoresist mask, in this project to form the electrode bases, wiring and contacts of the *in vitro* neural network recording platform.

Characterized by atom-by-atom deposition of metals through condensation from vapor phase in an inert environment to solid phase on a substrate, physical vapor deposition (PVD) is a commonly used means of metal deposition in microfabrication [77]. Sputtering and electron beam evaporation make up the two primary PVD techniques, differing in their method of inducing a gaseous phase from a solid metal target. In electron beam evaporation, an intense electron beam originating from an electron gun is directed and accelerated towards a metal target by magnetic fields. Upon hitting the metal, a highly localized heating and subsequent evaporation of the metal occurs. Performed in a vacuum chamber, the mean free path of evaporated metal atoms is far larger than the distance between the metal target and the substrate [78]. Thus, the atoms are able to traverse the chamber without colliding and precipitate on all exposed surfaces without external guiding forces. Due to the evaporated atoms taking a direct path from the target to the deposition substrate, a line-of-sight effect makes it hard to achieve completely uniform growth over the entire substrate. One strategy to achieve more uniform growth is to continuously rotate the substrate during deposition.

Placing a substrate prepared with a photoresist mask in the chamber facing the metal target from which the evaporation occurs, a controlled metal deposition with growth rate typically ranging from $1\,\text{Å}\,\text{s}^{-1}$ to $10\,\text{Å}\,\text{s}^{-1}$ can be achieved [79]. After metal deposition, the photoresist mask and the excess metal deposited on top of the resist are removed by submersion and rinsing in an organic solvent dissolving the resist, a process referred to as *lift-off*. Metal deposited directly on the underlying substrate, through the openings in the photoresist mask, remains on the substrate.

Etching — ICP-RIE

Crucial to the formation of nanotopographical surfaces inductively coupled plasma (ICP)-reactive ion etching (RIE) was used in this project to etch and roughen SU-8 films. Here, a brief introduction to etching and ICP-RIE will be given, while a more elaborate description of the characteristic roughening etch of SU-8 is given in a later section.

Etching is a process of material removal from a substrate, and can be subdivided into wet etching and dry etching. While wet etching involves submersion of substrate in a chemical etch solution, dry etching utilizes ion bombardment to dislodge material from a substrate. One commonly used dry etching technique called RIE relies on chemically reactive plasma excited in a vacuum chamber to etch material. High-energy ions from the plasma are accelerated towards the substrate by an electric field applied between an electrode in the top of the chamber and the substrate holder. In ICP, one RF sources excites the plasma, while another RF source produces the electric field accelarating the ions towards the substrate.

In RIE, bombarding the surface with high-energy ions provides anisotropic etching normal to the substrate, while the chemical reactivity of the ions further selectively etch the materials they react with. Thus, a compromise is struck between an anisotropic physical etch, allowing smaller features to be etched, and a chemical etch providing material selectivity [80].

PDMS Soft Lithography

Forming the microfludic structures of the neural network recording platform, polydimethylsiloxane (PDMS) was used, shaped in to its final structure by a soft lithography technique.

Soft lithography refers to a range of fabrication techniques imprinting geometric patterns through molding, stamping or embossing of soft matter, specifically elastomers. Commonly used as a complement to photolithography, soft lithography offers the comparative advantage of experimental simplicity, high through-put and low cost [81]. Once a master – i.e. a mold with the geometric features to be replicated directly on a structure or indirectly via a stamp – has been fabricated using photolithography or other microfabrication techniques, it can be reused several times in soft lithography to fabricate the same features on several samples.

Having found extensive use in biomedical research, PDMS is one of the most common elastomers used for soft lithography [82]. Several characteristics contribute to the popularity of PDMS for biomecical applications. A non-exhaustive list includes biocompatibility, transparency facilitating optical imaging, gas permeability and ease of deforming [83]. Crucial to its most common application, in microfluidics, PDMS also has an excellent ability to form waterproof seals with surfaces of glass or other silicon compounds after simple surface modification. Conveniently, the same surface modification simultaneously transforms the surface of PDMS from a hydrophobic surface to a hydrophilic one. Thus, PDMS patterned with microchannels, chambers and other features can easily be bonded to glass and rendered hydrophilic to facilitate liquid flow, forming excellent microfluidic platforms. Treatment in oxygen plasma removes organic hydrocarbon compounds from the surface of the PDMS and leaves a surface covered by siloxide groups (SiO_x). These siloxide groups render the surface hydrophilic, but are highly reactive [84]. Immediately bonding the PDMS to glass also treated in oxygen plasma, SiO_x groups on the PDMS surface react with activated SiOH groups on the glass and form permanent siloxane (Si – O – Si) bonds with the glass, sealing the PDMS irreversibly to the glass. By wetting the resulting microfluidic structures following bonding, hydrophobic recovery of the PDMS surface is prevented and the hydrophilicity maintained.

While irreversible bonding and sealing of PDMS to glass or surfaces of other silicon compounds is readily achieved by a simple oxygen plasma treatment, irreversible bonding to surfaces of compounds lacking silicon – such as the SU-8 photoresist on which PDMS is bonded in this project – is not. Several alternative strategies have been developed for achieving irreversible bonding of PDMS to photoresist surfaces, including functionalization with adhesives, N_2 plasma treatment and heating to introduce amino-groups on the PDMS and silanization of the resist surface [85–87]. However, reversible bonding relying on weak van der Waals interactions between the PDMS and the substrate have also demonstrated the ability to form waterproof seals with various surfaces [88]. Although unable to withstand hydraulic pressure in continuous-flow microfluidics, reversible bond seals could be sufficient in quasi-static systems without extensive liquid flow, such as neuronal culturing platforms. Additionally, reversible bonds offer the comparative advantage of the option to remove the PDMS structure from the substrate after it has served its purpose, e.g. to enable scanning-electron

microscope (SEM) imaging of neurons after maturation in the microfluidic device.

Electrodeposition of Platinum Black

On the neural network recording platform, platinum black was deposited on top of planar platinum elecrodes to improve recording quality, as will be described below. Deposition of platinum black was achieved by electrodeposition.

Electrodeposition is a film growth process in which a metal coating is formed on a metal substrate by electrochemical reduction of corresponding metal ions in an electrolyte solution. An electrochemical cell is established where a cathode, on which reduction and growth of metal occurs, and an anode, where oxidation occurs, are placed in an electrolyte bath with metal ions and connected via an external circuit. By connecting the electrodes through an external circuit, current can be driven through the system, driving the electron exchanging reduction and oxidation reactions at the electrodes [89]. Fundamentally, an applied potential between the anode and the cathode acts as the driving force for metal ions in the solution to overcome various energy barriers associated with the reduction of the ion and incorporation in to the metal lattice at the cathode [90]. Increasing the potential difference between the cathode and anode equates to an increase in the driving force of the electrochemical reaction, and thus faster reaction kinetics.

Among common materials deposited by means of electrodeposition is platinum. Due to its high electrical conductivity, it is a well suited material for electrode fabrication. Furthermore, platinum has found extensive use in biological and medical application, due to its inherent inertness in organic environments and resistance to corrosion making it highly biocompatible [91]. A highly porous, and thus exhibiting vastly increased effective surface area compared to its non-porous counterpart, preparation of platinum dubbed *platinum black* has been used as an electrocatalyst for well over a century and has in recent years been adopted in neuroscience to produce highly efficient electrodes for neural recording [92–94]. Increasing electrode surface area has been proven to result in lower electrode impedance, which in turn increases signal strength and reduces noise during recording of neurons [95]. At the same time, the specificity of neural recordings – the ability to discern the signals of individual or small groups of neurons from one another during simultaneous recording of several neurons by a single electrode – has been shown to be affected negatively by increasing the lateral dimensions of the electrode [96]. Therefore, porous nanostructured electrodes with vastly increased surface area compared to planar electrodes of equal diameter, such as platinum black electrodes, have become popular for neural recording MEAs [97].

Electrodeposition of porous platinum black, rather than platinized platinum (planar platinum), is a process that is not fully understood, and is likely the result of a complex combination of interactions. However, based on previous research on the topic, reactant depletion kinetics is deemed a primary contributing factor [98]. Under high applied driving potentials, the reaction rate is sufficiently high to cause highly localized and eventually more global depletion of reactant – i.e. platinum ions in the solution around the electrode – leading to *mass transport limited* growth. Growth rate is lim-

ited by the transport of reactants from the bulk solution to the site of electrochemical reaction, rather than the rate of the reaction it self and the establishment of depletion zones causes preferential nucleation in certain sites and exclusion of nucleation in adjacent sites, as illustrated in figure 2.7. The result is ramified, non-homogeneous growth.

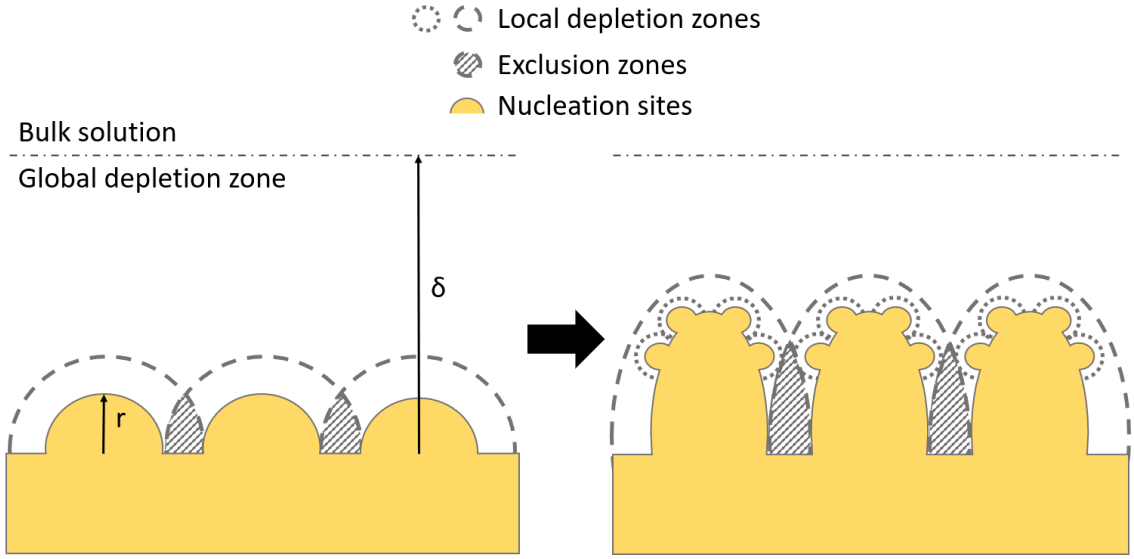

Figure 2.7: Illustration of mass transport limited growth and development of local and global depletion zones, resulting in exclusion of adjacent nucleation. r denotes radius of nuclei and δ extent of global depletion zone. Due to the fact that the distance from the nuclei to the bulk solution outside the global depletion zone is shortest at the top of the nuclei ($\delta - r$), growth normal to the surface is favored, where the diffusion length is shortest. As the initial nuclei grow, secondary nuclei (new nucleation on existing nuclei) form, along with their depletion zones, following the same principles of excluding growth of adjacent secondary nuclei as the primary nuclei.

2.2.2 SU-8 Photoresist

SU-8 photoresist forms the basis of this entire project, and have as such been devoted a separate sub-section. The project revolved around the nanotopographical structuring – explained in this sub-section – of SU-8 and subsequent incorporation as the base substrate of the neural network recording platform.

Since its introduction by IBM in the nineties, the negative photoresist SU-8 has been used extensively for a number of applications, ranging from microelectromechanical systems (MEMS) and integrated micro-/nano-optics to microfluidic labs-on-a-chip [99–101]. By virtue of excellent chemical stability, structural integrity and good biocompatibility – confirmed by decades of characterisation experiments – SU-8 has become a popular versatile tool in micro- and nanofabrication [102, 103].

Chemistry and Photolithography

Making up the base components of any photoresist, as outlined in section 2.2.1, SU-8 is composed of polymer resin (Bisphenol A Novolac epoxy), solvent (cyclopentanone) and photosensitizer (triarylsulfonium/hexafluoroantimonate salt). Contrary to regular negative photoresists, SU-8 is however characterised as a *chemically amplified* resist. Rather than directly catalyzing cross-linking of the polymer resin upon exposure to light, the photosensitizing triarylsulfonium/hexafluoroantimonate salt in SU-8 acts as a photoacid generator (PAG), generating hexafluoroantimonic acid upon interaction with light in the UV range. Hexafluoroantimonic acid, in turn, protonates expoxide groups in the epoxy resin, activating them to the point where cross-linking reactions will occur at heightened temperatures of 55 °C or above [104]. Single molecules of hexafluoroantimonic acid can catalyze the activation and cross-linking of several epoxy monomers – hence the characterisation chemically "amplified". Figure 2.8 displays an overview of the molecules and reactions involved in the cross-linking of SU-8. Due to the fact that cross-linking does not occur immediately upon exposure, but requires the addition of heat to drive the cross-linking of protonated epoxy groups, photolithohgraphic processes using SU-8 necessitate an added baking step referred to as post-exposure bake (PEB) following exposure. In terms of the overview of photolithography steps listed in section 2.2.1, PEB occurs between step 5 and 6.

One of the major obstacles encountered when utilizing SU-8 in a photolithographic fabrication process is poor adhesion, which in combination with internal stress in the photoresist film can cause it to delaminate from the underlying substrate [105]. Among the particularly challenging substrates to achieve satisfactory SU-8 adhesion on is glass, the substrate used in this project. General optimization of process steps such as soft bake and PEB could improve adhesion properties, but is often found insufficient. Therefore, in addition to PEB, SU-8 resist films on glass often require yet another additional processing step, namely coating with an adhesion promoter [106].

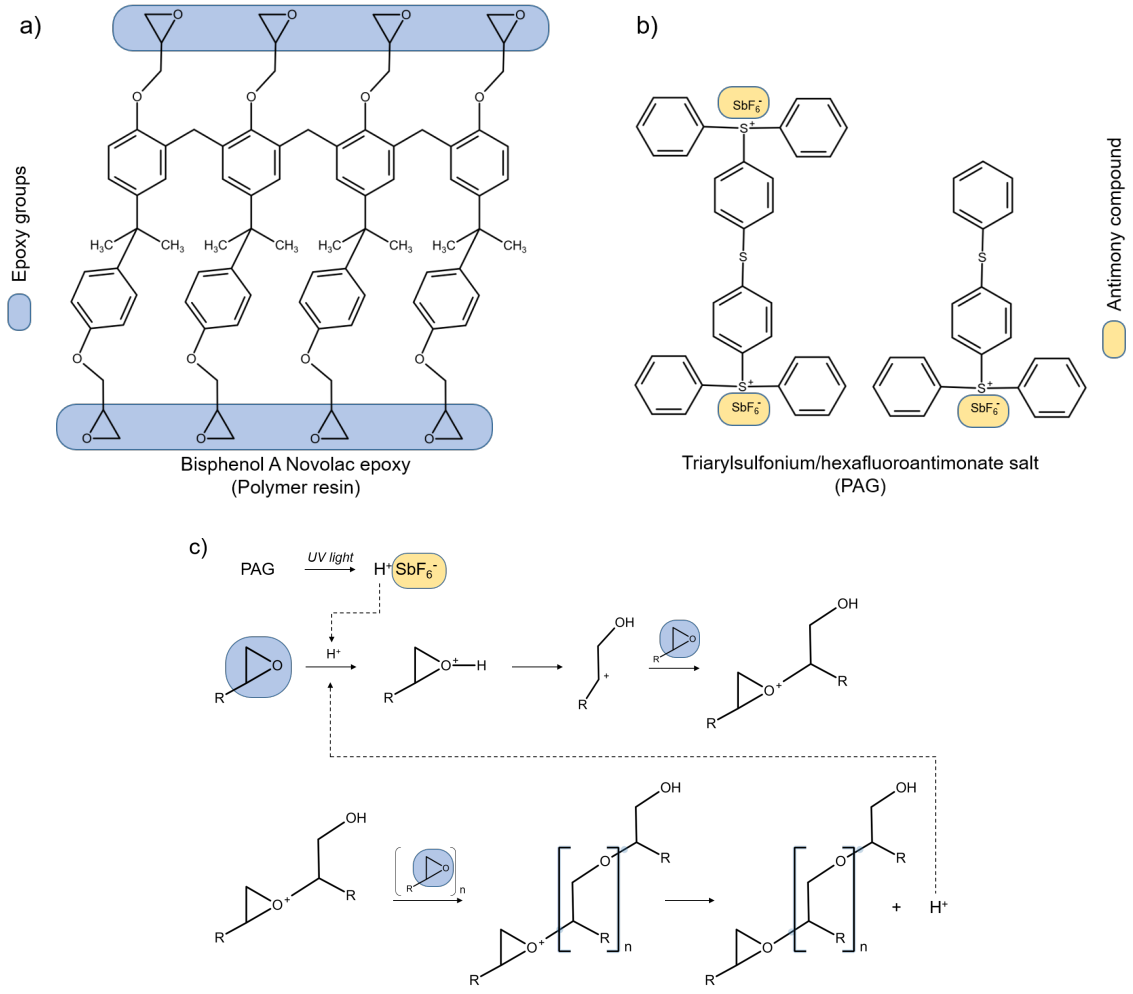

Figure 2.8: Molecular composition for the primary components of SU-8, a) the epoxy polymer and b) the PAG, as well as c) an overview of the chemical reactions involved in the crosslinking of SU-8 during photolithography. PAG generates the acid $H^+SbF_6{}^-$ in interaction with UV light, which protonates epoxy groups of the resin (for simplicity displayed as a single epoxy group with an abbreviated side-group R representing the remainder of the Bisphenol A Novalac epoxy molecule) leading to a series of reactions cross-linking the resin at the epoxy groups upon heating.

Roughening by Etching

As mentioned previously in section 2.2.2, achieving proper adhesion of an SU-8 film to a substrate can prove exceedingly difficult. Conversely, SU-8 is also considered among the most resistant photoresist to removal once cross-linked. Excellent chemical stability renders conventional chemical resist strippers and organic solvents such as acetone largely useless in removing cross-linked SU-8. In stead, researchers have frequently turned to oxygen based RIE [107, 108].

Oxygen based RIE has proven effective in removing cross-linked SU-8 films, but a pure oxygen plasma etch inevitably results in a sample defect characteristic for

plasma etched SU-8. Complete or partial oxygen plasma etching of SU-8 leaves a white residue on the surface of the sample where SU-8 has been etched. Additionally, partial oxygen plasma etching of SU-8 renders the surface of the remaining SU-8 film rough on a micro-/nanoscale, with roughness increasing with the extent of the etch [109]. Although research on the topic is scarce, the source of the white residue and cause of the roughening of partially etched SU-8 is widely believed to be the antimony present in the PAG and its generated acid upon photoactivation, as presented above in section 2.2.2. Antimony compounds are believed to be mechanically rigid enough to largely resist the physical sputtering component of the RIE, and form thermally stable compounds in reaction with the reactive ionized oxygen species in the plasma – i.e. antimony oxide (Sb_2O_3) and atomic antimony with high boiling points of 1425 and 1587 °C respectively [110]. High boiling points result in low vapor pressure of antimony compounds, which means only very small amounts evaporate and leave the surface of the SU-8. Concentrated micro-/nanoscale deposits of antimony compounds appearing on the resist surface effectively shield underlaying resist from etching, creating protruding surface structures of non-etched SU-8, as illustrated in figure 2.9. Supporting the theory of antimony deposits in the resist surfacing during etching and shielding underlying resist to form protruding structures, x-ray photoelectron spectroscopy (XPS) and energy-dispersive x-ray spectroscopy (EDX) performed by several research groups have measured the surface concentration of antimony on SU-8 surfaces to increase significantly after oxygen plasma etching compared to before etching [111, 112].

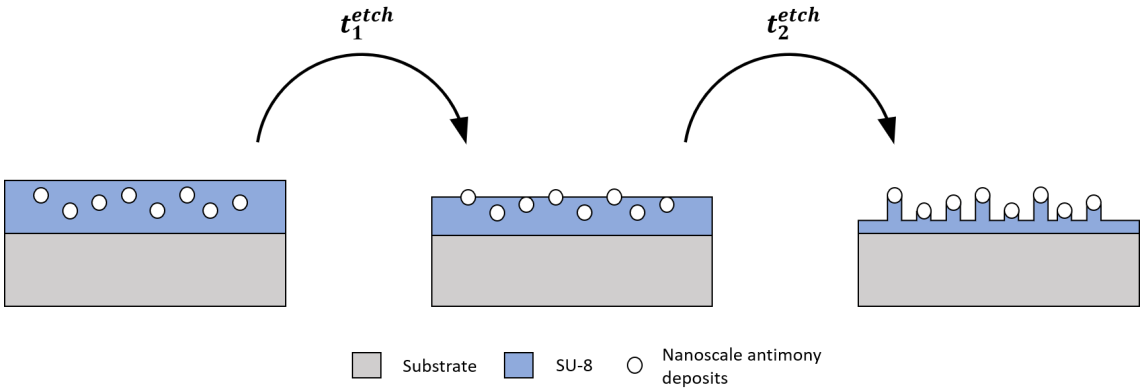

Figure 2.9: Simplified illustration of the principle of non-etchable antimony deposits in the SU-8 film acting as etch masks, protecting SU-8 immediately underneath the deposits. Resulting structures become more protruding with etch time, $t_2^{etch} > t_1^{etch}$.

Adding some fluorides – e.g. CF_4 or SF_6 – to the plasma gas mixture has become the convention when performing oxygen based plasma etching of SU-8. Addition of fluorides drastically reduces the roughening effects and amount of white residue experienced in pure oxygen etches. While no definitive explanation has been offered for how the addition of fluorides counteracts the surface roughening and accumulation of residue, a possible mechanism is the generation of antimony fluorides such as antimony trifluoride (SbF_3) and pentafluoride (SbF_5) in reaction with reactive fluorine ions in the plasma. SbF_3 and SbF_5 have significantly lower boiling points than atomic

antimony and antimony oxide, of 376 and 141 °C respectively, and thus exhibit much higher vapor pressure, evaporating from the surface throughout etching [110].

Generally highlighted as a caveat for SU-8 use, this characteristic etching behaviour can also be exploited to form micro-/nanoroughened surfaces. Intentional RIE-based roughening of SU-8 has been explored for applications in fuel cells, and even to create nanowires by extensive etching and subsequent pyrolysis of the resulting high aspect ratio protruding "wires" of non-etched resist [109, 112]. Forming the basis of this project, it has been hypothesized that the degree of roughness achieved from plasma etching of SU-8 can be reproducibly controlled, producing a variety of topographic surfaces. Control results from tweaking of etch parameters such as gas composition, chamber pressure and power of the electrical field accelerating the plasma ions towards the etched substrate.

2.2.3 Profilometry

Profilometry encompasses a range of surface analysis techniques aimed at capturing the topographical features of a sample, such as height of feature profiles and overall surface roughness metrics.

Mechanical Profilometry

Mechanical profilometry was used in this project to measure thickness of SU-8 films.

As a simple profilometry technique, mechanical profilometry relies on contact-based measurement, capable of resolving surface features in the range of tens of nanometers with high-throughput [113]. A stylus with a diamond tip is kept in contact with the substrate with a small force of a few millinewton and moved in a one-dimensional straight trajectory across the surface. As the tip moves along its trajectory, surface features cause the stylus to be displaced vertically. Displacements are, in turn, detected by a displacement sensor connected to the stylus. Feed-back loops keep the force the stylus exerts on the substrate constant, while the displacement sensor feeds the surface topology information to a connected computer, forming a two-dimensional profile of the surface along the trajectory.

Atomic Force Microscopy

As a more central characterisation technique to the project, atomic force microscopy (AFM) was used for quantitative analysis of nanotopographical surfaces. AFM measurements formed topography maps of nanotopographical SU-8 surfaces, from which a metric of surface roughness was calculated.

Closely related to mechanical profilometry, AFM operates on a similar working principle. A tip attached to a cantilever beam is driven across a surface, while the interaction of the tip with the surface is detected through the deflection of the cantilever to form a topographical map of the surface. In contrast to mechanical profilometry, however, AFM involves scanning over a surface in two dimensions, forming a 3D map of the scanned sample surface rather than a 2D profile along a trajectory. Additionally, while the force exerted on the sample is in the millinewton-range for mechanical

profilometry, it is typically in a far less damaging nanonewton-range for AFM, relying on interatomic *Van der Waals* forces and induced dipole-dipole interactions to deflect the cantilever [114]. Minute deflections of the cantilever are detected by a laser beam reflected off the top of the cantilever hitting a photodiode, as illustrated in figure 2.10, boasting vertical resolution down to the subatomic scale and lateral resolution down to tens of nanometers, depending on the diameter of the tip [115].

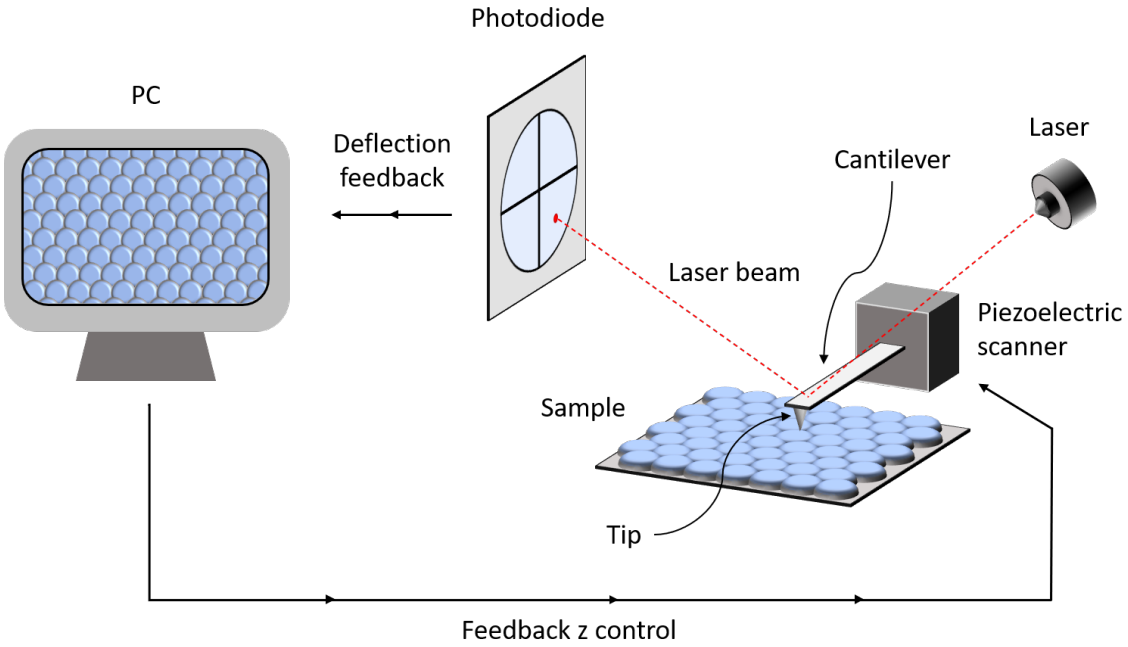

Figure 2.10: Working principle of AFM, here displayed in contact mode. A cantilever with a nanoscale tip attached its end is driven across a sample surface. Surface features deflect the cantilever, shifting a laser beam reflected off the top of the cantilever. The shift in the laser beam results in the beam hitting a spot away from the center of a detecting photodiode, which in turn communicates the shift in the laser beam to a computer. Shifts are translated to a topographic image of the surface by the computer, which also gives a feedback command to the piezoelectric scanner controlling the cantilever to counteract the deflection of the cantilever by moving vertically, maintaining a constant force between the tip and the sample surface.

Two modes of operation are most commonly used in AFM, namely *contact mode* and *tapping mode*. As the name would imply, contact mode relies on direct contact with the sample, in the repulsive domain of Van der Waals forces. Surface features repulse the tip and thus deflect the cantilever. Deflections of the cantilever beam result in a shift of the laser beam focus point on the photodiode away from the center, which in turn feeds the information to a computer controlling the piezoelectric scanner the cantilever is attached to, maintaining a constant force against the sample. Deflection feedback is simultaneously translated to an image representation of the surface. While contact mode is well suited for hard samples, constant contact with the sample as the tip is dragged along the surface gives rise to lateral friction forces, potentially damaging a soft organic sample [116]. Addressing the issue with sample damage induced

by lateral friction, tapping mode is usually the preferred mode for characterisation of soft organic samples. Rather than maintaining contact with a constant force against the sample, the cantilever is driven to oscillate at a frequency close to its resonating frequency, only coming into momentary contact with the sample surface. As the tip approaches the surface during oscillation, Van der Waals forces in the attractive domain and, as the tip comes into contact with the sample, Van der Waals forces in the repulsive domain act on the tip, interrupt the oscillations of the cantilever and introduce a shift in the frequency. The oscillations of the cantilever are recorded through the shifts of the reflected laser beam on the photodiode, and analysed by a computer, forming an image of the surface based on the shifts in oscillation frequency [117]. Feedback to the piezoelectric scanner result in continuous height adjustment of the cantilever to keep the oscillation frequency constant. Due to the fact that the tip only briefly contacts the sample, and experiences minimal lateral movement during contact, lateral shear forces caused by friction are avoided.

In addition to imaging, AFM and the data acquired from its measurements can be used to calculate a myriad of different metrics characterising a surface, including measures of the roughness of a surface. A common surface roughness metric that can be acquired by analysis of AFM data is *arithmetical mean deviation* (S_a), defined as the average absolute value of height deviation from a mid-line for a surface,

$$S_a = \frac{1}{A} \iint_A |z(x, y)| dx dy, \tag{2.1}$$

where A is the total area of the surface.

2.2.4 Scanning Electron Microscopy

For qualitative assessment of nanotopographical surfaces to complement the quantitative measurements by AFM, SEM was chosen.

An SEM replaces the light beams of optical microscopy with a beam of high energy electrons directed towards a sample in a vacuum chamber. Produced by an electron gun acting as a cathode, electrons are accelerated towards an anode by the produced electric field. By adjusting the potential difference between the cathode and anode, the acceleration of the electrons is controlled. Passing through a gap in the anode, the electrons are further condensed in a beam and focused towards the sample by columns of condenser and objective lenses as well as apertures [89]. Lenses, in the case of electron microscopy, refers to current conducting coils that induce a magnetic field acting on the electrons. Scan coils are used to deflect the beam in the lateral x and y-directions, scanning over a patch of the sample surface in a raster pattern.

The electron beam incident on the sample interacts with the sample in multiple ways, producing various detectable signals, such as secondary electrons (SEs), backscattered electrons (BSEs), Auger electrons and x-rays. Differing in the information they provide about the sample, the signalling source is selected based on what properties of the sample are of primary interest. Particularly suited for surface topography investigations, SEs stem from the ionization of sample atoms caused by inelastic scattering interaction with electrons from the incident beam. The SE ejected in the ion-

ization are ejected with a far lower energy than the incident electrons (<50 eV compared to up to several keV for electrons of the incident beam) [118]. Due to their low energy, only the SEs generated in close proximity to the sample surface are able to escape the sample and be captured by the detector. As a consequence of the low interaction volume for production of SEs, high resolution images of surface features can be achieved. In the detector, captured SEs are accelerated towards a scintillator, which emits flashes of light in response to electrons passing through. These flashes of light are in turn captured, where the intensity of light scales with the number of SEs detected, forming a light intensity mapped image as the incident electron beam scans over the surface. An increasing angle of incidence of the electron beam leads to an increase in the portion of SEs capable of escaping the sample, and thus a brighter signal [119]. As a result, surface features with slopes appear brighter in the produced images than flat surfaces, and a topographical representation of the surface forms.

Apart from selecting the appropriate signalling source, several additional parameters must be considered to optimize the quality of produced images in scanning electron microscopy. One of the primary parameters to consider is the acceleration potential. Decreasing the acceleration potential results in a reduced interaction volume, increasing resolution, but can also increase spherical aberrations limiting the resolution of the image. Beam current is another parameter subject to optimization. An increased beam current results in an increased signal count, reducing the effects of noise and improving image contrast, but the increase in the amount of electrons focused in the beam also leads to an increase in repulsive forces between them, resulting in a widening of the beam and lower resolution. Artifacts such as astigmatism and charge accumulation due to insufficient conductance of electrons away from the incidence site must also be considered and counteracted.

2.2.5 Contact Angle Measurement

Establishing an *in vitro* platform for studies of cells, regardless of whether those cells be fibroblasts, muscle cells or neurons, inevitably requires consideration of the wettability of the surfaces the cells will be grown on. Microfluidics with aqueous solutions, such as cell culture medium, require hydrophilic surfaces, making use of capillary forces to facilitate fluid flow through its channels. While the optimum grade of wettability depends on cell type, several studies have also demonstrated a clear effect of surface wettability on cell adhesion and proliferation on a surface [120, 121].

Defined as the angle a liquid forms at the contact point of a three-phase boundary, the contact angle is a measurement of the combination of surface tension of the liquid phase, interphase tension of the gas phase and surface free energy of the solid phase of the three-phase system [122]. Arguably the simplest, and most frequently characterized, three-phase system consists of air as the gas phase, water as the liquid phase and the surface of any solid as the solid phase. In such a system, the liquid-gas interface between water and air is well known. The liquid-solid interface between the solid surface and water is what is of interest – specifically whether and to what degree the surface is hydrophilic or hydrophobic. *Sessile drop* measurements determine contact angle by suspending a droplet of water on the surface to be characterised and monitor-

ing the angle θ formed at the contact point between the edge of the water droplet and the surface, illustrated in figure 2.11. Hydrophilic surfaces attract water and induce the partial collapse of the droplet, resulting in a contact angle of less than 90 degrees. Hydrophobic surface, on the other hand, repel the water and induce a more spherical droplet shape on the surface with a contact angle of more than 90 degrees [123].

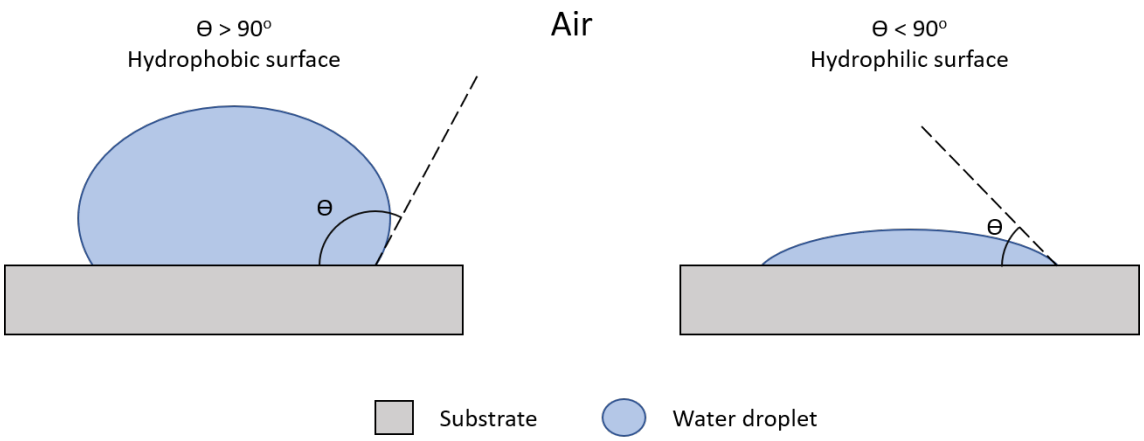

Figure 2.11: Illustration of the simple principle of sessile drop contact angle measurements of wettability with water. A water drop is suspended on the surface under analysis, and the resulting angle θ the edge of the water drop forms with the surface is analysed to determine whether and to what degree the surface is hydrophobic or hydrophilic. Hydrophobic surfaces result in $\theta > 90°$, while hydrophilic surfaces result in $\theta < 90°$.

Chapter 3

Methods & Materials

Materials and methods presented in the following section are strictly related to the fabrication ad characterisation processes, as conducted in this project. All cell work mentioned throughout this thesis was performed by Edevard Hvide, and is documented in his thesis [18].

3.1 Fabrication & Optimization of Roughened SU-8

Fabrication of roughened SU-8 surface chips consisted of primarily two processes - photolithography and reactive ion etching. An initial phase of fabrication was aimed at experimenting with etching parameters and characterising surfaces achieved for a wide range of etching conditions. In the second phase of fabrication, the etching parameters deemed to yield the most interesting results in the context of neural culturing were used to produce chips for seeding of neurons. Outlined in the following section, the photolithographic processes used in the two phases were different, optimized for throughput in phase one and for neural culturing in phase two.

In order to facilitate imaging of neurons cultured on the roughened SU-8 surfaces, 170 µm thick transparent glass cover slips of dimensions 24x24 mm from Menzel-Gläser were chosen as the underlying substrate.

3.1.1 Photolithographic Process

As an initial pre-processing step in the photolithographic process, all glass chips underwent thorough cleaning. Cleaning included submersion and rinsing in acetone and isopropanol (IPA) followed by a 2 minute plasma cleaning with O_2, using the Femto Plasma Cleaner from Diener Electronics at 200 sccm oxygen flow and 40 kHz generator frequency. Dehydration bake was carried out on a hotplate at 150 °C for 5 minutes to remove excess solvents and humidity on the chips. Chips for neural culturing were additionally coated with hexamethyldisilazane (HMDS) (producer Sigma-Aldrich) to improve resist adhesion, an addition which was made after the resist on a couple of chips in the first neural culturing set disassociated from the glass substrate while in cell medium. Glass cover slips were placed in a desiccator together with a vial containing a drop of HMDS. The desiccator was pumped to vacuum by a vacuum pump, and left

at vacuum for 10 minutes, allowing the HMDS to evaporate from the vial and adsorb on the substrate surfaces, before ventilating the chamber and removing the samples.

Following the cleaning and pre-processing procedure, SU-8 2010 (45% solids made by diluting SU-8 2100 75% solids from MicroChem Corp. with cyclopentanone from Sigma-Aldrich) was manually poured onto the cover slips to form a puddle of resist covering approximately two thirds of the cover slip. Distributing the resist evenly across the glass substrate, slips were spun at 3500 rotations per minute (RPM) for 30 seconds preceded by a 1000 RPM/s ramp-up phase lasting for 3.5 seconds, to achieve a resist thickness of around 10 µm. Soft bake was subsequently carried out in two steps on separate hotplates, first at 65 °C for 1 minute and then at 95 °C for 3 minutes.

Two different methods and accompanying equipment were used for exposure of the resist:

Flood Exposure in Maskaligner

Initially, exposure was carried out with i-line (365 nm) flood exposure from a mercury lamp in the MA6 Maskaligner from Karl Süss. In each exposure run, 4 glass cover slips were placed on a 4" silicon carrier wafer mounted by vacuum seal to the exposure stage in the MA6 Maskaligner, and were simultaneously exposed with a dose of 150 mJ/cm^2. Chips were exposed in their entirety, rendering all SU-8 insoluble. Exposure was followed by post-exposure bake on hotplates at 95 °C for 3 minutes.

Patterned Exposure in Maskless Aligner

After alterations to the photolithographic process, exposure was moved to a maskless aligner. Exposure was carried out in the MLA 150 maskless aligner from Heidelberg Instruments according to a simple design created in the software Clewin 4, exposing a 8 mm ∅ circle in the center of the chip. The extent of the SU-8 film on the glass substrate was chosen to facilitate bonding of petri-dishes with 14 mm ∅ holes on their bottom to the chips, as illustrated in figure 4.2. Due to the fact that SU-8 resist is far less sensitive to the 375 nm light emitted in the MLA 150 than the traditional i-line exposure commonly applied for SU-8, exposure dose in the MLA 150 had to be set to a comparatively high 5000 mJ/cm^2. Exposure was followed by a two-step post-exposure bake on hotplates, at 65 °C for one minute and then at 95 °C for 4 minutes. Chips were consequently developed to remove resist outside the exposed area. Two beakers of the resist developer chemical mr-Dev 600 from Micro resist technology GmbH were prepared, along with one beaker of IPA. Chips were submerged in the mr-Dev 600 solution in one beaker for 55 seconds, before being transferred to the other for another 55 seconds of development, for a total development time of 1 minute and 50 seconds. Development in developer was immediately followed by submersion in and rinsing with IPA to stop the development process and ultimately drying using a nitrogen gun.

Control chips of planar SU-8 were additionally plasma cleaned for 1 minute in 200 sccm O_2 plasma at generator frequency 2 kHz to remove organic contaminants and increase the wettability of the surface.

3.1.2 Roughening by Etching

Roughening of SU-8 was performed by means of etching with a primarily oxygen based plasma in the Plasmalab System 100 ICP-RIE 180 from Oxford Instruments. Glass cover slips with SU-8 were attached to a 4" quartz carrier wafer by rubbing a small amount of fomblin oil on the backside of each glass slide, acting as a weak glue to the carrier. Remnants of fomblin oil were removed by cleaning carefully with cotton swabs soaked in IPA and ethanol following etching. Prior to each round of etching experiments, the etch chamber was first cleaned with a 15 minute etch in 80 sccm O_2 with just the carrier wafer loaded.

Three parameters were kept constant throughout the etching runs, namely the temperature, at 20 °C, main coil power, at 1000 W, and oxygen gas release rate, at 80 sccm. Parameters tuned for optimization of the etching process included chamber pressure, p, bias power, P_{bias}, etching time, t, and release rate of gas added in addition to oxygen, q_{gas}.

3.2 Integration on MEA Neural Recording Chips

In line with the overarching goal of incorporation and utilization of roughened surfaces on the neural network recording platform this project aimed to advance, MEA neural recording chips used by the research group, with minor design changes, were fabricated and used for testing neural network behaviour on roughened SU-8 surfaces versus non-roughened ones. The particular neural recording chip chosen was designed for a two-chamber microfluidic set up.

Apart from the inclusion of a roughened SU-8 surface layer with the fabrication processes involved, the fabrication of MEA neural recording chips was largely based on previous work. Metallization and the photolithographic process used to create a metallization mask was based on the work of Nicolai Winter Hjelm. Electrodeposition of platinum black electrodes was based on previous work by the author of this thesis, carried out throughout the completion of his project thesis.

3.2.1 Design

The photolithography design software Clewin 4 was used to create the design for the photolithographic processes of this work. Shown in fig. 3.1, the design for the neural recording chips was based on one created by Nicolai Winter-Hjelm, with certain changes to facilitate a more consistent fabrication and electrodeposition. Forming the patterns of the photoresist masks to be used for metallization and exposure of the SU-8 layer, the design consisted of two layers, both of which were inverted before exposure due to the use of negative resist. Layer 1 corresponded to the first photolithographic process, creating a resist mask for metallization. All features in layer 1 of the design would thus be translated to metal present on the fabricated chip. Layer 2 corresponded to the second process, patterning the SU-8 layer. Features appearing in layer 2 represents open areas not covered by SU-8, while the remainder of the substrate would be covered. Designed for 4 inch circular wafers, features and dimensions were

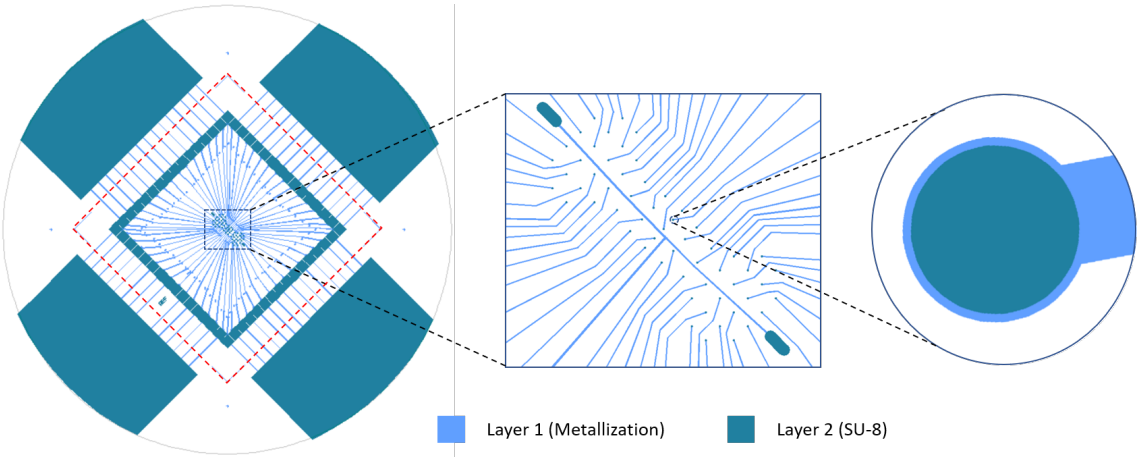

Figure 3.1: Overview of the design used in the photolithographic processes involved in the fabrication of MEA neural recording chips with SU-8 surfaces. Light blue features correlate with layer 1 of the design, the metallization mask, and would be covered in metal. Dark green features correlate with layer 2 of the design, the SU-8 layer, and signify openings in the SU-8 film down to the underlying metal. Dashed red lines illustrate where the wafer will be cut after completed microfabrication.

as follows; 4 orthogonally situated large contact pads, 38.5 mm wide and stretching up to 23 mm in to the wafer, present in both layer 1 and 2. These were in turn connected by 150 µm wide and 8.5 mm long wires in layer 1 to 15 smaller contact pads each (60 in total) of dimensions 2.2 x 2.2 mm, present in both layer 1 and 2. Wires of width 30 µm stretched from the contact pads towards the middle of the wafer, connecting the contact pads and electrodes in layer 1. Wire width was originally 20 µm, but was changed to 30 µm due to problems with narrow wires breaking. At the end of each wire was a circular electrode of diameter 55 µm and 50 µm in layer 1 and 2, respectively. The 5 µm larger electrode diameter in layer 1 (for metallization) compared to layer 2 (opening in SU-8 layer) was designed to account for some misalignment of the second photolithographic process. One wire connected to a set of two larger electrodes, acting as reference electrodes, one in each microfluidic chamber, in the neural recording set up.

Alignment marks were used to facilitate alignment of the second photoresist exposure to the existing structures from the metallization step. Additionally, markers were added to guide the cutting of the wafer after completed microfabrication, cutting away the large contact pads connected to several electrodes each and leaving a square chip with the individual contact pads for individual electrodes, as necessary for neural recording.

3.2.2 Metal Deposition of Contacts, Wires and Planar Electrodes

As a first step in the photolithographic process for the metallization mask, the substrate – 4" 1 mm thick borosilicate wafers from Plan Optic AG – was thoroughly cleaned. Cleaning included submersion and rinsing in acetone and isopropanol (IPA) followed by a 5 minute plasma cleaning with O_2, using the Femto Plasma Cleaner from Diener

Electronics (used whenever referring to plasma cleaning from here on out) at 100sccm oxygen flow and 20 kHz generator frequency. Following the cleaning procedure, a dehydration bake was carried out on a hotplate at 100 °C for 2 minutes. Approximately 3 mL of MaN-440 photoresist was deposited on the wafer before initiating a spin cycle of 3000 RPM for 42 seconds with a 500 RPM/s ramp-up lasting for the first 6 seconds of the cycle, to achieve a resist thickness of around 3.5 µm. Soft bake was subsequently carried out on a 95 °C hotplate for 5 minutes, followed by a 10 minute rest to allow the resist to settle. Using the MLA 150 maskless aligner from Heidelberg Instruments, the resist was exposed with a 405 nm laser at a dose of 2400 mJ/cm^2 according to the layer 1 design described in section 3.2.1. After a 10 minute rest, the resist was developed by submersion in a MaD-332/S developer solution for a period of 1 minutes and 40 seconds, and rinsed thoroughly in DI water to stop development.

Prior to metallization, the wafer was plasma cleaned with 100sccm O_2 at 20 kHz to remove organic contaminants such as dust and resist residues. Subsequent evaporation of 50 nm of titanium, as an adhesion layer, followed by 100 nm of platinum onto the wafer was performed, using the electron beam mode for the E-Beam Evaporator & Sputter from AJA International Inc. Deposition was set to a rate of 5 Å s^{-1}. Removing the metallization mask, as well as the metal deposited on top of the mask resist, lift-off was carried out by submersion in acetone for approximately 5 minutes. The wafer was rinsed in IPA to remove traces of acetone.

3.2.3 Application of SU-8

Prior to the photolithographic process involved in applying SU-8 on the neural recording chips, the same pre-processing procedure was followed as described in section 3.1.1, involving cleaning of the chip, dehydration bake and treatment with HMDS.

For planar SU-8 control chips, a more diluted solution of SU-8 was used. To reduce distance between cultured neurons on top of the resist and the base of the platinum electrodes at the bottom of the electrode holes in the resist, a thinner layer of SU-8 was deposited than for the roughening etch parameter testing. Approximately 4 mL of SU-8 2001 (25% solids made by diluting SU-8 2100 75% solids from MicroChem Corp. with cyclopentanone) was deposited on the chips with a pipette, and spun in a cycle of 500 RPM for 10 seconds, followed by 30 seconds at 6000 RPM. Resulting resist thickness was around 1 µm. Chips to be roughened by etching were prepared with the same dilution ratio, SU-8 2010, and spin parameters as described in etch testing experiments, resulting in a 10 µm thick film. Soft bake was performed in two steps, a 1 minute bake at 65 °C followed by a 3 minute bake at 95 °C. The MLA 150 maskless aligner from Heidelberg Instruments was used for exposure, exposing the chips with 375 nm wavelength light up to a total dose of 5000 mJ/cm^2. Exposure was followed by a two-step post-exposure bake at 65 °C for 1 minute and 95 °C for 3 minutes. Chips were subsequently developed by submersion in mr-Dev 600 from Micro resist technology GmbH. 1 µm SU-8 chips were developed for 25 seconds in one beaker and 20 seconds in another, for a total development time of 45 seconds, while 10 µm SU-8 chips were developed for a minute in each beaker. After the designated development time, development was immediately stopped by rinsing chips in IPA.

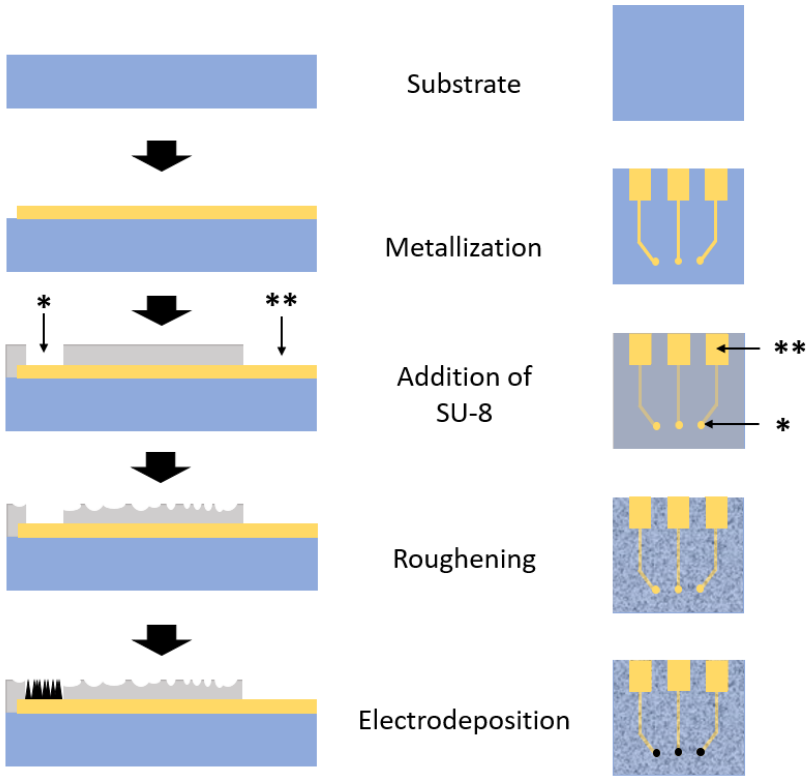

Figure 3.2: Schematic overview of the primary process steps involved in the fabrication of SU-8 topographical neural recording chips. The top view of the chip presented on the right hand side is a simplified and reduced version of the design with contact pads, wires and electrodes. Platinum is deposited on the borosilicate glass substrate, according to the design of the MaN-440 resist mask. An SU-8 layer is deposited on the chip to cover all areas other than contact pads and electrodes, and subsequently roughened by etching. Finally, electrodeposition of platinum black is performed on the electrodes

3.2.4 Electrodeposition of Platinum Black

Electrodeposition was carried out using the pump system, elecrolyte bath setup, counter electrode slot (mounted with a large Pt plate counter electrode), paddle agitator and temperature controller of a 2-4-inch Silicon Wafer Plating Electroplating Laboratory system (PP-type) from Yamamoto. During deposition, the wafer was placed in a custom built wafer holder and partially submerged in the electrolyte bath. A wire connected to the potentiostat was clamped on one of the large contact pads with a conducting crocodile clamp, as shown in figure 3.3. While the set of 15 electrodes to be deposited on were submerged in the electrolyte, the corresponding contact pads (both the large and the 15 individual ones) were kept above the electrolyte, thus ensuring that platinum black growth only occurred on the electrode and not the contact pad. Between each deposition, the wafer was taken out of the bath, cleaned with DI water and dried with a nitrogen gun before switching the connection to the contact pad of the next electrode set to be deposited on.

As the potentiostat for electrodeposition with controlled potentials, a PalmSens4

from PalmSens was used. A Red Rod REF201 Ag/AgCl Reference electrode from Hach was used as the reference electrode. The electrodeposition solution contained 2.5 mM chloroplatinic acid diluted in watera (H_2PtCl_6, 8wt% H_2O from Sigma-Aldrich). The temperature was set to 30 °C, and the paddle agitator was set to stir back and forth in the solution at an RPM of 60. Deposition was carried out in a chronoamperometric set up, with potential set to −0.4 V. Deposition time was 5 minutes for chips with planar SU-8 surfaces and 3 minutes for chips with roughened SU-8 surfaces.

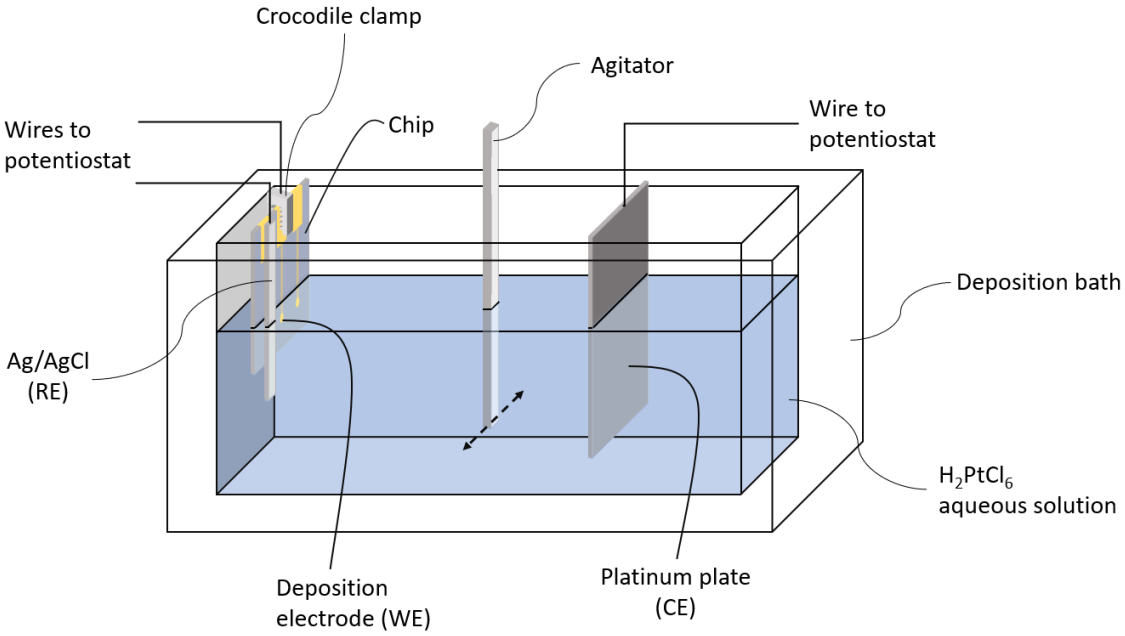

Figure 3.3: Simplified schematic of the three-electrode electrodeposition setup used in this project. The wire from the potentiostat is clamped with an electrically conducting crocodile clamp on to the contact pad (above the electrolyte soltion) of the electrodes on which deposition of platinum black will occur (suspended in the electrolyte solution) on the chip. The connected deposition electrodes on the chip act as working electrode (WE) and a plate of platinum acts as counter electrode (CE). An Ag/AgCl reference electrode (RE) is suspended in the electrolyte bath adjacent to the chip. A paddle agitator moves back and forth at a set rate to stir the solution around in order to ensure an even concentration of electrolyte across the whole bath.

3.2.5 PDMS Microfluidic Culture Wells

Forming the microfluidic chambers for neuron culturing, PDMS structures were made using a mold created by Nicolai Winter Hjelm. 70 g of PDMS elastomer was mixed with 7 g of Dow Cornings Sylgard 184 curing agent and stirred manually with a spoon for 5 minutes to create a uniform mixture. After stirring, the mixture was put in a dessicator connected to a vacuum pump and left in vacuum for for 15 minutes to draw out air bubbles, followed by pouring in to a mold and another 10 minutes in the dessicator. Remaining bubbles having surfaced during treatment in vacuum were drawn out of the mixture by lightly blowing on the surface with a rubber bulb attached to a pipette. To solidify the PDMS, the mixture was baked at 65 °C for 4 hours. Each run yielded 10 complete PDMS structures, with 2 culturing wells each and channels connecting the wells, according to the 2-node neural network culturing design.

PDMS structures were bonded to the fabricated and cut up MEA neural recording chips, completing the fabrication steps of the neural network recording platform. Chips and PDMS structures were first plasma cleaned at 100 sccm oxygen flow and 2 kHz generator frequency to functionalize both surfaces. Immediately after plasma cleaning, two drops of ethanol were pipetted on the chips to facilitate alignment, and PDMS structure chambers were aligned to the MEAs of the chips under a inverted microscope. Bonding was performed on a heated 95 °C hotplate while applying a light pressure to the top of the PDMS structure. Using a pipette, bonded microfluidic structures were filled with DI water to maintain hydrophilicity

3.3 Characterization

3.3.1 Mechanical Profilometry

Mechanical profilometry was used to measure the height profiles of the photoresist prior to and following etching to determine etch depth and etch rate for certain etching conditions. Throughout this project, a Dektak 150 Profilometer from Veeco was used with a 12.5 μm radius stylus. Scan length varied between 200 and 500 μm, with scan duration set to 60 s. Force was set to 3.00 mg and vertical deflection range to 65.5 μm.

3.3.2 Atomic Force Microscopy

In order to evaluate degree of roughness, AFM measurements were taken of the roughened SU-8 surfaces. All measurements were taken with the Dimension Icon AFM from Bruker using the ScanAsyst mode, which combines tapping and contact mode and automatically optimizes parameters such as feedback gain, setpoint and scan rate for high quality imaging [124]. Two different probes were used depending on the approximate degree of roughness of tested samples. For less rough samples, the ScanAsyst Air probe from Bruker was used, with resonance frequency 70 kHz and spring constant 0.4 N/m. Rougher samples were measured with the RTESPA-300 probe from Bruker, with resonance frequency 300 kHz and spring constant 40 N/m.

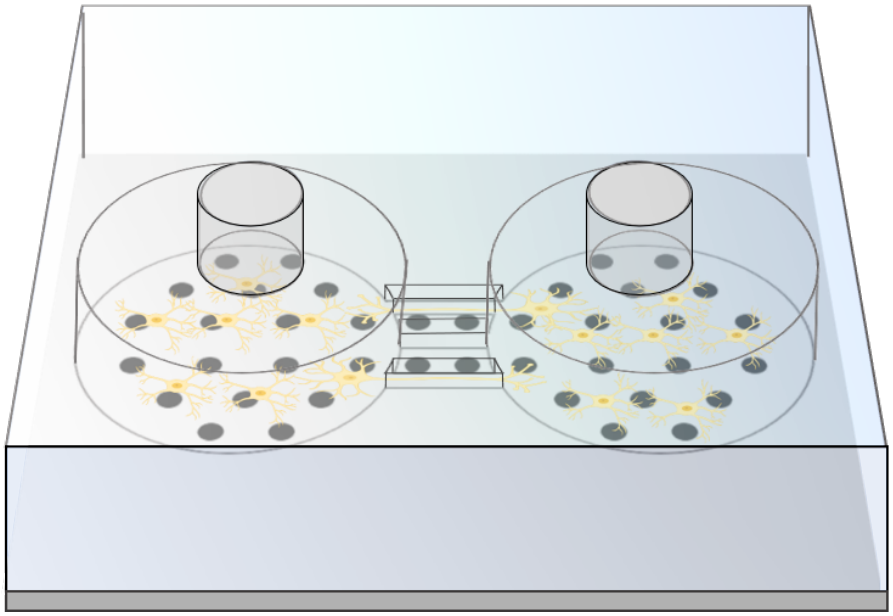

Figure 3.4: Simplified illustration of central region on complete two-node neural network recording platform. PDMS structure consists of two microfluidic compartments interconnected by microchannels only permissible to axons. Culturing chambers and channels connecting them are covered by microelectrodes recording spiking activity within chambers and passing between chambers through axons traversing the channels. Seeding of neurons and subsequent supply of nutrients is facilitated by holes in the PDMS structure leading down to the culturing chambers.

Acquired images were processed and analyzed, extracting surface roughness measurements, using the software Gwyddion. Processing of images consisted of performing the same three data cleaning steps for all measured samples. First, the surface leveling function was used, which compensates for potential tilt of the sample during measurement by performing mean plane substraction. Second, row alignment was performed, compensating for jumps in height the AFM tip occasionally does when starting the scan of a new row in the raster scan pattern. Lastly, correction of horizontal scars was performed, compensating for "scars" of lost data in the measurements often resulting from sudden drastic changes in cantilever deflection caused by particularly large and sudden surface features. Surface roughness measured by S_a is automatically calculated by the software and given in the overview of statistical data for a given measurement.

3.3.3 Scanning Electron Microscopy

An SEM was used for high magnification imaging of SU-8 surfaces, to evaluate the nano- and microscale topographical structures of etch roughened surfaces. The SEM used for this project was the APREO Field Emission Scanning Electron Microscope (SEM) from FEI, with all images being taken in the immersion mode setup.

Prior to imaging, the 24 x 24 mm chips were manually cut into smaller samples, of approximate dimensions 6 x 6 mm, using a diamond tip scriber. Samples were then coated with a 2 nm conducting metal layer of Pd/Pt using a 208 HR B Sputter Coater

from Cressington, to prevent a build up of charge at the site of imaging. Coated samples were mounted on a 8 mm ∅ sample holder with double sided copper tape, which in turn was mounted on the SEM sample stage. Samples were electrically connected to the sample stage by conductive copper tape attached at one end to the top of the sample and at the other to the sample stage. Beam current was set to 6.3 pA and acceleration voltage to 2 kV. All images were acquired using secondary electrons as the detected signal.

Simple image processing, including the addition of scale bars, was performed in the Fiji ImageJ software.

3.3.4 Drop Shape Analysis

The hydrophilicity of SU-8 surfaces, roughened and planar, was tested by means of contact angle measurements. Using the Drop Shape Analyser DSA25 from Kruss in the sessile drop mode, 20 µL drops of water were ejected from a syringe and suspended on the chip surfaces. Interaction of the drop with the surface was captured with a built in camera and automatically analysed to determine contact angle.

Chapter 4

Results

Outline

In the following chapter, the experimental results of this work will be presented. By and large, the experimental work of this project can be divided in to three separate phases, and the results presented in this chapter will be structured accordingly. The first phase was centered around establishing general photolithography protocols for fabrication of SU-8 films on 24x24 mm glass slips and integration with cell culturing. Following the protocols established in the first phase, the second phase shifted the focus to experimenting with a wide variety of etch gas compositions and etch parameters for surface-roughening of SU-8. Etch conditions were tuned to achieve a multitude of surface topographies, with the aim of determining which topographies had the most desired effect on neural culturing. The final phase was aimed at developing a complete MEA neural network recording platform with SU-8 surfaces, exploring the viability of using SU-8, both roughened and planar, as an insulating layer during electrodeposition and subsequently as the bottom surface in a microfluidic PDMS platform. Additionally, neurons were cultured on MEA chips with both planar SU-8 surfaces and SU-8 surfaces roughened with the set of parameters deemed most promising from the second phase, to look for electrophysiological differences in networks grown on planar versus roughened surfaces. Results presented for each phase will have an emphasis on the aspect of fabrication, and present a summary of the main results obtained by Edevard Hvide in neural culturing on fabricated platforms. A thorough description of the cellwork and in-depth analysis of results related to neural culturing can be found in the thesis written by Hvide [18].

4.1 Phase 1 — Establishing Protocols

Prior to experimentation with neural culturing on roughened topographic SU-8 surfaces, general fabrication protocols for the photolithography of SU-8 films had to be established, including integration with culturing of neurons.

Having prepared two dilutions of SU-8 resist, namely SU-8 2010 and 2001, spin coating was first optimized, aiming at resist films of thickness 10 and 1 µm respectively. Illustrated by mechanical profilometry measurements in figure 4.1, spin cycles mentioned in section 3.1.1 were found to yield resist thicknesses of 9.95 and 1.08 µm respectively for prepared films of SU-8 2010 and SU-2001, supporting the nominal film thickness given by the recipe.

Initially, films covering the full 24x24 mm surface of the glass slides were exposed in their entirety with flood exposure in a maskaligner following parameters suggested in SU-8 resist datasheets, with i-line exposure of dose 150 mJ/cm^2 [125]. However, flood exposure of the entire SU-8 film covering the glass substrate proved incompatible with the method used for neuronal culturing on the fabricated samples. Petri-dishes were bonded to the substrates by applying parafin around the edges of the 14 mm ∅ hole on the bottom of the petri-dish and pressing it against the substrate to form a seal. Owing to capillary forces, micro- and nanostructures on the roughened SU-8 surfaces pulled parafin from the edges to the center of the hole in the petri dish, detrimentally contaminating the open SU-8 surface area where neurons were to be cultured. In order to address the issue, a new exposure protocol had to be established, outlined in section 3.1.1. Rather than exposing the entire substrate surface, only a central region of 8 mm ∅ was exposed, thus enabling petri dish bonding directly on the glass around the SU-8 film, as illustrated in figure 4.2. Exposing with 375 nm wavelength laser – to which SU-8 is far less sensitive than the 365 nm in i-line exposure – in a maskless aligner, doses of 1000, 3000 and 5000 mJ/cm^2 were tested. Only 5000 mJ/cm^2 yielded fully cross-linked SU-8 resistant to dissolution during development.

Attempting neuronal culturing on surface roughened chips, SU-8 film on 8 out of 9 chips detached completely from the glass substrate while placed in the cell culturing solution, indicating poor adhesion. Several alterations of the photolithographic process were subsequently made in the attempt to improve resist adhesion. Dehydration bake at 150 °C was extended from 3 minutes to 5 minutes, based on the hypothesis that 3 minutes was insufficient to drive off residual moisture from the surface of the glass substrate before deposition of SU-8. Water on the substrate surface repels the photoresist solvent, and thus inhibits proper adhesion of resist. Allowing a more gradual evaporation of residual solvent in the resist, thus inducing less film stress, both soft-bake and PEB time was changed from a single step to a two-step process, adding a preliminary 1 minute 65 °C bake to both processes before baking at the final temperature of 95 °C. Finally, a pre-processing step for the glass substrate was added after dehydration bake and before spin coating of SU-8 – coating with a monolayer of the adhesion promoter HMDS, rendering the surface hydrophobic and thus improving resist wetting and adhesion [126]. Proving effective in improving the adhesion properties of SU-8 films to the glass substrate, these alterations resulted in the detachment of only 3 out of 16 SU-8 films during neuronal culturing, a significant reduction.

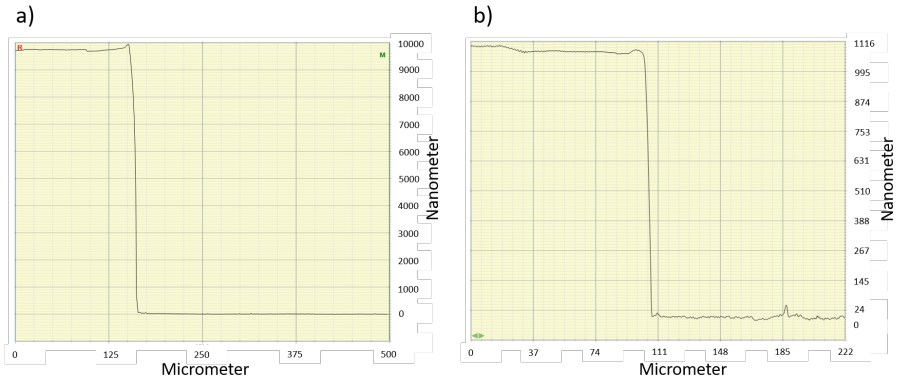

Figure 4.1: Mechanical profilometry measurements of the thickness of SU-8 a) 2010 and b) 2001 films after complete photolithographic process, measured from the top of the resist film to the glass substrate beneath at the edge of the resist film.

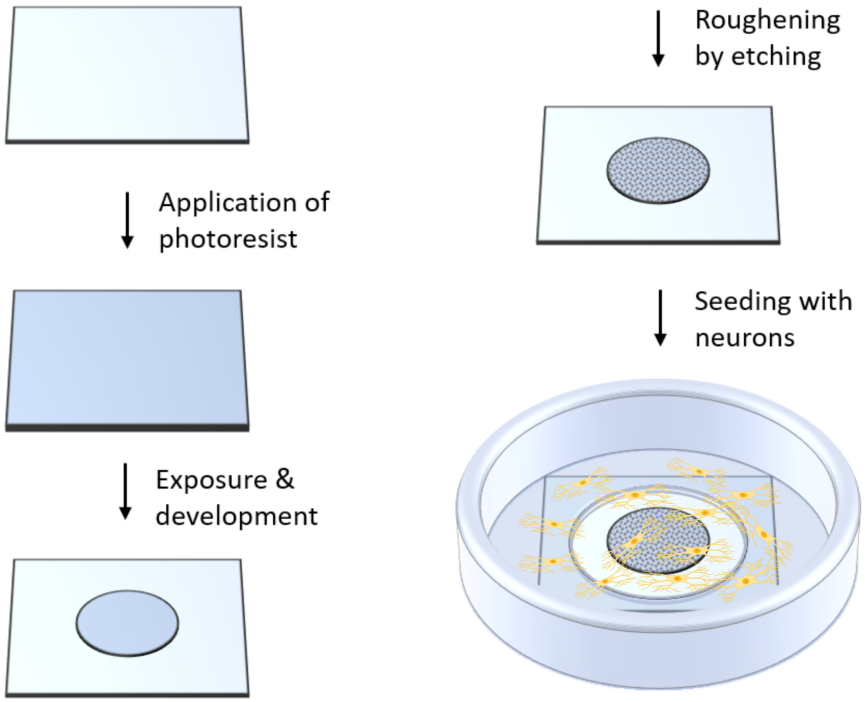

Figure 4.2: Schematic overview of the process steps involved in the fabrication of roughened SU-8 surfaces and subsequent culturing of neurons. SU-8 film is applied and patterned through exposure and development to a central circle of the glass slide, and roughened through etching. A petri-dish with a hole larger than the SU-8 structure on its bottom is then bonded to the glass slide, forming a platform for culturing of neurons.

4.2 Phase 2 — Tuning Etch Parameters for Optimization of Topography

Having developed protocols for photolithography compatible with the neuronal culturing platform, focus in the second phase of the project shifted to experimentation with plasma etch roughening of SU-8 to produce different nanotopographic surfaces. With the aim of improving the physiological relevance of a neural network recording platform by incorporating these nanotopographic surfaces, surfaces were evaluated on two primary criteria: Biocompatibility was one – healthy neurons is a prerequisite for the formation of physiologically relevant neural networks. As the second criteria, surfaces were evaluated on whether they induced in cultured neural networks more hallmarks of behaviour characteristic for networks of the brain – as outlined in section 2.1.4 – than planar control surfaces.

4.2.1 Etching in Pure Oxygen Plasma

Based on the work of Oruganti et al. in 2013, pure O_2 plasma etches were chosen for the first round of surface roughening [109]. Without the addition of fluorinated gases to the plasma mixture, only three parameters were left – i.e. chamber pressure p, bias power P_{bias} and etching time t. Further reducing the amount of parameters to tune, chamber pressure and bias power were fixed to $p = 20\,\text{mTorr}$ and bias power $P_{bias} = 300\,\text{W}$, respectively, leaving etching time as the only variable.

SEM micrographs of three samples etched in pure oxygen with the aforementioned bias power and chamber pressure for an etch time of 1, 3 and 5 minutes are displayed along with a sample of planar non-etched SU-8 for reference in the first two columns of figure 4.3. As is apparent from the SEM micrographs, strictly altering the etch time while keeping all other parameters costant during pure oxygen etching resulted in similar structures, but at different size scales. Consistent with theory presented in section 2.2.2, increasing the extent of the etch by extending the etch time led to the formation of more protruding, larger aspect-ratio surface features. Demonstrated in figure 4.3d, none of these surface structures were present in the SU-8 film prior to plasma etching.

AFM measurements were taken of the surfaces of the samples, and are displayed in rightmost column in figure 4.3. Acquired AFM measurements were further analysed – see section 3.3.2 for work flow – to calculate surface roughness given as arithmetical mean deviation S_a, as defined in section 2.2.3. Based on measurements of two samples per etching time parameter and 3 measurements at different places on each sample, samples etched for 60 seconds resulted in $S_a = 26\pm4\,\text{nm}$, 180 seconds in $S_a = 72\pm6\,\text{nm}$ and 300 seconds in $S_a = 152\pm8\,\text{nm}$. It should however be noted that AFM measurements strictly capture the outline of surface features, incapable of measuring the intricacies of porous structures. Analogous to measuring a tree with all its branches as a solid pillar with width defined by the widest reaching branch and height by the tallest reaching, AFM measurements underestimate the roughness of porous structures. Hence, the measured surfaces were likely significantly more rough than the AFM data indicated. Planar non-etched SU-8 control samples proved nominally

flat at a surface roughness of $S_a = 0.25 \pm 0.01$ nm.

Upon culturing neurons on chips roughened with the 3 different etching times along with non-etched control chips, all roughened surfaces were found to have detrimental effects on the neurons. After two days *in vitro* (DIV), the vast majority of neurons cultured on all surfaces had not adhered to the surface and had undergone necrosis, and thus the cultures were promptly terminated. Poor cell viability was attributed to the surface structures, even for the samples with the lowest roughness out of the three sets, being too protruding and extreme, preventing adequate cell adhesion to the surfaces. Brunetti et al. in 2010 determined roughness values S_a of over 80 nm to be inhibiting to adhesion for neuroblastoma cells on gold surfaces [64]. Similarly, Khan et al. in 2005 found adhesion of primary cortical neural cells on silicon surfaces to decrease rapidly at roughness values over 100 nm [127]. While the samples etched for 1 minute were measured to a surface roughness below both of these values, at $S_a = 26 \pm 4$ nm, the threshold for adhesion could be lower for the combination of cell type and substrate in this project – primary neural stem cells and SU-8. Expanded on in section 5.2, an alternative theory for the extensive cell death revolves around the potential cytotoxic effect of a high surface concentration of antimony resulting from the roughening etch. While none of the surfaces proved promising for integration on the neural network recording platform, the results steered the project on-wards in the direction of less rough surfaces.

Rather surprisingly, neurons cultured on planar control chips also exhibited cell viability lesser to expectations, though better than for the roughened samples. Considering the proven biocompatibility of SU-8, low wettability caused by organic contaminants on the untreated planar surfaces was proposed as an explanation for the poor cell viability.

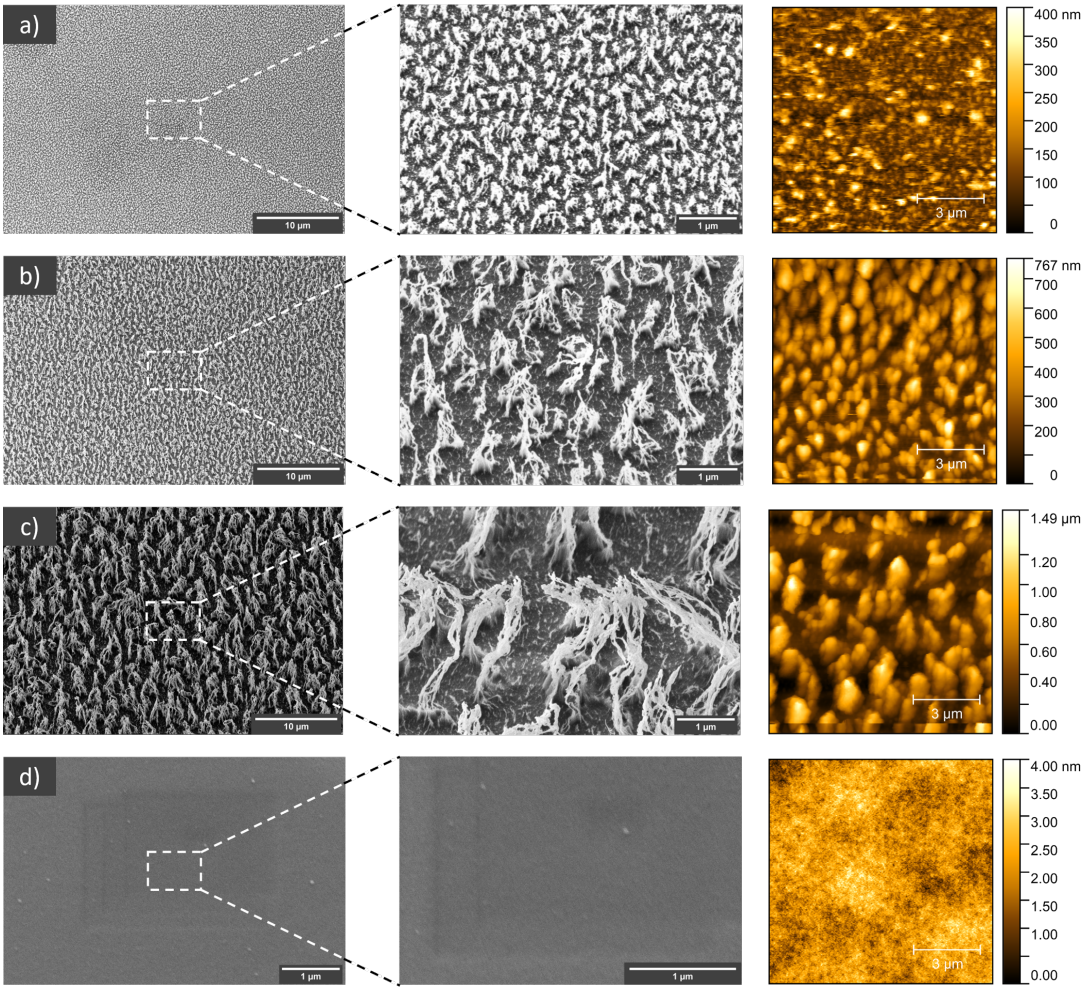

Figure 4.3: From left to right: SEM micrographs of SU-8 film surfaces at two magnifications, followed by AFM measurements of the same surface. For samples a-c, SEM micrographs were taken at 8 000x and 35 000x magnification, and imaged surfaces were achieved by etching in pure O_2 plasma with pressure p=20 mTorr and bias power P_{bias}=300 W for time a) $t = 60$ s, b) $t = 180$ s and c) $t = 300$ s. Sample d) was a non-etched control chip of planar SU-8, imaged at 35 000x and 65 000x magnification.

4.2.2 Introduction of Fluorinated Gases

After attributing poor neural cell viability to the protruding surface features and high roughness values resulting from the pure oxygen etches tested in section 4.2.1, priority was put on reducing the extent of the roughening. In the work of Rasmussen et al. in 2013, etching of SU-8 was optimized to minimize surface roughness while adding SF_6 in the plasma gas mixture along with O_2 and fluorine in the gas mixture was proposed as the key to reducing the roughening. Inspired by this work – and driven by the objective to produce surfaces of less rough and protruding nanotopographies – fluorinated gases were introduced in the etch.

In a phase of high-throughput testing, rather than testing each set of etch para-

meter on three samples, a single etching condition was only tested on a single sample. An overview of tested etch conditions is listed in table 4.1. For ease of referral, all etch conditions will from here on out be referred to by their given abbreviated name, as listed in the table. While a sample etched with conditions SF_6:C1 was deemed too planar, ruling out SF_6 in subsequent experiments, addition of different concentrations of CF_4 and CHF_3 was found to produce surfaces of non-porous topographies on the nanoscale. The significantly less extensive pure oxygen etch O_2:C2, featuring reduced etch time, increased chamber pressure and greatly reduced bias power compared to the pure oxygen etches presented in section 4.2.1, was also found to result in less protruding and porous topographies. Figure 4.4 displays SEM micrographs of a selection of achieved topographies. Three etching conditions, O_2:C2, CHF_3:C2 and CF_4:C2, were selected for roughening of samples for the next batch of neuronal culturing based on a qualitative assessment of the resulting surfaces as less rough and porous, and thus dissimilar enough to the previous pure oxygen batch to induce new effects on the neurons. Samples etched with conditions CHF_3:C3 and CF_4:C3 were considered too rough, exhibiting similar topographies to the previous batch, and were thus discarded. Nevertheless, they serve as a demonstration of how the etch process and resulting topographies are tunable and strongly dependent on plasma gas composition and concentration, showing topographies less rough than for equivalent etches with pure oxygen and rougher than equivalent etches with higher concentrations of the same fluorinated gas.

Gases	q_{gas} **[sccm]**	p **[mTorr]**	P_{bias} **[W]**	t **[s]**	S_a **[nm]**	**Name**	**Comment**
O_2	N/A	30	30	60	U	O_2:C1	Deemed too rough
		30	20	30	10.3	O_2:C2	SEM and AFM in fig. 4.6a
O_2 + CHF_3	10	20	200	300	U	CHF_3:C1	Etched through resist
	8	20	200	300	6.8	CHF_3:C2	SEM and AFM in fig. 4.6b
	5	20	300	300	U	CHF_3:C3	SEM in fig. 4.4d
O_2 + CF_4	5	20	300	180	U	CF_4:C1	Etched through resist
	5	20	300	120	1.3	CF_4:C2	SEM and AFM in fig. 4.6c
	3	20	300	120	U	CF_4:C3	SEM in fig. 4.4c
O_2 + SF_6	10	20	200	180	U	SF_6:C1	Deemed too planar

Table 4.1: Overview of etching parameters used to produce the surface-roughened SU-8 samples displayed in phase two. q_{gas} represents release rate of gas added in addition to oxygen, p chamber pressure, P_{bias} bias power, t etching time and S_a measured surface roughness. U means no AFM measurements were taken of samples etched with the given parameters.

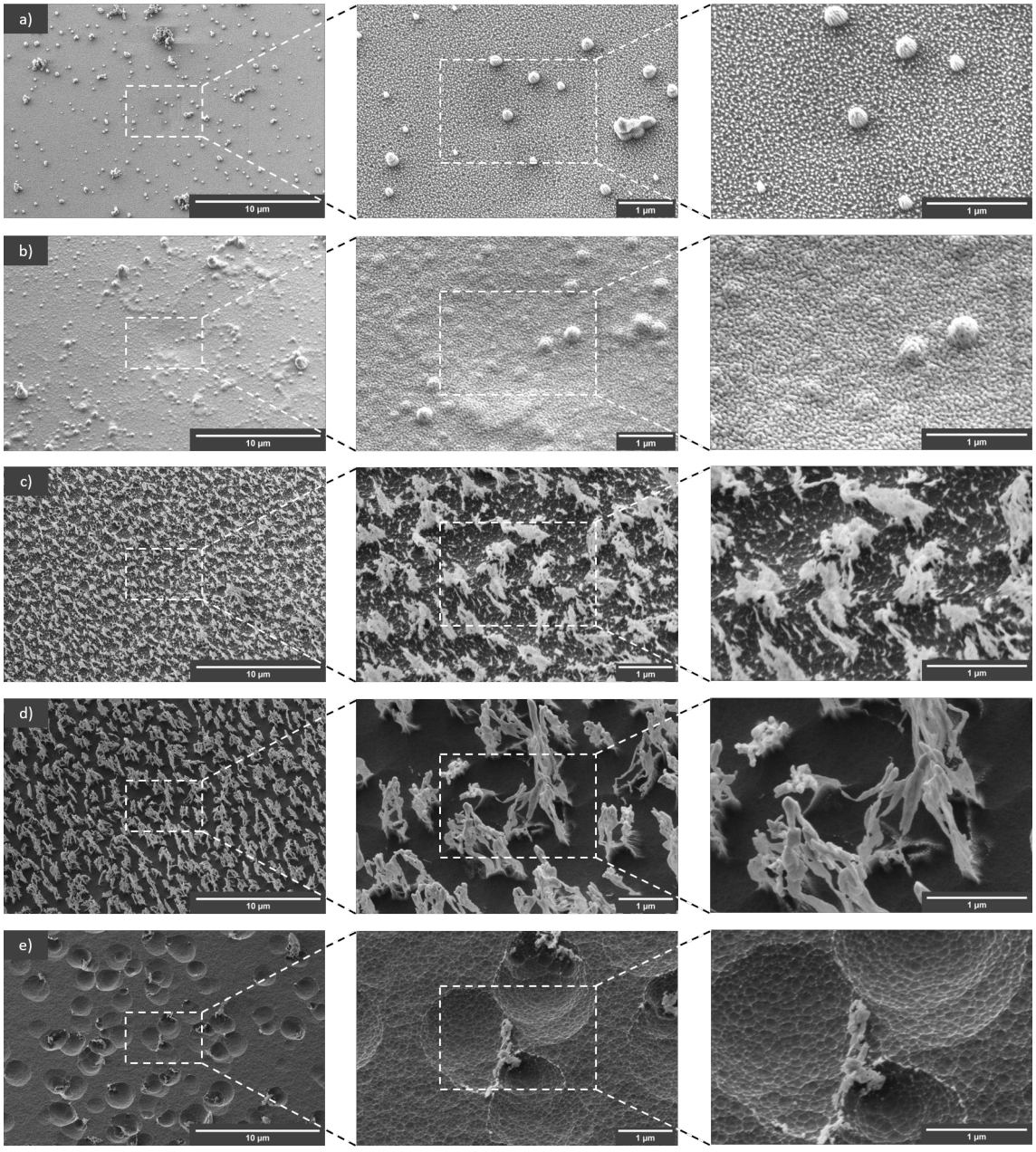

Figure 4.4: SEM micrographs of SU-8 film surfaces produced with various etch compositions, at 8 000x – 35 000x – 65 000x magnification. Samples were etched with conditions a) O_2:C2, b) CHF_3:C2, c) CF_4:C3, d) CHF_3:C3 and e) CF_4:C2.

Mentioned in section 4.2.1, poor neuron viability on planar SU-8 surfaces was hypothesized to result from low wettability. Therefore, the wettability of planar SU-8 surfaces, along with samples etched with the etch conditions selected for neuronal culturing, was measured by sessile drop contact angle measurements. Displayed in figure 4.5c, d and e, all roughened surfaces demonstrated strong hydrophilicity, with contact angles $\theta < 20°$ and in the case of samples in d and e too low for the analysis software to calculate. Non-treated planar SU-8, displayed in figure 4.5b, was found significantly less hydrophilic, with a contact angle of $\theta = 69.4°$. Although optimum surface wettability for biocompatibility with neurons is disputed, several works have concluded that contact angles of $\theta > 50 - 60°$ result in poor biocompatibility [128, 129]. Hence, the attribution of poor biocompatibility to the low surface wettability of non-etched SU-8 seemed warranted, and wettability would have to be increased for non-etched SU-8 to act as a viable control. A plasma cleaning treatment with 200 sccm O_2 at 40 kHz plasma generator frequency for 1 minute drastically reduced the contact angle of the same planar sample, to $\theta < 20°$, without significant effect on the surface topography, as displayed in figure 4.5f.

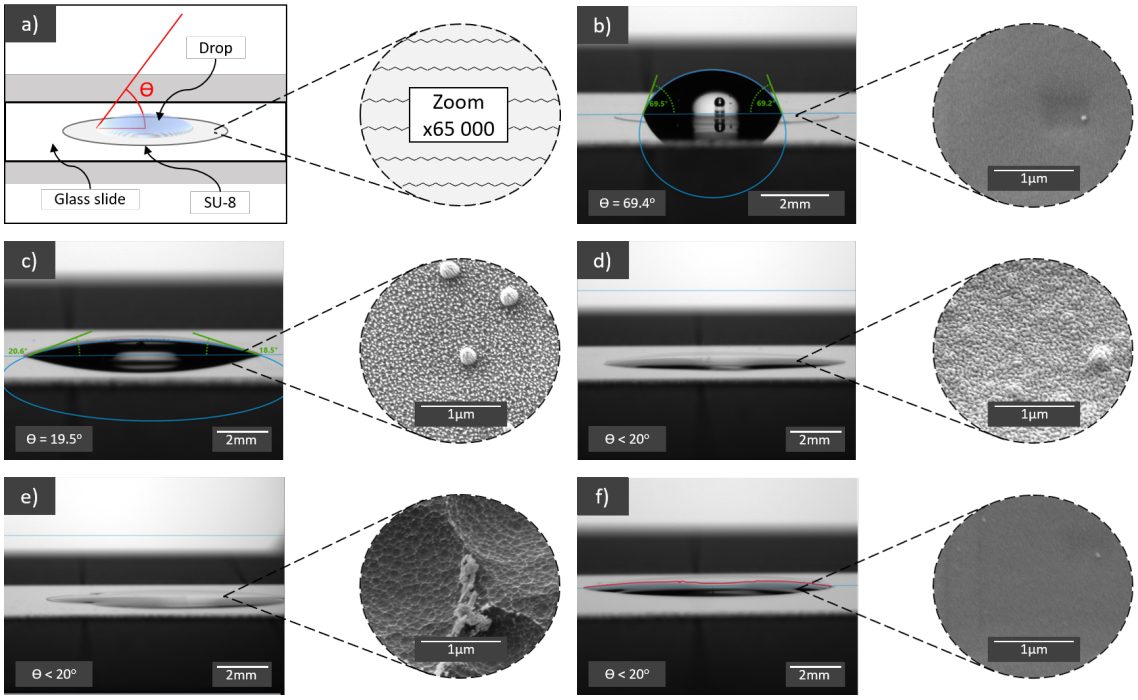

Figure 4.5: Sessile drop contact angle measurements of selected surfaces from the batch displayed in figure 4.4. Illustrated in a), each image displays the suspension of a drop of water on top of SU-8 films on glass slides, forming a contact angle θ based on the wettability of the surface. For each sample, a x65 000 magnification SEM micrograph of the sample surface is attached. c), d) and e) correspond to samples etches with conditions O_2:C2, CHF_3:C2 and CF_4:C2, respectively. b) is a planar non-etched SU-8 sample prior to plasma cleaning and f) the same sample after plasma cleaning.

Based on the selected three etch conditions, O_2:C2, CHF_3:C2 and CF_4:C2, a new neuronal culturing sample batch was fabricated with two chips for each parameter set, along with two planar samples treated with plasma cleaning acting as control. Displayed in figure 4.6a and b, topographies of samples etched with conditions O_2:C2 and CHF_3:C2 were found largely identical to the samples etched with the same parameters during high-throughput testing. Conversely, a notable discrepancy of surface features between samples etched with CF_4:C2 displayed in figure 4.6c and the sample with the same parameters in high-throughput testing was discovered. While nanoscale ridges and valleys were apparent in both, samples fabricated for neuronal culturing lacked the characteristic microscale craters found on the sample etched with the same parameter in high-throughput testing, displayed in figure 4.4e. Microscale craters were also not found on the surface of succeeding full-scale SU-8 covered MEA neural recording chips treated with the same etch condition, suggesting that the craters were an artefact of the high-throughput sample SU-8 film rather than a general feature of the roughening etch. Proposed as an explanation, microscale air bubbles regularly appear and reside in photoresist – resulting from trapping of air in the resist during transfer from the bottle to the sample or by shaking of photoresist bottles – and would upon bursting during etching leave open craters on the surface of the resist.

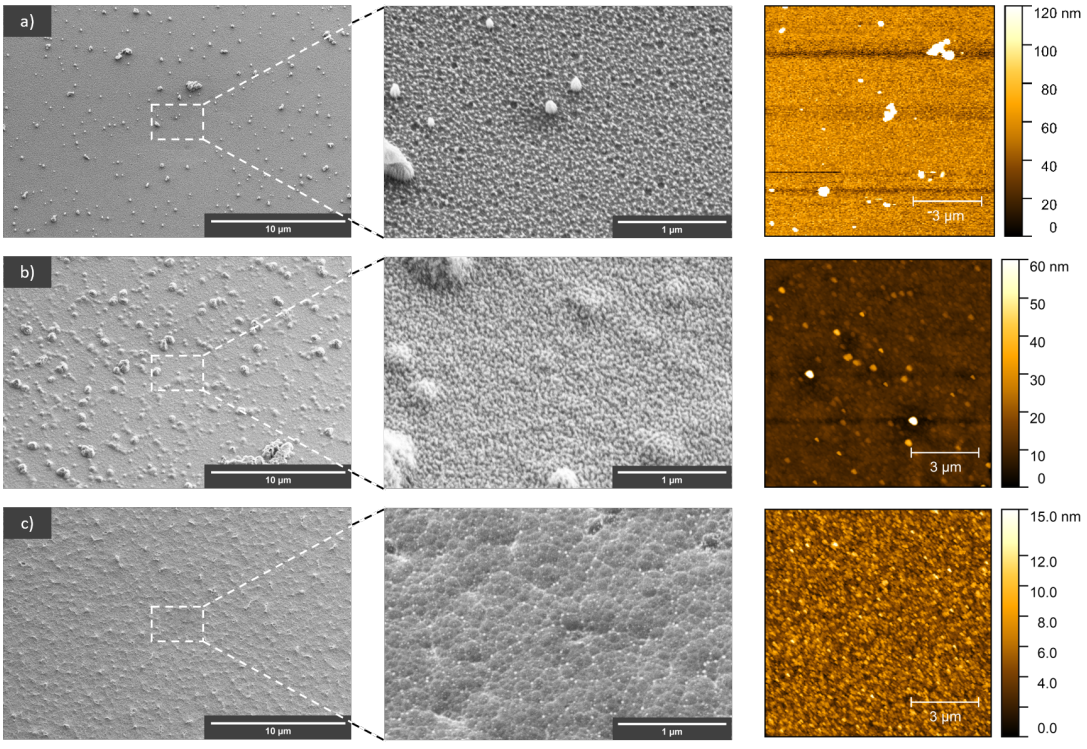

Figure 4.6: From left to right: SEM micrographs of SU-8 film surfaces at 8 000x magnification, further magnified to 65 000x and finally AFM measurements of the same surface. Samples were etched with the etch parameters deemed most promising from the batch displayed in figure 4.4. Etching conditions were a) O_2:C2, b) CHF_3:C2 and c) CF_4:C2.

Surfaces were measured with a single AFM measurement on one sample per parameter set. AFM measurements are presented in the right-most image column in figure 4.6, and equate to surface roughness $S_a = 10.6\,\text{nm}$ for the sample etched with conditions O_2:C2 and $S_a = 1.3\,\text{nm}$ for sample etched with CF_4:C2. The sample etched with conditions CHF_3:C2 was however measured in two locations on the sample. Upon optical inspection of the sample after etching, central areas of the SU-8 film appeared significantly more cloudy and white in color than peripheral areas of the film. Furthermore, the cloudy and white area corresponded perfectly to where the bottom of the glass substrate had been covered by fomblin oil for mounting on a carrier wafer. As mentioned in section 2.2.2, white appearance on plasma etched SU-8 film is a hallmark of the antimony induced roughening effect, suggesting central areas situated on the top of the glass directly above the fomblin oil brushed on the bottom were affected in a way that increased the roughening effect. For reference, an illustration of the procedure of mounting glass cover slides with fomblin oil to a 4" carrier wafer and the resulting roughening effect is illustrated in figure 4.7.

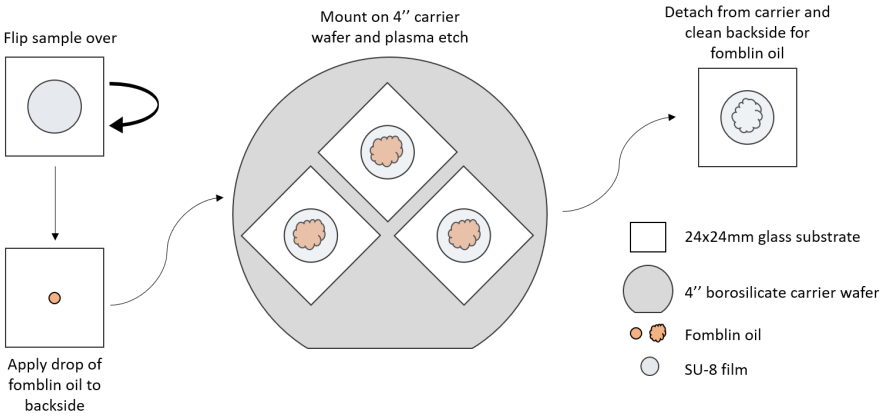

Figure 4.7: Illustration of the procesure for mounting 24x24 mm glass cover slides with SU-8 film to 4" carrier wafers for etching in the ICP-RIE machine. A drop of fomblin oil is rubbed on the back of the glass cover slide before mounting it on the carrier wafer, SU-8 film facing up and fomblin oil on the back affixing the glass substrate to the carrier wafer. After etching, detaching the substrate and cleaning remaining fomblin oil off the back of the glass, a white and cloudy patch is apparent on the SU-8 film corresponding perfectly to where the backside of the glass was covered by fomblin oil.

Confirmed by SEM micrographs and AFM measurements displayed in figure 4.8, central areas of the film were indeed an order of magnitude more rough than peripheral areas, with surface roughness $S_a = 53.4\,\text{nm}$ in the central area against $S_a = 6.8\,\text{nm}$ in the peripheral area. While not investigated by means of SEM and AFM, the same pattern – exceedingly white and cloudy areas of etched SU-8 film corresponding precisely to where fomblin oil had been brushed on the bottom of the glass – was found upon optical inspection of other samples etched with gas mixtures containing fluorinated gases. This was especially the case for gas mixtures containing CHF_3. Further interpretation and discussion of this result will be presented in section 5.3.

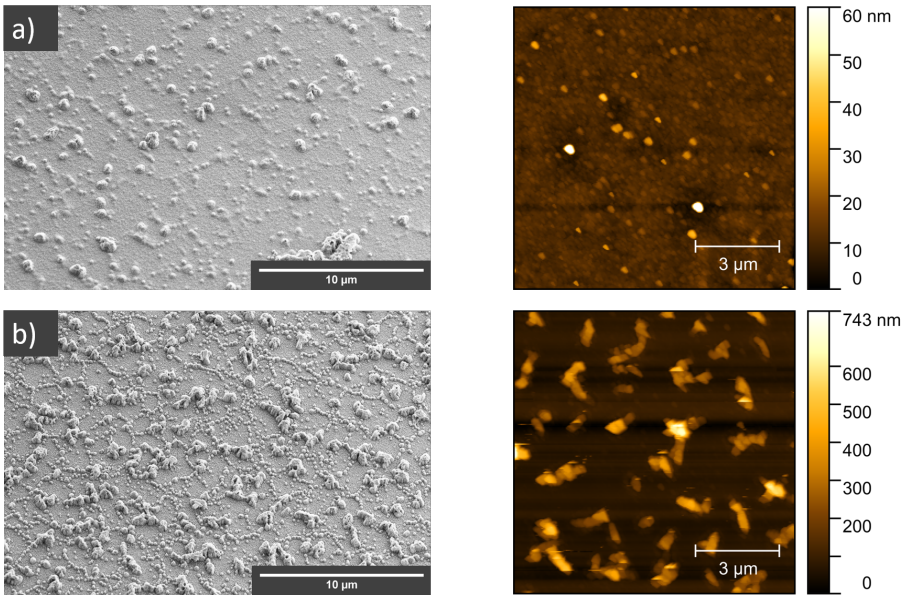

Figure 4.8: SEM micrographs at 8 000x magnification and AFM measurements from two areas of a single sample, etched with conditions CHF_3:C2. a) corresponds to a peripheral area of the SU-8 film, outside the region in which the bottom of the glass substrate was covered by fomblin oil during etching, while b) corresponds to a central area directly above the fomblin oil.

Contrary to the previous neuronal culturing sample set etched with extensive pure O_2 etches, a variety in induced neuronal response was observed on the new batch of samples etched with parameter sets O_2:C2, CHF_3:C2 and CF_4:C2. Microscopy images of randomly selected locations on samples taken after 14 DIV are presented in figure 4.9. After plasma cleaning treatment, planar SU-8 surfaces demonstrated excellent cell viability on par with glass control surfaces, pointing to low wettability of untreated planar SU-8 as the cause of poor cell viability in the previous culturing batch. Similar to more extensive pure O_2 etches, samples etched with conditions O_2:C2 – low bias power and short etch time with pure O_2 – were found to induce cell death, despite their significantly less porous and rough topography at roughness $S_a = 10.6\,\text{nm}$. Central regions of pronounced roughness, at $S_a = 53.4\,\text{nm}$, on the samples etched with CHF_3:C2 also induced cell death. Peripheral regions of significantly lower roughness, at $S_a = 6.8\,\text{nm}$, displayed good cell viability and signs of neuron clustering and axon fasciculation. Demonstrating the most promising network characteristics was however the networks grown on samples etched with conditions CF_4:C2, with the lowest roughness in the batch, at $S_a = 1.3\,\text{nm}$. Neurons grown these samples showed a clear increase in propensity for clustering and fasciculation of neurites compared to control chips of planar SU-8 and exposed glass regions around the roughened film. As outlined in section 2.1.4, fasciculation and clustering are both hallmarks of small-world topology and indications of a network topology more similar to that of the *in vivo* brain than networks without these features. Tendency of cultured neurons to cluster and fasciculate combined with uniformity in the surface topography and neuron response led to the selection of etching conditions CF_4:C2 for the incorporation of roughened

surfaces on the full neural network recording platform. Further analysis and results related to the neuronal culturing can be found in the thesis written by Hvide [18].

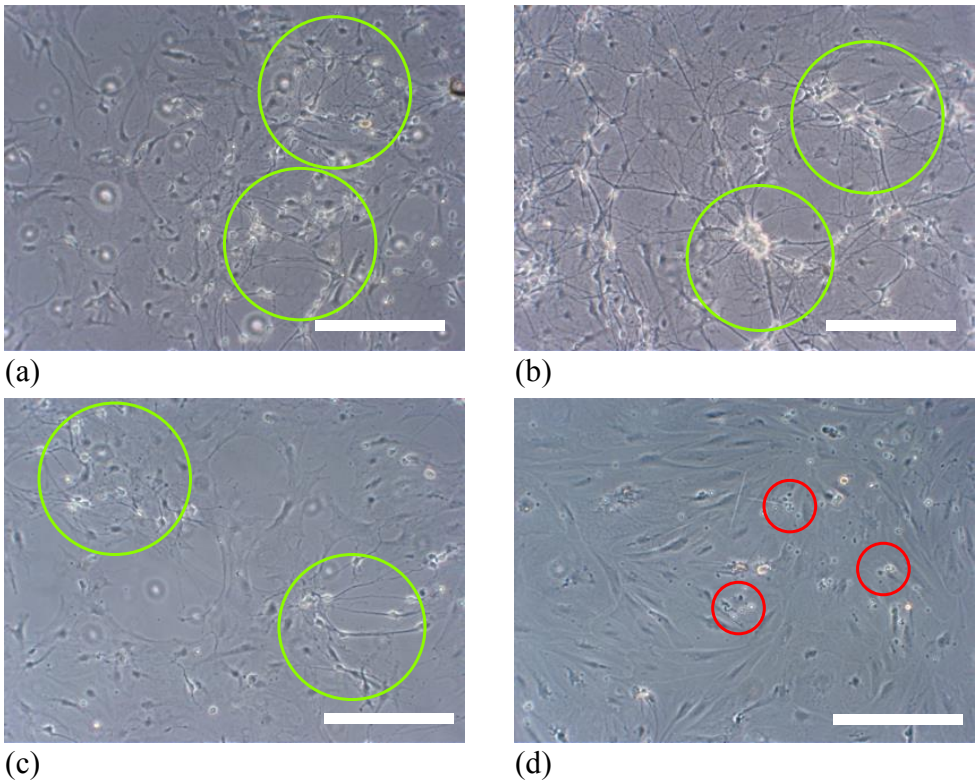

Figure 4.9: Representative images from regions of neural networks grown on roughened nanotopographical SU-8 and planar control surfaces. The regions of interest were selected at random, to avoid bias in analysis. Green circles in image of a) planar control highlight regions exemplifying tendencies of neuronal networks forming. In image of b) sample etched with condition CF_4:C2, the green circle highlights an area with large clusters and fasciculation of axons between cluters. In image of c) peripheral region of sample etched with CHF_3:C2, the green circle indicated area with networks forming, with a clearly lower density than in image b). In image of d) sample etched with O_2:C2, red circles show cells exhibiting a shrunken and non-polarized morphology, indicating cell death. All images have a scale bar of 150 μm. Images were acquired by phase contrast microscopy at 14 DIV, and were taken by Edevard Hvide.

4.3 Phase 3 — Incorporation on Neural Network Recording Platform

4.3.1 Fabrication

Photolithography protocols for SU-8 with improved adhesion had been established and RIE conditions for roughening of SU-8 to achieve topographies inducing behaviour reminiscent of that in the *in vivo* brain optimized. For the incorporation of rough SU-8

surfaces on the neural network recording platform, three primary fabrication concerns remained. Firstly, the observation that fomblin oil smeared on the bottom of glass slides affected the plasma etch process raised concerns about discrepancies in etch and roughening characteristics between the 170 µm thick glass cover slides mounted on carriers with fomblin oil and 1 mm thick 4" borosilicate wafers placed directly on the sample stage without mounting to a carrier. Both the second and the final concerns were centered around the replacement of Si_3N_4 – previously used as the insulating layer for electrodeposition and for irreversible bonding of PDMS to the surface on the neural network recording platform – with roughened SU-8. In order for SU-8 to be a viable direct replacement for Si_3N_4, it would have to provide sufficient insulation for electrodeposition and not adversely affect the resulting platinum black electrodes, and form a sufficiently strong seal upon reversible bonding of PDMS to prevent leakage or detachment during culturing.

As a first step towards determining the viability of incorporating roughened SU-8 on the neural network recording platform, the surface roughening process was tested on the 4" borosilicate substrate used for the platform. A wafer was covered with SU-8, etched with selected conditions, CF_4:C2, and characterised with SEM and AFM to determine whether resulting topographies deviated from those achieved on the thin 24x24 mm glass cover slides. SEM micrographs of the wafer surface, displayed in figure 4.10a, showed a topography clearly similar to those found on identically etched SU-8 on glass cover slides, displayed in figure 4.6c. Although the surface appeared somewhat less rough in SEM imaging, it was likely the result of the 4" wafer being imaged at 0° stage tilt while all surfaces on cut-out pieces of thin glass cover slips were imaged at 25° tilt. AFM measurements taken at three spots on the 4" wafer conversely revealed a higher roughness for the 4" wafer compared to the measurement on the glass cover slide, at $S_a = 4.1 \pm 0.4$ nm versus $S_a = 1.3$ nm respectively. Similar roughness values were later found for the two completed roughened surface neural network recording chips, at $S_a = 4.8 \pm 0.3$ nm on one and $S_a = 4.7 \pm 0.6$ nm on the other. AFM measurements of the chips are displayed in figure 4.10b and c.

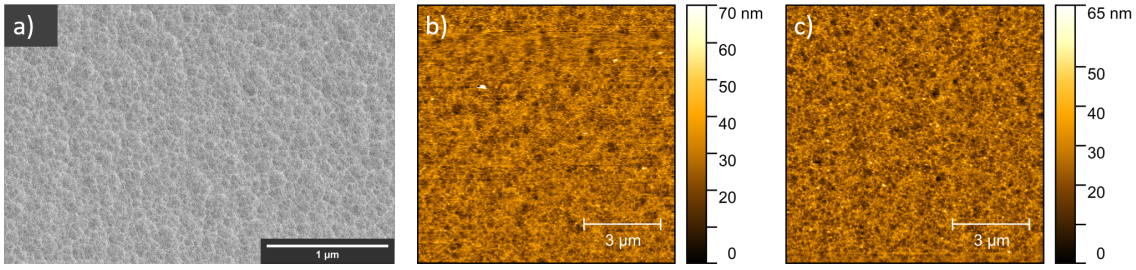

Figure 4.10: a) and b): AFM measurements of the two MEA neural recording chips with surface-roughened SU-8 films. c): 65 000x magnification SEM micrograph of the roughened SU-8 surface of a 4 inch wafer covered entirely by SU-8 and etched with the same parameters as the roughened MEA chips, condition CF_4:C2.

To determine whether PDMS could be reversibly bonded to roughened SU-8 and form a seal of sufficient strength to prevent detachment and leakage during neuronal culturing, another 4" wafer was prepared with SU-8 roughened with the selected parameters and bonded with PDMS. Neuronal culturing chambers and channels between

chambers were filled with water stained with blue food dye to make detection of leakage from the microfluidics simpler. After two weeks the microfluidic structure showed no signs of leakage or detachment, indicating a sufficiently strong seal between the PDMS and the roughened SU-8. During subsequent culturing of neurons, however, the PDMS on one of the neural network recording chips with roughened SU-8 detached completely after 8 DIV, out of a total of 4 neural network recording chips cultured with neurons.

Electrodeposition of platinum black with SU-8, roughened and planar, was the final aspect of fabrication of the neural network platform that needed to be explored. Addition of platinum black is strictly not necessary for comparatively large electrodes, such as the 50 µm ∅ electrodes fabricated in this project, as the signal to noise ratio for such electrodes is adequate even with simple planar electrode morphology. Nevertheless, electrode size is continuously decreased to improve specificity of recording – i.e. ability to record individual or small groups of neurons and distinguish them from others – and platinum black addition is required to keep the signal to noise ratio high. Thus, for roughened and planar SU-8 to be a viable option to replace Si_3N_4 in the long term, it should be compatible with platinum black deposition.

Platinum black electrodeposition was initially tested on chips with planar SU-8. Presented in figure 4.11, exposed electrodes positioned at the end of wires covered by insulating SU-8 appear white in color prior to deposition and change to the characteristic black color of platinum black after deposition. Growth of platinum black was not found to occur on any insulated wires, demonstrating excellent insulating capabilities for the SU-8 film. SEM micrographs of the platinum black electrodes grown on chips with planar SU-8, displayed in figure 4.12a, reveal a growth characterised by scattered highly porous "roses" of platinum black interspaced with relatively non-porous platinum. Maximizing effective surface area, highly porous platinum black should ideally cover the full electrode. Hence, while planar SU-8 was demonstrated to be compatible with platinum black electrodeposition, the process is certainly subject to optimization of parameters such as deposition driving potential and deposition time.

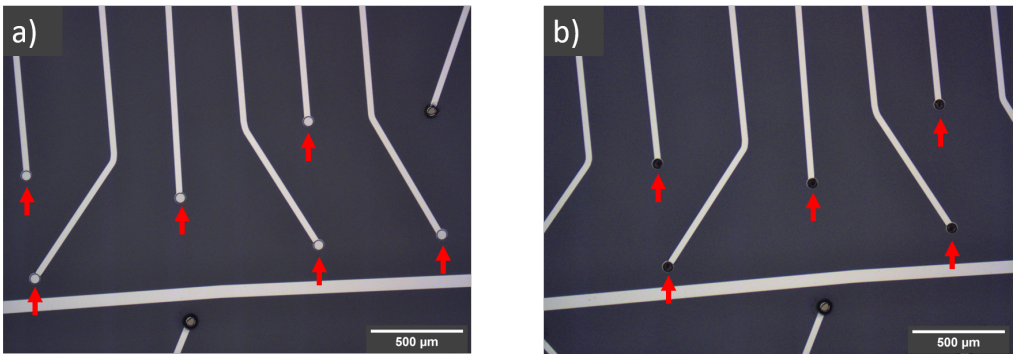

Figure 4.11: Optical microscopy images of wires and electrodes on a planar SU-8 MEA neural recording chip, a) before and b) after electrodeposition of platinum black. Sites of platinum black deposition are indicated with red arrows, prior to and after deposition. The color of the microelectrodes changes from the white color of the wires to a deep black color, confirming the growth of platinum black.

As can be seen in figure 4.12b, platinum black on chips with roughened SU-8 exhibited significantly more homogeneous porous growth across the entire electrode than that grown on chips with planar SU-8. On some electrodes grown on chips with roughened SU-8, however, a far more detrimental defect than sub-optimal platinum black morphology was observed. Demonstrated in the SEM micrographs in figure 4.13, flakes of platinum black were delaminating, and in certain cases completely detaching, from some of the electrodes. SEM micrographs taken of both the delaminating flake and the remaining electrode consist of platinum black. No apparent defects were found in the surrounding roughened SU-8 film, leading to the conclusion that the delamination of platinum black was caused by poor mechanical stability of the platinum black structure itself – as a result of non-ideal electrodeposition parameters – rather than defects on the sample prior to deposition. Due to concerns with delaminating and detaching platinum black adversely affecting neurons during culturing, a decision was made to fabricate two new MEA recording chips with planar platinum electrodes without deposition of platinum black.

An image of a completed neural network recording platform is displayed in figure 4.14.

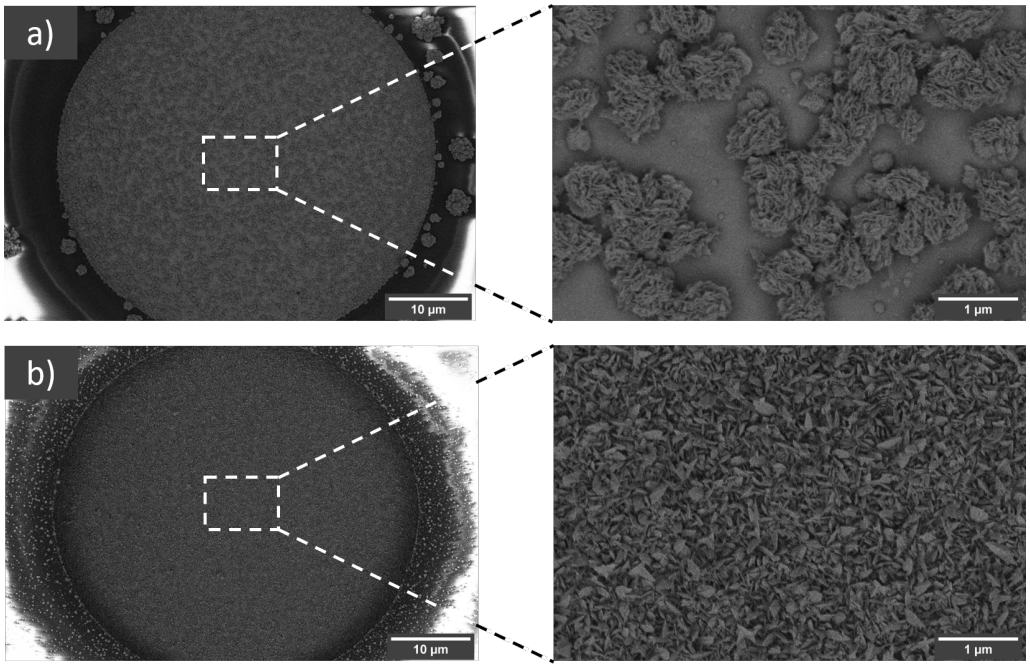

Figure 4.12: Overview and 35 000x magnification SEM micrographs of platinum black electrodes grown potentiostatically with the same driving potential of −0.3 V for samples with a) planar and b) roughened SU-8 as the insulating layer.

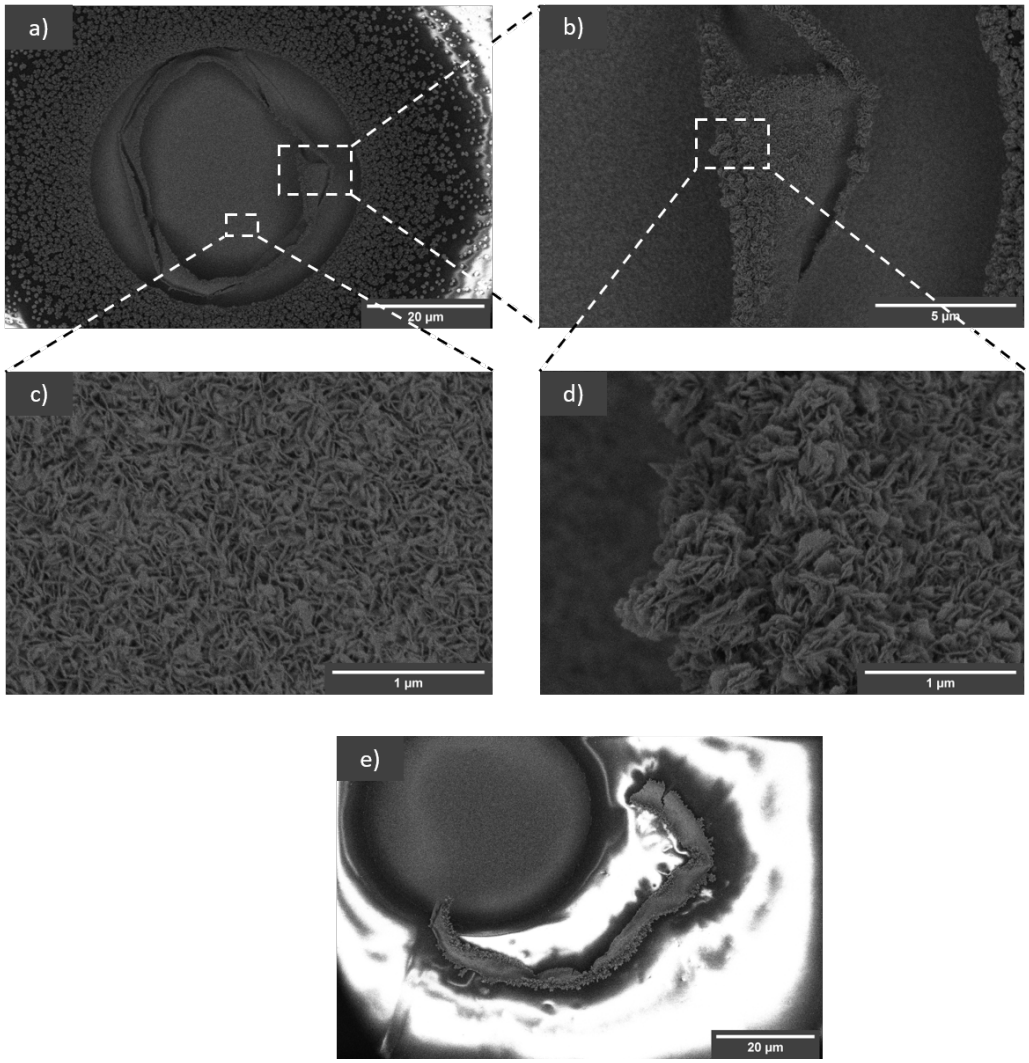

Figure 4.13: SEM micrographs showing delamination of platinum black occuring on electrodes for MEA chips with surface roughened SU-8. a) displays an overview of a delaminating platinum black electrode, b) a magnified view of the right side fold, c) 65 000x magnified view of the middle of the delaminating electrode and d) 65 000x magnified view of the edge of the right side delamination fold. e) displays an overview of a fully delaminated layer of platinum black having completely detached from the electrode and moved to the top of the SU-8 film.

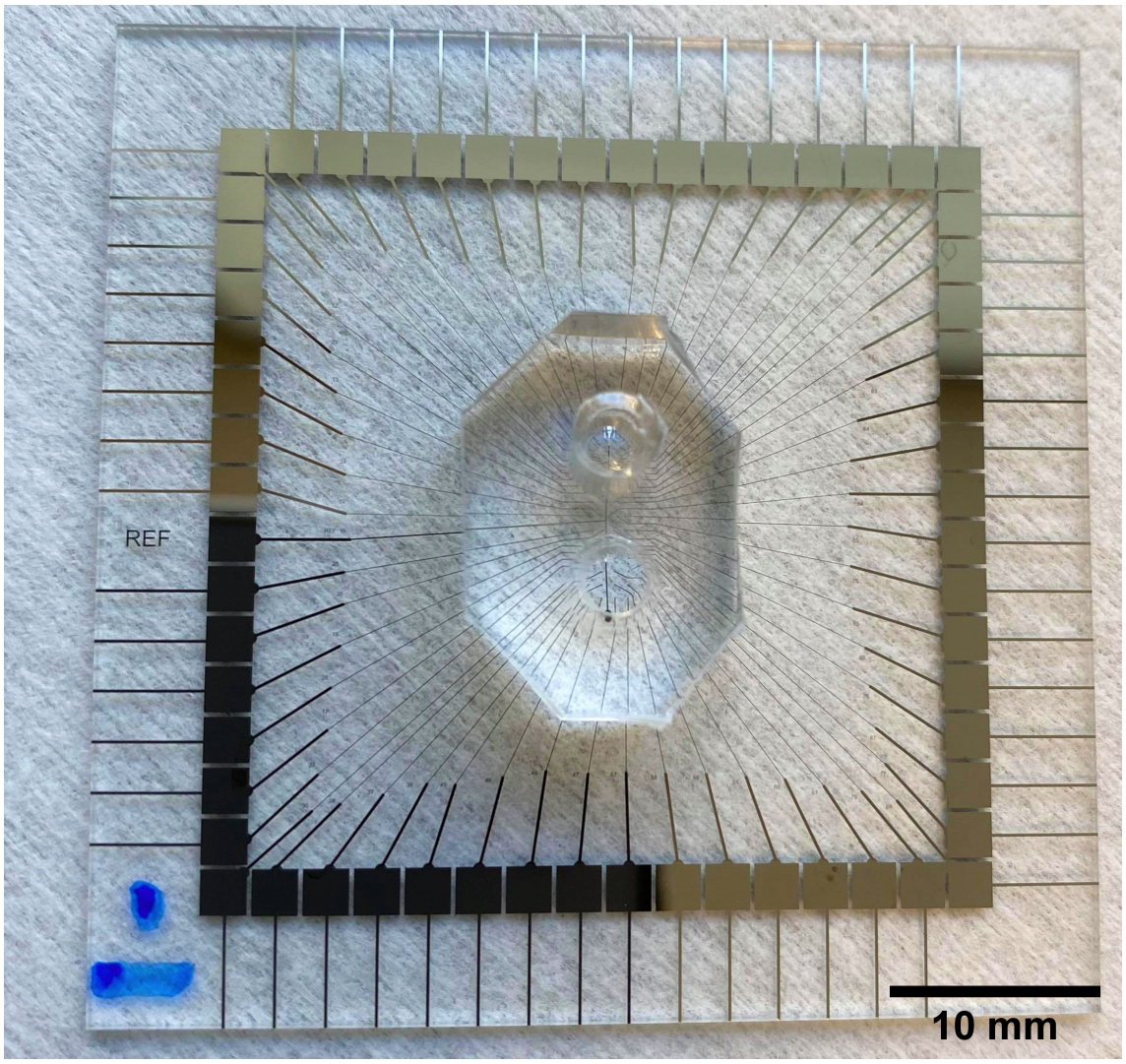

Figure 4.14: Birds-eye view of the complete neural recording chip, including the cut-out chip from the initial 4 inch glass wafer with MEAs and corresponding individual contact pads as well as the bonded PDMS microfluidic structure.

4.3.2 Recording Neurons on Nanotopographical Surfaces

Completed neural network recording platforms were successfully cultured with neurons and electrical activity of cultured networks was recorded through maturation. As mentioned, the PDMS microfluidic structure detached from one of the chips with roughened nanotopographical surface shortly after spontaneous network activity started emerging. Thus, significant network recording data was only acquired from a single nanotopographical surface chip and two planar surface control chip. It should therefore be stated that the statistical significance of the results that will be presented is poor. However, from the data that was acquired, observations were made that could indicate an increased degree of small world topology in the network grown on the nanotopographical surface. Some of the data acquired from electrophysiological recordings are displayed in figure 4.15.

Data on firing rate, displayed in figure 4.15a, serves as a validation of the health and stability of grown networks. Networks grown on both nanotopographic and planar surfaces exhibit a consistent increase in firing rate from the emergence of electrical spiking activity to the termination of the networks after 18 DIV. Resulting from the integration of progressively more signalling neurons in to the network, this increase is expected of healthy maturing networks [130].

Network bursts are characterised as periods of synchronized rapid firing in groups of neurons – such as neuron clusters, groups of clusters or the whole network – followed by periods of silence without activity [131]. As can be seen from figure 4.15b, the maturing network grown on the nanotopographical surface developed a higher rate of network bursts than networks grown on planar surfaces. This result arguably becomes more interesting when considered together with the data for the size of the frequent network bursts on nanotopography compared to those on planar surfaces. Demonstrated in figure 4.15c, network bursts in the network grown on the nanotopographic surface are of a significantly smaller scale than those in networks grown on planar surfaces. At the final point of recording, where networks had matured the longest, network bursts on average spanned 22.7 out of 59 actively recording electrodes on networks grown on nanotopography, and 36.7 out of 59 on planar surfaces. These results indicate more localized and frequent bursting behaviour in networks on nanotopographical surfaces, and less frequent and more globally spanning burst on planar surfaces. As outlined in section 2.1.4, highly synchronized global bursting activity is largely incompatible with the small-world topology principles of the *in vivo* brain neural networks. As such, these results, while not of particular statistical relevance due to low sample size, indeed imply a higher degree of small-worldedness in networks grown on nanotopography.

For further interpretation and discussion of results related to electrophysiological measurements, the reader is referred to the complimentary work of Hvide [18].

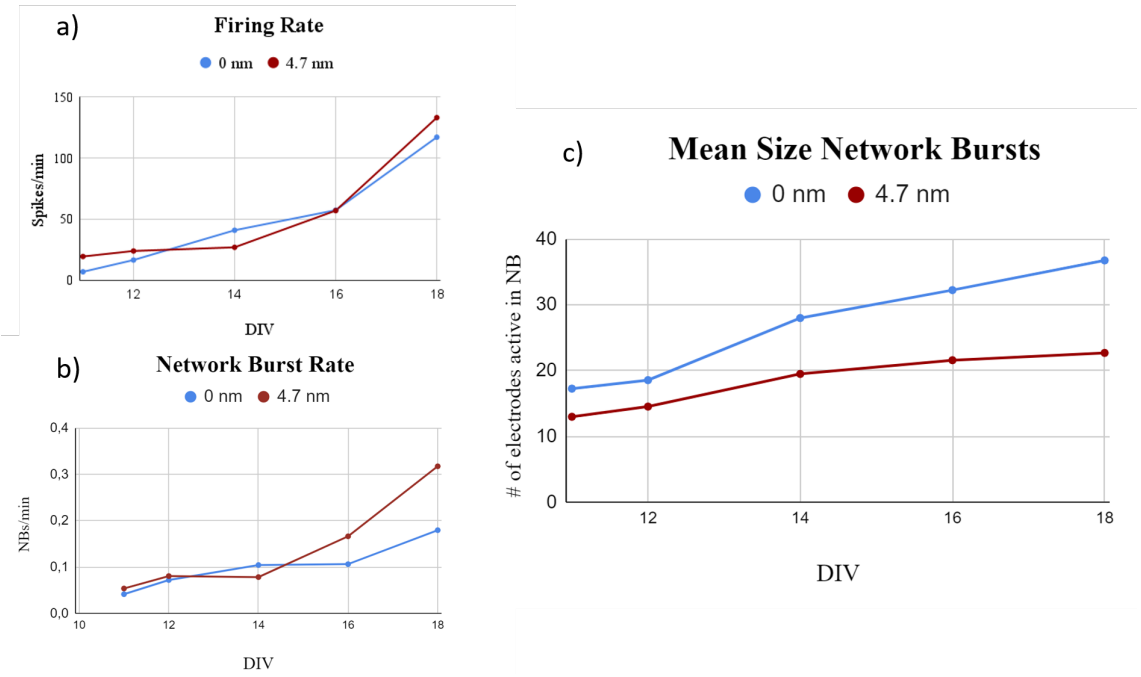

Figure 4.15: Data calculated from electrophysiological recordings performed at different points of maturation (DIV). Data relates to the single remaining chip with roughened SU-8 surface (red graphs, denotation 4.7 nm corresponding to its roughness) and the average from two planar SU-8 control chips (blue graphs, denoted 0 nm). Firing rate measured in spikes per minute given in a), network burst rate in bursts per minute given in b) and mean burst size given as average number of electrodes simultaneously active in a burst given in c). Electrophysiological measurements and subsequent calculation of statistical data was performed by Edevard Hvide.

Chapter 5

Discussion

Outline

In the following chapter, the impacts of the work performed in this thesis will be discussed on a general level, along with more elaborate discussion around some of the specific results presented in chapter 4. At the focal point of this project, a discussion will first be held on the development of the novel 2.5D network recording platform that was developed. Impact and prospects of the platform will be discussed, along with limitations and fabrication challenges. Discussion about the novel platform will be followed by a discussion on the observed effects of nanotopographical roughened SU-8 surfaces on neural networks cultured on the surfaces. Once again, the reader is referred to the complimentary thesis of Hvide for description of neural cell work and more thorough analysis of the effect of surfaces on neurons [18]. Finally the discussion will be steered towards observations, results and limitations from the fabrication processes not directly related to the developed neural network recording platform, as well as characterisation techniques.

5.1 Development of 2.5D *in vitro* Neural Network Recording Platform

5.1.1 Progress Towards Aim

Throughout the course of this project, the aim was to develop a 2.5D – termed 2.5D, between a 2D planar surface and more extensive 3D structure – nanotopographical neural network recording platform. Development of the platform would involve the establishment of new fabrication processes to replace the previously used planar Si_3N_4 base substrate with nanotopographically surface structured SU-8 photoresist. Incorporation of nanotopographies on the platform was aimed at mimicking the physical environment of the *in vivo* brain, and by extension replicate the physical guidance cues that contribute heavily to the formation of small-world network architecture. As mentioned in section 2.1.4, neurodegenerative diseases have been demonstrated to spread more quickly in networks with the small-world architecture of the nervous system than in other network topologies [50, 51]. Hence, inducing small-world network architecture similar to the brain would signify an improved efficacy of the *in vitro* platform in modeling the dynamics of neurodegenerative diseases in the *in vivo* brain.

With these initial aims and objectives in mind, three important results achieved in the course of this project should be highlighted.

- Biocompatible SU-8 nanotopographic surfaces were successfully implemented on the neural network recording platform. Nanotopographically structured SU-8 films were proved to be a viable direct replacement for planar Si_3N_4. Herein, nanotopographic SU-8 was found compatible with bonding of PDMS microfluidics, achieving sealing capable of withstanding 18 days in neuronal culture medium, and as insulation for electrodeposition of platinum black and during electrophysiological recording. This was achieved without than addition of new components, other than the nanotopographic SU-8 in itself, or large chip design changes to support the replacement. Thus, while this project specifically carried out implementation on a two-chamber 59 electrode neural network recording platform, the SU-8 nanotopographic surfaces should be implementable on existing platforms of any microfluidic design and with any number of electrodes.
- Nanotopographic surfaces of SU-8 fabricated with roughening by etching conditions CF_4:C2 (table 4.1 in section 4.2.2) were found to result in neural networks exhibiting an increase of structural and functional characteristics correlated with small-world architecture. While further investigation, with larger sample sizes, is needed before conclusions can be drawn, these results indicate an ability of nanotopographical SU-8 surfaces to improve small-world topology in *in vitro* neural networks.
- Through tuning of RIE process parameters – gas composition, gas release rate, chamber pressure, bias power and etch time – a breadth of SU-8 surface nanotopographies varying in morphology, scale and pitch was achieved. At one end, slender and porous "seaweed" structures of height up to 1.5 µm, pitch 1-2 µm and roughness $S_a = 152 \pm 8$ nm (figure 4.3c) were achieved for a 5 minute pure oxygen etch. At the other, ridges and grooves of few nanometers in width and height

and roughness $S_a = 1.3\,\text{nm}$ (figure 4.6c) were achieved with conditions CF_4:C2 (table 4.1). Results were found to be in congruence with theory presented in 2.2.2, with the roughening increasing with extent of etch – e.g. by increasing etch time while keeping other parameters constant – and decrease with increasing addition of fluorinated gases. As such, the established method for plasma based roughening of SU-8 demonstrates excellent flexibility in controlled tuning of nanotopographies, with clear potential for further optimization.

5.1.2 Comparison with Existing Platforms & Future Perspectives

As highlighted in the section above, one of the prominent advantages of the novel SU-8 based 2.5D nanotopographical neural network recording platform developed in this project is its flexibility for adaptation on previously planar 2D platforms. Nanotopographical SU-8 was demonstrated to be a viable direct replacement of the traditionally used planar Si_3N_4 insulation layer, compatible with bonding of PDMS microfluidics and as insulation during electrodeposition of platinum black and electrophysiological recording. Rather than complicating the fabrication process, the replacement of Si_3N_4 with nanotopographical SU-8 brings a reduction in fabrication process steps. Application of Si_3N_4 involves chemical vapor deposition of Si_3N_4 covering the whole substrate, followed by patterning of an etch mask with photolithography and finally etching to remove insulation on electrodes and contact pads [132, 133]. In comparison, the application of nanotopographical SU-8 merely involves photolithography and etching, alleviating the need for the chemical vapor deposition step. In summary, the SU-8 plasma etch based nanotopographical surface structuring developed and incorporated on a neural network platform in this project is a promising and simple way of incorporating physical environment on previously planar platforms.

No published works have been found to have incorporated 2.5D nanotopographical surfaces on a complete *in vitro* neural network recording platform – herein defined as a platform incorporating microfluidics and electrical recording with neural culturing. However, some 2.5D surface structuring strategies have been tested that could have potential on a neural network recording platform. In their work in 2014, Kang et al. cultured neurons on top of monolayers of silica beads placed on a planar substrate [134]. Bead monolayers were made of beads of uniform diameter in a regular lattice, with monolayers of different bead diameters tested in the range 600-1800 nm, and reportedly resulted in accelerated neurite growth – the circuitry of neural networks. No investigations in to the larger scale architecture of grown neural networks were made, but a hypothesis can be raised for accelerated circuit formation resulting in organization in to more complex networks, potentially of higher degree of small-worldedness. However, as presented in section 2.1.5, the sensing apparatus of neurons, components of the ECM and the structures mediating their interaction span across the low nanometer to low micrometer scale. Hence, it seems reasonable to assume that while uniformly sized beads in a regular lattice may capture some of the important physical guidance cues of the *in vivo* brain, it neglects others and thus likely would not induce the same small-worldedness as in the brain. Additionally, incorporation on neural network recording platforms would have to involve scaffolding surrounding the

microelectrodes and shielding them from the beads, so as not to damage the porous platinum black electrodes or interrupt recording.

Employing a different strategy, Baranes et al. in 2015 investigated behavior of neurons grown on top of an electrospun polymer fiber matrix with fibers of approximate diameter 270 nm decorated with gold nanoparticles of diameter 10 nm. Baranes et al. studied effects on neural stem cell differentiation rather than effects on network formation [135]. Nevertheless, the substrate intuitively seems like a promising candidate in recapturing the network growth guiding cues of the *in vivo* brain. The polymer fiber matrix closely reassembles the collagen fibril dimensions – 100-200 nm in diameter – and structure making up the major scaffolding compound of the ECM. Nanoparticles at low nanometer dimensions can reassemble the physical structure of various proteins decorating the collagen fibrils. In addition to the complication of fabrication that would be involved in electrospinning polymer fibers on neural network platforms and then decorating them with nanoparticles, making the structure compatible with the current microelectrodes embedding for recording would be challenging at best. Mentioned in section 2.1.2, the electrodes of embedded MEAs can record neural activity up to 100 µm away from the electrode, although signal strength and quality dissipates rapidly with distance. Isotropic electrospun polymer fibrous matricies can usually be achieved with a thickness of a few hundred micrometers, down to 50 µm [136]. Thus, a process would have to be established for fabricating an exceptionally thin mat of electrospun fibers for recording of neurons grown on top of the mat to be possible. Additionally, this would have to be achieved through millimeter openings in bonded microfluidic structure down to culture chambers, as bonding of sealed microfluidics on top of electrospun fibers would be impossible. In comparison to both of these methods, SU-8 based nanotopographical surfaces developed in this project have been proved far more compatible with current neural network recording platforms, and have demonstrated excellent flexibility in shaping into a myriad of different topographies.

Rather than recapitulating the nano- and low microscale components of the ECM and interaction with neurons, some work has been aimed at fabricating larger scaffolding for formation of 3D neural networks. 3D neural networks are herein defined as networks of neurons and circuitry distributing in layers in all three dimensions rather than as a monolayer on top of planar or topographic surfaces. In the work of Li et al. in 2018, a matrix of interlocked angled PDMS pillars of diameters approximately 5 µm and height 40 µm made with a photoresist mold created with three exposures [137]. Exposures were performed by tilting the sample 45° in relation to the light source and rotating it 120° around the its own axis between exposures. This 3D matrix was found to promote neuron distribution and circuit forming at different points along the height of the pillars, forming a 3D network. No analysis was however made with regards to the network characteristics of grown 3D networks in relation to 2D ones. In 2019, however, Valderhaug et al. grafted polymer particles of diameters between 100 and 1000 µm on a recording MEA chip from producer MultiChannel Systems to induce growth of 3D networks and test for characteristics of small-world topology [138]. Allowing neurons to form networks of three dimensions rather than two was found to increase prevalence of clustering and fasciculated axon "short-cuts" between clusters forming on top of separate polymer particles. Recording of activity of neurons

in the network situated up to 100 µm away from the electrodes at the base showed signs of less network-wide synchrony between populations in the 3D network than for 2D networks. In other words, similar changes in network architecture were indicated for these 3D networks as for the networks grown on the nanotopographical platform developed in this project.

In order to fully recapitulate the network architecture of the nervous system, a combination of larger scale 3D structuring approaches, such as those employed by Li et al. and Valderhaug et al., with nanotopographical structuring will likely have to be applied. 3D scaffolding enable neurons and circuitry to organize in three dimensions rather than two, as in the brain, while nanotopographies can capture the physical guiding cues steering development towards small-world architecture. One of the clear advantages of basing the nanotopographic neural network platform developed in this project on SU-8 is the versatility in structuring of SU-8 photoresist. SU-8 photoresist is widely regarded in research for its capability of producing high aspect ratio structures with height of hundreds of micrometers [139–141]. While high aspect ratio pillars and similar three dimensional structures protruding normal to the surface can readily be fabricated with traditional lithography methods, SU-8 has also been shaped in to more complex three dimensional structures using advanced lithography techniques such as gray-scale lithography and diffraction lithography [142, 143]. Larger 3D SU-8 structures could in turn be treated with the plasma based roughening process established in this work, introducing nanotopography in addition to the 3D scaffold. Thus, a future alteration of the established neural network recording platform could be to pattern part of the SU-8 film directly under the open culture chambers of the microfluidics into 3D scaffolds and subsequently imprint nanotopography by RIE. In doing so, the platform could benefit from both 3D network structure and nanoscale physical guidance cues, likely resulting in networks of higher small-worldedness and greater clinical relevance.

5.1.3 Challenges & Limitations

While incorporation of SU-8 nanotopographical surfaces on the neural network recording platform was largely successful, some aspects of the complete platform fabrication proved are subject to improvement.

As outlined in section 2.2.1, bonding of PDMS to SU-8 after functionalization by oxygen plasma treatment results in reversible bonding and sealing. The advantage of reversible bonding is the option to remove the microfluidic structure after maturation and recording of neural networks to facilitate imaging with SEM. SEM imaging of physical network, neuron and neurite structure after recording of functional activity patterns could in turn help elucidate the bridge between structural and functional connectivity in neural networks. On the other hand, reversible bonding and sealing runs the risk of breaking and detaching during neural culturing, ruining ongoing experiments in cultures that take days to weeks to mature. Throughout the 18 DIV of culturing neurons on the neural network recording platform developed in this project, 1 out of 4 microfluidic structures detached, ruining one of the two platforms with nanotopographies. Hence, the current bonding procedure entails a trade-off between

reliable sealing and ability to detach PDMS for imaging. Considering the number of fabrication steps for a single platform and subsequent time spent maturating cultured neural networks, reliable sealing is arguably more desirable than the option to detach PDMS. With the aim of improving sealing, two strategies could be employed. Further optimization of steps involved in reversible sealing – such as oxygen plasma functionalization time or heating time and temperature during bonding – could potentially improve sealing capabilities, and reduce the ratio of detaching to stable bonds. Alternatively, the option to detach PDMS could be sacrificed in favor of reliable irreversible bonding and sealing. Several strategies have been demonstrated to achieve irreversible bonds between SU-8 and PDMS, including functionalization in nitrogen plasma rather than oxygen plasma [144, 145].

While electrodeposition of platinum black was demonstrated with nanotopographical SU-8 as insulation, some delamination of formed platinum black led to the decision of using planar platinum electrodes on the final chips to avoid potential adverse effects on neurons. As mentioned in section 2.2.1, as electrodes are progressively reduced in size to improve specificity in recording, application of porous platinum black is necessary to maintain signal quality. Consequently, reliable electrodeposition of platinum black must be achieved with nanotopographical SU-8 for it to be viable as a direct replacement for planar Si_3N_4 in future platforms. Deemed the most likely cause of delamination of platinum black deposited on electrodes of nanotopographical samples is the difference in film thickness compared to planar SU-8 (2.2 µm after etching from 10 µm versus 1 µm of planar film). Supply of reactant from bulk solution to reaction site in deeper electrode holes might be slower than for the more shallow holes in thinner films. Presented in section 2.2.1, the porous ramified structure of platinum black is a result of mass transport limitation, and thus reduced availability of reactant in the deeper electrode holes would accelerate the onset of mass transport limited growth and thus the porosity of resulting structures. Higher porosity entails lower mechanical stability, which has been a reported challenge in growth of platinum black structures [146]. Hence, reducing the film thickness of nanotopographic SU-8 by depositing a thinner original film before etching would be a first step in attempting to improve the reliability of use in electrodeposition of platinum black. An alternative theory is the nanotopographies having a destabilizing effect on platinum black. Counteracting this destabilizing effect, deposition voltage could be decreased, for example to −0.2 V, to produce less porous growth of higher mechanical stability. Less porous growth would however also signify a reduction in signal-to-noise ratio during recording. As a consequence, the viability of using nanotopographical SU-8 in deposition of platinum black on smaller electrodes, with higher demands on the surface area increase of porosity to maintain sufficient signal quality, could be compromised.

5.2 Neuronal Effects of Nanotopographical SU-8 Surfaces

In the course of this project, nanotopographical SU-8 fabricated with etching conditions CF_4:C2 (table 4.1) was demonstrated to induce more characteristics of small-world architecture than its planar counterpart. Both structural and functional patterns emerged that were more consistent with small-worldedness, as per theory presented in 2.1.4, than for planar surfaces. Structurally, it was found to promote clustering of neurons and fasciculation of axon bundles. Thus, it was found structurally coherent with the segregation into interconnected clusters connected by few but strong connections at hub nodes characteristic of small-world networks. Functional analysis by electrophysiological recording additionally revealed signs of reduced synchrony of activity on a larger network level, also consistent small-world architecture.

The nanotopograhies found to induce the most prominent small-world characteristics, and as a result were selected for incorporation on the complete neural network recording platform, were those resulting from etch conditions CF_4:C2. Based on AFM measurements, surface roughness S_a of the resulting nanotopographical surfaces was 1.3 nm for the tested 24x24 mm glass cover slip sample and 4-5 nm for full 4" samples. Similar structural network characteristics, that is propensity for clustering and fasciculation, was found on peripheral areas of samples etched with conditions CHF_3:C2, with surface roughness 6.8 nm. Conversely, all tested nanotopographies of higher roughness, above 10 nm, were found to induce cell death. These result were to some extent incoherent with previous findings, in terms of both optimal roughness for organization in to small-world networks and threshold levels of roughness for cell adhesion and viability.

In their work in 2017, Onesto et al. found small-worldedness of neural networks grown on rough surfaces of silicon to increase with increasing roughness for $S_a < 30$ nm [147]. In 2019, the same group reported small-worldedness in networks grown on surfaces of densely packed zinc oxide nanowires to be most prominent on surfaces of the lowest roughness tested, at S_a of approximately 35 nm [148]. It should however be noted that evaluation of small-worldedness in both cases was based not on electrophysiological recordings, nor on any analysis of formed circuitry, but purely on the spatial distribution of neurons in relation to each other. Small-worldedness was estimated using a statistical model called the waxman-model – described in the work of Edevard Hvide – on data for position of neuron somas, a model for which the validity is disputed [18]. Nevertheless, roughness threshold for cell viability was also found incongruent with previous findings. Brunetti et al. reported in their work in 2010 a roughness threshold on silicon surfaces of 80 nm, above which cell viability fell rapidly.

Two primary hypotheses are raised to explain these discrepancies in optimal and threshold values for surface roughness in comparison with previous works. Firstly, surface roughness measured by arithmetical mean deviation, S_a, is merely one metric, and cannot in itself perfectly capture the characteristics of a surface. As an example, a surface with densely packed small particles can have the same S_a as a surface with large, protruding, but scattered pillars. Displayed in AFM measurements and seen on SEM images in figures 4.3a and 4.6a, surfaces with measured roughness S_a of approx-

imately 26 and 10 nm, respectively, exhibited protruding structures of dimensions far higher than their roughness metric would indicate. For the surface achieved with pure oxygen plasma etch at 300 W bias power for 60 seconds, displayed in 4.3a, the base of the surface appeared nominally flat, but was scattered at intervals of hundreds of nanometers with large porous and protruding structures of height up to 400 nm. The surface achieved with etch conditions O_2:C2, displayed in figure 4.6a, is characterised by general densely packed dots of height below 50 nm, but also scattered with sudden protruding structures. The highest of these structures measured in the single AFM measurement was 120 nm, but SEM images clearly reveal some structures of height far above that. Thus, while roughness is below previously indicated threshold values for cell viability, both surfaces include features of dimensions far above their measured surface roughness and these threshold values. These abrupt and tall structures that fail to be captured by the surface roughness metric S_a could be the cause of poor cell viability and by extension prevent formation of complex networks.

An alternative theory revolves around the potential cytotoxic effect of antimony. As presented in section 2.2.2, the roughening mechanism of SU-8 in plasma etching is likely based on antimony deposits from the resist PAG surfacing and shielding underlying SU-8 from etching. The result would be surfaces of rough structure, and high surface concentration of antimony. In their work in 2013, Rasmussen et al. found, surface concentration of antimony on SU-8 to increase from 0.1% to 24.1% from before to after etching with pure oxygen at 30 W bias power and 20 mTorr pressure for 20 minutes, with all other parameters equal to those used in this project [149]. They further found surface concentrations to be lower after etches with less roughening effect, achieved by addition of SF_6 to the plasma gas mixture. Thus, degree of roughening appears, in congruence with theory, appears closely correlated with antimony surface concentration and vice versa. In their work in 2009, Bregoli et al. demonstrated a cytotoxic effect on hemapoetic progenitor cells of antimony nanoparticles, but they did not have any observed toxic effect on 7 other cell lines [150]. Neurons were not tested by Bregoli et al., but cytotoxic effects from antimony on surfaces of nanotopographic etch roughened SU-8 could potentially be the cause of low neuron viability. Furthermore, rougher surfaces would in this case lead to lower cell viability due to higher surface concentration of antimony. Unlike the cells in the experiments of Bregoli et al., neurons are however likely in limited direct contact with antimony, as surfaces are coated with laminin and PLO before neural culturing. Nevertheless, the potential of antimony affecting cell viability should be investigated.

5.3 Additional Finding: Fomblin Oil Affecting Etch Process

As presented and illustrated in section 4.2.2, fomblin oil used for mounting 24x24 mm glass slides with SU-8 film to a 4" carrier wafer during RIE was found to have a clear affect on certain etches. Under some etching conditions involving fluorinated gases – particularly etches with CHF_3 in the gas mixture – fomblin oil increased the extent of the roughening of areas situated above it. Based on the SU-8 etching theory

presented in section 2.2.2 suggesting fluorinated gases reduce roughening by forming compounds with antimony with lower boiling points, an hypothesis for the fomblin oil effect is offered.

Addition of fluorinated gases was proposed to reduce the etch roughening effect by introducing reactive fluorine ions forming SbF_3 and SbF_5 compounds with significantly lower boiling points (376 °C and 141 °C) than those of atomic antimony and Sb_2O_3 (1425 °C and 1587 °C). Thus, these antimony compounds more readily evaporate from the surface upon local heating at the surface of SU-8 produced by the etch process, reducing the amount and retention time of antimony on the SU-8 surface shielding underlying resist. Local heat accumulation at different parts of the SU-8 resist will however vary based on how well heat can be conducted away from the surface and through the substate to the sample stage. While no specific information on the conductivity of fomblin oil could be found, oils are significantly better conductors of heat than air. As such, areas of SU-8 film situated directly above fomblin oil will have a more direct path of heat conduction to the sample stage than areas under which air separates the sample from the sample stage. From these peripheral areas, heat will have to be conducted through a longer path of glass substrate before reaching fomblin oil or be conducted through comparatively insulating air. With less heat accumulating at areas of SU-8 directly above fomblin oil, less antimony compounds evaporate from the surface and the roughening effect is consequently less impaired. As an explanation for the more prominent effect on etches with addition of CHF_3 compared to CF_4, a lower atomic concentration of fluorine in CHF_3 (3 per molecule against 4 in CF_4) likely favors the formation of SbF_3 to a larger extant than SbF_5. With a higher boiling point than SbF_5, more heat would have to be locally accumulated to produce high vapor pressure of SbF_3 from the surface. Thus, the effect of less accumulated heat causing less evaporation of antimony over fomblin oil might be more apparent and larger differences in roughness come as a result.

This theory would also help explain the increased roughness of substrates etched with CF_4 on 4" inch glass wafers placed directly on the sample stage compared to glass slides mounted with fomblin oil. With direct contact between the glass substrate and the sample stage, and glass exhibiting significantly higher heat conductivity than oils, heat is conducted more readily away from the SU-8 surface. Consequently, less heat accumulates and the roughening effect of the plasma etch is less impaired by the fluorinated gas.

5.4 Limitations of Methods

5.4.1 Surface Roughness S_a as Surface Metric

Throughout the course of this project various nanotopographical surfaces were tested for their effect on neurons and their organization into networks. To compare different surfaces and link surface characteristics to neuronal effects, the surface roughness metric arithmetical mean deviation S_a was utilized. However, as pointed out in section 5.2, S_a is a rather ambiguous metric which on its own cannot fully describe a surface and its characteristics. Particularly, surfaces of discontinuous nature charac-

terised by abrupt and scattered features are poorly captured by the metric S_a. Without metrics capturing surface characteristics more definitely, it is difficult to establish a link between surface topography and elicited neuronal response.

In an effort to provide a more complete basis of comparison between surfaces, S_a should be supplied with other metrics of surface characteristics. *Root mean squared* S_q, defined as the arithmetic mean of the square of deviation, by virtue of calculating a squared value puts higher weight on larger deviations. *Fractal dimensions* D_f provides a metric for complexity of the roughness profile of a surface. Combined, these metrics would provide a more complete picture of nanotopographical surfaces, and form a better basis of comparison.

5.4.2 Sample Sizes

Due to the constraint of time, several of the experiments conducted throughout this project used small sample sizes, compromising the statistical significance of the findings. In measuring surfaces of the last culturing batch on 24x24 mm glass cover slides, displayed in figure 4.6, only a single AFM measurement was taken on a single sample per set of etching parameters. While a minimum of three measurements per set of etching parameters was planned, problems with the AFM equipment making engagement of the probing tip to the surface difficult and time consuming led to the decision to take one measurement per set instead. After the PDMS structure on one of two nanotopographical neural network recording platforms detached during culturing, only a single sample was left. With a single nanotopographical sample and two planar control samples, data on differences in activity patterns between neural networks cultured on nanotopographical and planar samples is of poor statistical significance.

In future works, larger sample sizes could make results more conclusive.

5.4.3 Photolithographic Exposure Time

Presented in section 4.1, the photolithography protocol established for exposure of 1 and 10 µm films of SU-8 in this project involved exposure in a maskless aligner with exposure dose 5000 mJ/cm^2. Due to SU-8 being far less sensitive to the 375 nm wavelength light from the laser in the maskless aligner, the exposure dose had to be increased drastically from the 150 mJ/cm^2 dose found sufficient with i-line exposure in the mask aligner. The result of the high exposure dose and exposure method in the maskless aligner, scanning over the sample and directly imprinting small parts of the design for a total of thousands of steps, was extensive exposure time. Exposing the SU-8 layer on a single chip for the neural network recording platform took approximately 6 hours. With i-line exposure and 150 mJ/cm^2 dose in the mask aligner, in which the entire design is exposed simultaneously through a mask, the same exposure would take approximately one minute. Small sample size and limited time to wait for delivery of a tailored mask from a producer led to the decision to carry out exposure in the maskless aligner. In future works, however, the purchase or fabrication of a mask and subsequent transition over to exposure in the mask aligner would be highly recommended to severely reduce fabrication time.

Chapter 6

Conclusion

In vitro neural network platforms hold tremendous potential for shining light on features of neural network function and, importantly, degeneration. However, a vital criterion for these platforms to be clinically significant is that they capture features of the *in vivo* neural networks important to the course of the degenerative diseases they seek to model. The nano- and microscale physical environment of the brain has been shown to steer formation of neural networks with architecture facilitating complex function, but also rapid disease spread. Traditional *in vitro* neural network platforms based on planar substrates neglect the importance of the *in vivo* physical environment, and result in network architecture of lesser clinical relevance. As such, this project set out to develop a nanotopographical surface *in vitro* neural network recording platform, in an effort to improve the resulting neural network characteristics and clinical relevance of the platform.

Firstly, a method for nanotopographical structuring of SU-8 surfaces was established, based on a plasma etch roughening process unique for SU-8. The established method demonstrated excellent flexibility in producing a breadth of nanotopographies, with scale and nature of nanotopographies changing reliably with tuning of etch parameters. Importantly, nanotopographical SU-8 was demonstrated to be a viable direct replacement for the traditionally used planar Si_3N_4 base substrate of neural network recording platforms. Accordingly, incorporation was proved possible on any neural network recording platform previously using Si_3N_4. Herein, nanotopographical SU-8 was found compatible with bonding of PDMS microfluidics and as insulation during electrodeposition of platinum black electrodes and neural recording. Additionally, nanotopographical SU-8 incorporated on the developed *in vitro* neural network recording platform was found to promote small-world characteristics in neural network. Cultured neurons were found to organize more persistently into clusters and form axon bundles, and resulting networks exhibited less global synchrony than on planar surfaces, implying higher degree of small-worldedness and, by extension, clinical relevance. Nevertheless, further optimization and investigation with larger sample sizes are needed before definitive conclusions about the improvement of network topology and clinical relevance can be drawn.

Chapter 7

Future Directions

As argued in section 5.1.2, an exciting direction to continue this work in could be incorporation of nanotopographies with larger three dimensional structures. With the utility of the photoresist SU-8, advanced photolithography techniques such as gray-scale and diffraction photolithography can be employed to create larger three dimensional patterns of SU-8. Nanotopography can in turn be imposed on these three dimensional structures by using the plasma etch roughening process established in this project. Combining larger three dimensional scaffolding, allowing neurons to organize into three dimensional networks, with nanotopography, providing additional physical guidance cues for network development, intuitively seems like a promising approach to recapitulate the network development effects of the *in vivo* ECM.

In addition to expanding the project in exciting new directions, focus should be put on further investigations and optimization of the developed platform to determine its utility. Proposed changes and additional work to the developed platform are listed below, in no particular order.

- Electrodeposition of platinum black and bonding of PDMS to nanotopographical SU-8, while clearly viable, are subject to optimization. Unstable growth causing delamination of some platinum black electrodes should be prevented to avoid adverse effects on neurons. Reducing film thickness and/or reducing deposition potential are proposed as approaches to make the growth more stable. Reversible bonding of PDMS should be optimized to improve the ratio of stable to unstable sealing, by optimization of bonding parameters such as oxygen plasma functionalization time and heating time and temperature during bonding. Alternatively, irreversible bonding, with stable sealing but lack of option for removal, could be achieved by techniques outlined in section 5.1.3.
- Analysis of surfaces should be expanded to calculation of more metrics than merely S_a to capture the complexities of the topography to a better extent. By calculating a set of metrics more clearly defining the surface topographies, a clearer link between surface characteristics and elicited neuronal response can be established. Among proposed additional metrics are root mean squared, S_q, and fractal dimensions, D_f.
- A wider selection of topographies should be tested with neurons to optimize effects on formed networks, along with larger sample sizes to achieve results of

higher statistical relevance.

- Exposure of SU-8 films should be changed from exposure with 375 nm wavelength light in a maskless aligner to i-line exposure in a mask aligner, using a fabricated or purchased mask with the design presented in section 3.2.1. In doing so, exposure time would be drastically reduced, from 6 hours to a mere minute, thus improving the efficiency of fabrication.
- The potential for neuron viability to be affected by antimony concentration on roughened SU-8 surfaces should be investigated.

Bibliography

[1] R. W. Williams and K. Herrup, 'The control of neuron number,' *Annual Review of Neuroscience*, vol. 11, no. 1, pp. 423–453, 1988.

[2] G. Ming and H. Song, 'Adult neurogenesis in the mammalian brain: Significant answers and significant questions.,' *Neuron.*, vol. 70, no. 4, pp. 687–702, 2011.

[3] P. D. Sohn, C. T.-L. Huang, R. Yan, L. Fan, T. E. Tracy, C. M. Camargo, K. M. Montgomery, T. Arhar, S.-A. Mok, R. Freilich, J. Baik, M. He, S. Gong, E. D. Roberson, C. M. Karch, J. E. Gestwicki, K. Xu, K. S. Kosik and L. Gan, 'Pathogenic tau impairs axon initial segment plasticity and excitability homeostasis,' *Neuron*, vol. 104, no. 3, pp. 458–470, 2019.

[4] M. J. Knight, B. McCann, R. A. Kauppinen and E. J. Coulthard, 'Magnetic resonance imaging to detect early molecular and cellular changes in alzheimer's disease,' *Frontiers in Aging Neuroscience*, vol. 8, p. 139, 2016.

[5] L. C. Walker and M. Jucker, 'The exceptional vulnerability of humans to alzheimer's disease,' *Trends in Molecular Medicine*, vol. 23, no. 6, pp. 534–545, 2017.

[6] M. Denham and M. Dottori, 'Neural differentiation of induced pluripotent stem cells,' in *Neurodegeneration: Methods and Protocols*, G. Manfredi and H. Kawamata, Eds. 2011, pp. 99–110.

[7] A. Kundu, L. Micholt, S. Friedrich, D. R. Rand, C. Bartic, D. Braeken and A. Levchenko, 'Superimposed topographic and chemical cues synergistically guide neurite outgrowth,' *Lab on a Chip*, vol. 13, no. 15, p. 3070, 2013.

[8] E. Ergir, B. Bachmann, H. Redl, G. Forte and P. Ertl, 'Small force, big impact: Next generation organ-on-a-chip systems incorporating biomechanical cues,' *Frontiers in Physiology*, vol. 9, Oct. 2018.

[9] H. Amin, T. Nieus and D. Lonardoni, 'High-resolution bioelectrical imaging of ab-induced network dysfunction on cmos-meas for neurotoxicity and rescue studies,' *Sci Rep*, vol. 7, p. 2460, 2017.

[10] S. J. Hearne and J. A. Floro, 'Microphysiological human brain and neural systems-on-a-chip: Potential alternatives to small animal models and emerging platforms for drug discovery and personalized medicine,' *Stem Cell Rev Rep*, vol. 13, no. 3, pp. 381–406, 2017.

[11] D. Pamies, T. Hartung and H. Hogberg, 'Biological and medical applications of a brain-on-a-chip,' *Exp Biol Med*, vol. 239, no. 9, pp. 1096–1107, 2014.

[12] O. SPORNS, D. CHIALVO, M. KAISER and C. HILGETAG, 'Organization, development and function of complex brain networks,' *Trends in Cognitive Sciences*, vol. 8, no. 9, pp. 418–425, Sep. 2004.

[13] R. Ayala, T. Shu and L.-H. Tsai, 'Trekking across the brain: The journey of neuronal migration,' *Cell*, vol. 128, no. 1, pp. 29–43, Jan. 2007.

[14] A. Gladkov, Y. Pigareva, D. Kutyina, V. Kolpakov, A. Bukatin, I. Mukhina, V. Kazantsev and A. Pimashkin, 'Design of cultured neuron networks in vitro with predefined connectivity using asymmetric microfluidic channels,' *Scientific Reports*, vol. 7, no. 1, Nov. 2017.

[15] P. Massobrio, J. Tessadori, M. Chiappalone and M. Ghirardi, 'In VitroStudies of neuronal networks and synaptic plasticity in invertebrates and in mammals using multielectrode arrays,' *Neural Plasticity*, vol. 2015, pp. 1–18, 2015.

[16] M. Marcus, K. Baranes, M. Park, I. S. Choi, K. Kang and O. Shefi, 'Interactions of neurons with physical environments,' *Advanced Healthcare Materials*, vol. 6, no. 15, p. 1 700 267, Jun. 2017.

[17] P. Ringer, G. Colo, R. Fässler and C. Grashoff, 'Sensing the mechano-chemical properties of the extracellular matrix,' *Matrix Biology*, vol. 64, pp. 6–16, 2017.

[18] E. Hvide, 'Effects of su-8 nanotopography on neuronal cells and neural networks in novel *In Vitro* platform,' M.S. thesis, Norwegian University of Science & Technology, Jun. 2021.

[19] F. Azevedo, L. Carvalho, L. Grinberg, J. Farfel, R. Ferretti, R. Leite, W. Jacob Filho, R. Lent and S. Herculano-Houzel, 'Equal numbers of neuronal and nonneuronal cells make the human brain an isometrically scaled-up primate brain,' *J Comp Neurol.*, vol. 513, no. 5, pp. 532–541, 2009.

[20] J. Purkinje, 'Uber neuesten untersuchungen aus der nerven- und hirn-anatomie,' 1838, Bericht über die Versammlung deutscher Naturforscher und Ärzte im September 1837 (pp. 177 - 180).

[21] H. Zeng and J. Sanes, 'Neuronal cell-type classification: Challenges, opportunities and the path forward,' *Nat Rev Neurosci*, vol. 18, pp. 530–546, 2017.

[22] E. Kandel, J. H. Schwartz and T. Jessel, *Principles of Neural Science*, 5th. Elsevier, 2012.

[23] D. Pfaff and N. Volkow, *Neuroscience in the 21st Century*, 2nd. Springer, 2013.

[24] E. Kandel, J. H. Schwartz and T. Jessel, *Principles of Neural Science*, 5th. Elsevier, 2012.

[25] O. Sporns, G. Tononi and R. Kötter, 'The human connectome: A structural description of the human brain,' *PLOS Computational Biology*, vol. 1, no. 4, pp. 245–251, 2005.

[26] E. Vizi, J. P. Kiss and B. Lendvai, 'Nonsynaptic communication in the central nervous system,' *Neurochemistry International*, vol. 45, no. 4, pp. 443–451, 2004.

[27] C. Su, K. Menuz and J. Reisert, 'Non-synaptic inhibition between grouped neurons in an olfactory circuit,' *Nature*, vol. 492, pp. 66–71, 2012.

[28] B. Alberts, A. Johnson and J. e. a. Lewis, 'Molecular biology of the cell,' in, 4th ed. New York: Garland Science, 2002, ch. Ion Channels and the Electrical Properties of Membranes.

[29] A. Hodgkin, 'Ionic movements and electrical activity in giant nerve fibres,' *Proc. R. Soc. Lond. B Biol. Sci.*, vol. 148, pp. 1–37, 1958.

[30] D. Ren, 'Sodium leak channels in neuronal excitability and rhythmic behaviors,' *Cell*, vol. 72, no. 6, pp. 899–911, 2011.

[31] M. E. J. Obien, K. Deligkaris, T. Bullmann, D. J. Bakkum and U. Frey, 'Revealing neuronal function through microelectrode array recordings,' *Frontiers in Neuroscience*, vol. 8, p. 423, 2015.

[32] H. G. Rey, C. Pedreira and R. Quian Quiroga, 'Past, present and future of spike sorting techniques,' *Brain Research Bulletin*, vol. 119, pp. 106–117, 2015.

[33] E. Kandel, J. H. Schwartz and T. Jessel, 'Principles of neural science,' in, 5th. Elsevier, 2012, ch. 10.

[34] B. Scholl and N. J. Priebe, 'The cortical connection,' *Nature*, vol. 518, no. 7539, pp. 306–307, Feb. 2015.

[35] A. L. Kolodkin and M. Tessier-Lavigne, 'Mechanisms and molecules of neuronal wiring: A primer,' *Cold Spring Harbor Perspectives in Biology*, vol. 3, no. 6, a001727–a001727, Dec. 2010.

[36] L. Strochlic, C. Weinl, M. Piper and C. Holt, 'Axon pathfinding,' in *Evolution of Nervous Systems*, Elsevier, 2007, pp. 187–209.

[37] L. K. Low and H.-J. Cheng, 'Axon pruning: An essential step underlying the developmental plasticity of neuronal connections,' *Philosophical Transactions of the Royal Society B: Biological Sciences*, vol. 361, no. 1473, pp. 1531–1544, Jul. 2006.

[38] S. N. Burke and C. A. Barnes, 'Neural plasticity in the ageing brain,' *Nature Reviews Neuroscience*, vol. 7, no. 1, pp. 30–40, Jan. 2006.

[39] D. S. Bassett, D. L. Greenfield, A. Meyer-Lindenberg, D. R. Weinberger, S. W. Moore and E. T. Bullmore, 'Efficient physical embedding of topologically complex information processing networks in brains and computer circuits,' *PLoS Computational Biology*, vol. 6, no. 4, K. J. Friston, Ed., e1000748, Apr. 2010.

[40] R. E. Passingham, K. E. Stephan and R. Kötter, 'The anatomical basis of functional localization in the cortex,' *Nature Reviews Neuroscience*, vol. 3, no. 8, pp. 606–616, Aug. 2002.

[41] D. Hebb, 'The organization of behavior: A neuropsychological theory,' 1949.

[42] D. S. Bassett and O. Sporns, 'Network neuroscience,' *Nature Neuroscience*, vol. 20, no. 3, pp. 353–364, Feb. 2017.

[43] S. M. Zeki, 'Functional specialisation in the visual cortex of the rhesus monkey,' *Nature*, vol. 274, no. 5670, pp. 423–428, Aug. 1978.

[44] O. Sporns and J. D. Zwi, 'The small world of the cerebral cortex,' *Neuroinformatics*, vol. 2, no. 2, pp. 145–162, 2004.

[45] O. Sporns, 'Theoretical neuroanatomy: Relating anatomical and functional connectivity in graphs and cortical connection matrices,' *Cerebral Cortex*, vol. 10, no. 2, pp. 127–141, Feb. 2000.

[46] J. H. Downes, M. W. Hammond, D. Xydas, M. C. Spencer, V. M. Becerra, K. Warwick, B. J. Whalley and S. J. Nasuto, 'Emergence of a small-world functional network in cultured neurons,' *PLoS Computational Biology*, vol. 8, no. 5, O. Sporns, Ed., e1002522, May 2012.

[47] K. Heiney, O. H. Ramstad, V. Fiskum, N. Christiansen, A. Sandvig, S. Nichele and I. Sandvig, 'Criticality, connectivity, and neural disorder: A multifaceted approach to neural computation,' *Frontiers in Computational Neuroscience*, vol. 15, Feb. 2021.

[48] V. D. Valderhaug, W. R. Glomm, E. M. Sandru, M. Yasuda, A. Sandvig and I. Sandvig, 'Formation of neural networks with structural and functional features consistent with small-world network topology on surface-grafted polymer particles,' *Royal Society Open Science*, vol. 6, no. 10, p. 191 086, Oct. 2019.

[49] M. Frega, M. Tedesco, P. Massobrio, M. Pesce and S. Martinoia, 'Network dynamics of 3d engineered neuronal cultures: A new experimental model for in-vitro electrophysiology,' *Scientific Reports*, vol. 4, no. 1, Jun. 2014.

[50] B. Deleglise, S. Magnifico, E. Duplus, P. Vaur, V. Soubeyre, M. Belle, M. Vignes, J.-L. Viovy, E. Jacotot, J.-M. Peyrin and B. Brugg, 'Beta-amyloid induces a dying-back process and remote trans-synaptic alterations in a microfluidic-based reconstructed neuronal network,' *Acta Neuropathologica Communications*, vol. 2, no. 1, Sep. 2014.

[51] A. Fornito, A. Zalesky and M. Breakspear, 'The connectomics of brain disorders,' *Nature Reviews Neuroscience*, vol. 16, no. 3, pp. 159–172, Feb. 2015.

[52] M. E. Hatten, 'Riding the glial monorail: A common mechanism for glialguided neuronal migration in different regions of the developing mammalian brain,' *Trends in Neurosciences*, vol. 13, no. 5, pp. 179–184, May 1990.

[53] Y. Takei, J. Teng, A. Harada and N. Hirokawa, 'Defects in axonal elongation and neuronal migration in mice with disrupted tau and map1b genes,' *Journal of Cell Biology*, vol. 150, no. 5, pp. 989–1000, Sep. 2000.

[54] E. A. Vitriol and J. Q. Zheng, 'Growth cone travel in space and time: The cellular ensemble of cytoskeleton, adhesion, and membrane,' *Neuron*, vol. 73, no. 6, pp. 1068–1081, Mar. 2012.

[55] R. Zaidel-Bar, S. Itzkovitz, A. Ma'ayan, R. Iyengar and B. Geiger, 'Functional atlas of the integrin adhesome,' *Nature Cell Biology*, vol. 9, no. 8, pp. 858–867, Aug. 2007.

[56] E. Atilgan, D. Wirtz and S. X. Sun, 'Mechanics and dynamics of actin-driven thin membrane protrusions,' *Biophysical Journal*, vol. 90, no. 1, pp. 65–76, Jan. 2006.

[57] G. Jacquemet, H. Hamidi and J. Ivaska, 'Filopodia in cell adhesion, 3d migration and cancer cell invasion,' *Current Opinion in Cell Biology*, vol. 36, pp. 23–31, Oct. 2015.

[58] N. O. Alieva, A. K. Efremov, S. Hu, D. Oh, Z. Chen, M. Natarajan, H. T. Ong, A. Jégou, G. Romet-Lemonne, J. T. Groves, M. P. Sheetz, J. Yan and A. D. Bershadsky, 'Myosin IIA and formin dependent mechanosensitivity of filopodia adhesion,' *Nature Communications*, vol. 10, no. 1, Aug. 2019.

[59] J. P. Myers and T. M. Gomez, 'Focal adhesion kinase promotes integrin adhesion dynamics necessary for chemotropic turning of nerve growth cones,' *Journal of Neuroscience*, vol. 31, no. 38, pp. 13 585–13 595, Sep. 2011.

[60] T. Kawauchi, 'Regulation of cell adhesion and migration in cortical neurons,' *Small GTPases*, vol. 2, no. 1, pp. 36–40, Jan. 2011.

[61] J. Albuschies and V. Vogel, 'The role of filopodia in the recognition of nanotopographies,' *Scientific Reports*, vol. 3, no. 1, Apr. 2013.

[62] T. Mitchison and L. Cramer, 'Actin-based cell motility and cell locomotion,' *Cell*, vol. 84, no. 3, pp. 371–379, Feb. 1996.

[63] T. Ushiki, 'The three-dimensional ultrastructure of the collagen fibers, reticular fibers and elastic fibers: A review,' *Kaibogaku zasshi. Journal of anatomy*, vol. 67, no. 3, pp. 186–199, Jun. 1992.

[64] V. Brunetti, G. Maiorano, L. Rizzello, B. Sorce, S. Sabella, R. Cingolani and P. P. Pompa, 'Neurons sense nanoscale roughness with nanometer sensitivity,' *Proceedings of the National Academy of Sciences*, vol. 107, no. 14, pp. 6264–6269, Mar. 2010.

[65] U. Horzum, B. Ozdil and D. Pesen-Okvur, 'Step-by-step quantitative analysis of focal adhesions,' *MethodsX*, vol. 1, pp. 56–59, 2014.

[66] L. Yao, S. Wang, W. Cui, R. Sherlock, C. O'Connell, G. Damodaran, A. Gorman, A. Windebank and A. Pandit, 'Effect of functionalized micropatterned PLGA on guided neurite growth,' *Acta Biomaterialia*, vol. 5, no. 2, pp. 580–588, Feb. 2009.

[67] C. Miller, S. Jeftinija and S. Mallapragada, 'Synergistic effects of physical and chemical guidance cues on neurite alignment and outgrowth on biodegradable polymer substrates,' *Tissue Engineering*, vol. 8, no. 3, pp. 367–378, Jul. 2002.

[68] J. S. Chua, C.-P. Chng, A. A. K. Moe, J. Y. Tann, E. L. Goh, K.-H. Chiam and E. K. Yim, 'Extending neurites sense the depth of the underlying topography during neuronal differentiation and contact guidance,' *Biomaterials*, vol. 35, no. 27, pp. 7750–7761, Sep. 2014.

[69] O. Shefi, Alon, Miroshnikov, Perkas, A. Gedanken and I. Nissan, 'Substrates coated with silver nanoparticles as a neuronal regenerative material,' *International Journal of Nanomedicine*, p. 23, May 2014.

[70] F. Haq, V. Anandan, C. Keith and G. Zhang, 'Neurite development in PC12 cells cultured on nanopillars and nanopores with sizes comparable with fi lopodia,' *International Journal of Nanomedicine*, vol. 2, no. 1, pp. 107–115, Mar. 2007.

[71] C. A. Mack, *Principles of Optical Lithography: The Science of Microfabrication*. John Wiley & Sons, 2007.

[72] S. Franssila, *Introduction to Microfabrication*. John Wiley & Sons, Ltd, Sep. 2010.

[73] M. J. Madou, *Fundamentals of Microfabrication*. CRC Press, Oct. 2018.

[74] W. Moreau, 'Semiconductor lithography,' in. Springer, Boston, MA., 1988, ch. Prebake (Softbake).

[75] M. Walsh, F. Zhang, R. Menon and H. Smith, '6 - maskless photolithography,' in *Nanolithography*, M. Feldman, Ed., Woodhead Publishing, 2014, pp. 179–193.

[76] B. Broyde, 'Exposure of photoresists,' *Journal of The Electrochemical Society*, vol. 117, no. 12, p. 1555, 1970.

[77] R. M. Thankachan and R. Balakrishnan, 'Chapter 8 - synthesis strategies of single-phase and composite multiferroic nanostructures,' in *Synthesis of Inorganic Nanomaterials*, ser. Micro and Nano Technologies, Woodhead Publishing, 2018, pp. 185–211.

[78] G. Cao and Y. Wang, 'Nanostructures and nanomaterials,' in, 2nd ed. World Scientific, 2011, vol. 2, ch. 5.4 - Physical Vapor Deposition (PVD), pp. 240–248.

[79] T. Kerdcharoen and C. Wongchoosuk, '11 - carbon nanotube and metal oxide hybrid materials for gas sensing,' in *Semiconductor Gas Sensors*, Woodhead Publishing, 2013, pp. 386–407.

[80] B. G. Streetman and S. K. Banerjee, 'Chapter 5.1 - fabrication of p-n junctions,' in *Solid State Electronics*, Pearson Education Limited, 2016, pp. 179–194.

[81] D. Qin, Y. Xia and G. Whitesides, 'Soft lithography for micro- and nanoscale patterning,' *Nat Protoc*, vol. 5, pp. 491–502, 2010.

[82] T. Fujii, 'Pdms-based microfluidic devices for biomedical applications,' *Microelectronic Engineering*, vol. 61-62, pp. 907–914, 2002.

[83] A. Mata, A. J. Fleischman and S. Roy, 'Characterization of polydimethylsiloxane (pdms) properties for biomedical micro/nanosystems,' *Biomed. Microdevices*, vol. 7, pp. 281–293, 2005.

[84] H. Hillborg, J. Ankner, U. Gedde, G. Smith, H. Yasuda and K. Wikström, 'Crosslinked polydimethylsiloxane exposed to oxygen plasma studied by neutron reflectometry and other surface specific techniques,' *Polymer*, vol. 41, no. 18, pp. 6851–6863, 2000.

[85] Z. Zhang, P. Zhao, G. Xiao, B. R. Watts and C. Xu, 'Sealing SU-8 microfluidic channels using PDMS,' *Biomicrofluidics*, vol. 5, no. 4, p. 046 503, Dec. 2011.

[86] S. Talaei, O. Frey, P. van der Wal, N. de Rooij and M. Koudelka-Hep, 'Hybrid microfluidic cartridge formed by irreversible bonding of SU-8 and PDMS for multi-layer flow applications,' *Procedia Chemistry*, vol. 1, no. 1, pp. 381–384, Sep. 2009.

[87] Z. Zhu, P. Chen, K. Liu and C. Escobedo, 'A versatile bonding method for PDMS and SU-8 and its application towards a multifunctional microfluidic device,' *Micromachines*, vol. 7, no. 12, p. 230, Dec. 2016.

[88] K.-Y. Song, H. Zhang, W.-J. Zhang and A. Teixeira, 'Enhancement of the surface free energy of PDMS for reversible and leakage-free bonding of PDMS–PS microfluidic cell-culture systems,' *Microfluidics and Nanofluidics*, vol. 22, no. 11, Nov. 2018.

[89] M. Paunovic and M. Schlesinger, *Fundamentals of Electrochemical Deposition*, 2nd ed. John Wiley & Sons, Ltd, 2006.

[90] M. Paunovic and M. Schlesinger, 'Kinetics and mechanism of electrodeposition,' in *Fundamentals of Electrochemical Deposition*. 2006, ch. 6, pp. 77–112.

[91] A. Cowley and B. Woodward, 'A healthy future: Platinum in medical applications,' *Platinum Metals Review*, vol. 55, pp. 98–107, Apr. 2011.

[92] A. M. Feltham and M. Spiro, 'Platinized platinum electrodes,' *Chemical Reviews*, vol. 71, no. 2, pp. 177–193, 1971.

[93] L. Zhou, Y. Cheng and M. Amrein, 'Fabrication by electrolytic deposition of platinum black electrocatalyst for oxidation of ammonia in alkaline solution,' *Journal of Power Sources*, vol. 177, no. 1, pp. 50–55, 2008.

[94] 'Nanostructured platinum grass enables superior impedance reduction for neural microelectrodes,' *Biomaterials*, vol. 67, pp. 346–353, 2015.

[95] V. Viswam, M. E. J. Obien, F. Franke, U. Frey and A. Hierlemann, 'Optimal electrode size for multi-scale extracellular-potential recording from neuronal assemblies,' *Frontiers in Neuroscience*, vol. 13, p. 385, 2019.

[96] L. A. Camuñas-Mesa and R. Q. Quiroga, 'A detailed and fast model of extracellular recordings,' *Neural Computation*, vol. 25, no. 5, pp. 1191–1212, 2013.

[97] S. Arcot Desai, J. Rolston, L. Guo and S. Potter, 'Improving impedance of implantable microwire multi-electrode arrays by ultrasonic electroplating of durable platinum black,' *Frontiers in Neuroengineering*, vol. 3, p. 5, 2010.

[98] L. Plyasova, I. Molina, A. Gavrilov, S. Cherepanova, O. Cherstiouk, N. Rudina, E. Savinova and G. Tsirlina, 'Electrodeposited platinum revisited: Tuning nanostructure via the deposition potential,' *Electrochimica Acta*, vol. 51, no. 21, pp. 4477–4488, 2006.

[99] H. Lorenz, M. Despont, N. Fahrni, N. LaBianca, P. Renaud and P. Vettiger, 'SU-8: A low-cost negative resist for MEMS,' *Journal of Micromechanics and Microengineering*, vol. 7, no. 3, pp. 121–124, Sep. 1997.

[100] X.-B. Wang, J. Sun, C.-M. Chen, X.-Q. Sun, F. Wang and D.-M. Zhang, 'Thermal uv treatment on su-8 polymer for integrated optics,' *Opt. Mater. Express*, vol. 4, no. 3, pp. 509–517, Mar. 2014.

[101] P. Abgrall, V. Conedera, H. Camon, A.-M. Gue and N.-T. Nguyen, 'SU-8 as a structural material for labs-on-chips and microelectromechanical systems,' *ELECTROPHORESIS*, vol. 28, no. 24, pp. 4539–4551, Dec. 2007.

[102] S. Keller, G. Blagoi, M. Lillemose, D. Haefliger and A. Boisen, 'Processing of thin SU-8 films,' *Journal of Micromechanics and Microengineering*, vol. 18, no. 12, p. 125 020, Nov. 2008.

[103] K. V. Nemani, K. L. Moodie, J. B. Brennick, A. Su and B. Gimi, 'In vitro and in vivo evaluation of SU-8 biocompatibility,' *Materials Science and Engineering: C*, vol. 33, no. 7, pp. 4453–4459, Oct. 2013.

[104] S.-W. Youn, A. Ueno, M. Takahashi and R. Maeda, 'Microstructuring of SU-8 photoresist by UV-assisted thermal imprinting with non-transparent mold,' *Microelectronic Engineering*, vol. 85, no. 9, pp. 1924–1931, Sep. 2008.

[105] R. L. Barber, M. K. Ghantasala, R. Divan, D. C. Mancini and E. C. Harvey, 'Study of stress and adhesion strength in SU-8 resist layers on silicon substrate with different seed layers,' *Journal of Micro/Nanolithography, MEMS, and MOEMS*, vol. 6, no. 3, pp. 1–9,

[106] A. Voigt, G. Ahrens, M. Heinrich, A. Thompson and G. Gruetzner, 'Improved adhesion of novolac and epoxy based resists by cationic organic materials on critical substrates for high volume patterning applications,' in *Advances in Patterning Materials and Processes XXXI*, vol. 9051, SPIE, 2014, pp. 382–390.

[107] P. M. Dentinger, W. Clift and S. H. Goods, 'Removal of su-8 photoresist for thick film applications,' *Microelectronic Engineering*, vol. 61-62, pp. 993–1000, 2002.

[108] G. Hong, A. Holmes and M. Heaton, 'SU8 resist plasma etching and its optimisation,' *Microsystem Technologies*, vol. 10, no. 5, pp. 357–359, Aug. 2004.

[109] N. Oruganti, M. Goedert and S.-J. J. Lee, 'Process variability in surface roughening of SU-8 by oxygen plasma,' *Microsystem Technologies*, vol. 19, no. 7, pp. 971–978, Nov. 2012.

[110] W. M. Haynes, D. R. Lide and T. J. Bruno, *CRC handbook of chemistry and physics : a ready-reference book of chemical and physical data*, 97th ed. New York, CRC Press, 2017, ch. 4.

[111] H. Mischke, G. Gruetzner and M. Shaw, 'Plasma etching of polymers like SU8 and BCB,' in *Micromachining and Microfabrication Process Technology VIII*, vol. 4979, SPIE, 2003, pp. 372–381.

[112] M. F. L. De Volder, R. Vansweevelt, P. Wagner, D. Reynaerts, C. Van Hoof and A. J. Hart, 'Hierarchical carbon nanowire microarchitectures made by plasma-assisted pyrolysis of photoresist,' *ACS Nano*, vol. 5, no. 8, pp. 6593–6600, 2011.

[113] M. Tosa, 'Surface profilometer,' in *Compendium of Surface and Interface Analysis*. Springer Singapore, 2018, pp. 679–682.

[114] B. Cappella and G. Dietler, 'Force-distance curves by atomic force microscopy,' *Surface Science Reports*, vol. 34, no. 1, pp. 1–104, 1999.

[115] F. J. Giessibl, 'Afm's path to atomic resolution,' *Materials Today*, vol. 8, no. 5, pp. 32–41, 2005.

[116] M. A. S. R. Saadi, B. Uluutku, C. H. Parvini and S. D. Solares, 'Soft sample deformation, damage and induced electromechanical property changes in contact- and tapping-mode atomic force microscopy,' *Surface Topography: Metrology and Properties*, vol. 8, no. 4, p. 045 004, Oct. 2020.

[117] I. Schmitz, M. Schreiner, G. Friedbacher and M. Grasserbauer, 'Tapping-mode AFM in comparison to contact-mode AFM as a tool for in situ investigations of surface reactions with reference to glass corrosion,' *Analytical Chemistry*, vol. 69, no. 6, pp. 1012–1018, Mar. 1997.

[118] H. Seiler, 'Secondary electron emission in the scanning electron microscope,' *Journal of Applied Physics*, vol. 54, no. 11, R1–R18, 1983.

[119] R. A. Shatas, J. F. Marshall and M. A. Pomerantz, 'Dependence of secondary electron emission upon angle of incidence of 1.3-mev primaries,' *Phys. Rev.*, vol. 102, pp. 682–686, 3 1956.

[120] L. De Bartolo, M. Rende, S. Morelli, G. Giusi, S. Salerno, A. Piscioneri, A. Gordano, A. Di Vito, M. Canonaco and E. Drioli, 'Influence of membrane surface properties on the growth of neuronal cells isolated from hippocampus,' *Journal of Membrane Science*, vol. 325, no. 1, pp. 139–149, 2008.

[121] M. Ferrari, F. Cirisano and M. C. Morán, 'Mammalian cell behavior on hydrophobic substrates: Influence of surface properties,' *Colloids and Interfaces*, vol. 3, no. 2, 2019.

[122] A. W. Adamson and A. P. Gast, *Physical Chemistry of Surfaces*, 6th. John Wiley and Sons, 1997, pp. 352–364.

[123] R. Hebbar, A. Isloor and A. Ismail, 'Chapter 12 - contact angle measurements,' in *Membrane Characterization*, Elsevier, 2017, pp. 219–255.

[124] *Introduction to bruker's scanasyst and peakforce tapping afm technology*, 133, Rev. A0, Bruker Nano Surfaces Division, Apr. 2011.

[125] *Su-8 2000 permanent epoxy negative photoresist*, Ver. 4, MicroChem, Sep. 2019.

[126] *Yes hmds vapor prime process application note*, Yield Engineering Systems, Jun. 2008.

[127] S. P. Khan, G. G. Auner and G. M. Newaz, 'Influence of nanoscale surface roughness on neural cell attachment on silicon,' *Nanomedicine: Nanotechnology, Biology and Medicine*, vol. 1, no. 2, pp. 125–129, Jun. 2005.

[128] K. Göbbels, T. Kuenzel, A. van Ooyen, W. Baumgartner, U. Schnakenberg and P. Bräunig, 'Neuronal cell growth on iridium oxide,' *Biomaterials*, vol. 31, no. 6, pp. 1055–1067, Feb. 2010.

[129] K. Webb, V. Hlady and P. A. Tresco, 'Relative importance of surface wettability and charged functional groups on NIH 3t3 fibroblast attachment, spreading, and cytoskeletal organization,' *Journal of Biomedical Materials Research*, vol. 41, no. 3, pp. 422–430, Sep. 1998.

[130] E. Biffi, G. Regalia, A. Menegon, G. Ferrigno and A. Pedrocchi, 'The influence of neuronal density and maturation on network activity of hippocampal cell cultures: A methodological study,' *PLoS ONE*, vol. 8, no. 12, G. F. Gilestro, Ed., e83899, Dec. 2013.

[131] T. Fardet, M. Ballandras, S. Bottani, S. Métens and P. Monceau, 'Understanding the generation of network bursts by adaptive oscillatory neurons,' *Frontiers in Neuroscience*, vol. 12, Feb. 2018.

[132] L. Berdondini, M. Chiappalone, P. van der Wal, K. Imfeld, N. de Rooij, M. Koudelka-Hep, M. Tedesco, S. Martinoia, J. van Pelt, G. L. Masson and A. Garenne, 'A microelectrode array (MEA) integrated with clustering structures for investigating in vitro neurodynamics in confined interconnected sub-populations of neurons,' *Sensors and Actuators B: Chemical*, vol. 114, no. 1, pp. 530–541, Mar. 2006.

[133] G. Gholmieh, W. Soussou, M. Han, A. Ahuja, M.-C. Hsiao, D. Song, A. R. Tanguay and T. W. Berger, 'Custom-designed high-density conformal planar multielectrode arrays for brain slice electrophysiology,' *Journal of Neuroscience Methods*, vol. 152, no. 1-2, pp. 116–129, Apr. 2006.

[134] K. Kang, S. Y. Yoon, S.-E. Choi, M.-H. Kim, M. Park, Y. Nam, J. S. Lee and I. S. Choi, 'Cytoskeletal actin dynamics are involved in pitch-dependent neurite outgrowth on bead monolayers,' *Angewandte Chemie International Edition*, vol. 53, no. 24, pp. 6075–6079, Mar. 2014.

[135] K. Baranes, M. Shevach, O. Shefi and T. Dvir, 'Gold nanoparticle-decorated scaffolds promote neuronal differentiation and maturation,' *Nano Letters*, vol. 16, no. 5, pp. 2916–2920, Dec. 2015.

[136] M. A. Calhoun, S. S. Chowdhury, M. T. Nelson, J. J. Lannutti, R. B. Dupaix and J. O. Winter, 'Effect of electrospun fiber mat thickness and support method on cell morphology,' *Nanomaterials*, vol. 9, no. 4, p. 644, Apr. 2019.

[137] S. Li, F. P. U. Severino, J. Ban, L. Wang, G. Pinato, V. Torre and Y. Chen, 'Improved neuron culture using scaffolds made of three-dimensional PDMS micro-lattices,' *Biomedical Materials*, vol. 13, no. 3, p. 034 105, Feb. 2018.

[138] V. D. Valderhaug, W. R. Glomm, E. M. Sandru, M. Yasuda, A. Sandvig and I. Sandvig, 'Formation of neural networks with structural and functional features consistent with small-world network topology on surface-grafted polymer particles,' *Royal Society Open Science*, vol. 6, no. 10, p. 191 086, Oct. 2019.

[139] J. J. K. Kim, H. A. Thuwaini and M. Almuslem, 'Photolithography of SU-8 microtowers for a 100-turn, 3-d toroidal microinductor,' *Micro and Nano Systems Letters*, vol. 6, no. 1, Dec. 2018.

[140] L. Amato, S. S. Keller, A. Heiskanen, M. Dimaki, J. Emnéus, A. Boisen and M. Tenje, 'Fabrication of high-aspect ratio SU-8 micropillar arrays,' *Microelectronic Engineering*, vol. 98, pp. 483–487, Oct. 2012.

[141] A. del Campo and C. Greiner, 'SU-8: A photoresist for high-aspect-ratio and 3d submicron lithography,' *Journal of Micromechanics and Microengineering*, vol. 17, no. 6, R81–R95, May 2007.

[142] J. M. Dykes, D. K. Poon, J. Wang, D. Sameoto, J. T. K. Tsui, C. Choo, G. H. Chapman, A. M. Parameswaren and B. L. Gray, 'Creation of embedded structures in SU-8,' in *Microfluidics, BioMEMS, and Medical Microsystems V*, Jan. 2007.

[143] X. Tan, T. Shi, J. Lin, B. Sun, Z. Tang and G. Liao, 'One-step mask-based diffraction lithography for the fabrication of 3d suspended structures,' *Nanoscale Research Letters*, vol. 13, no. 1, Dec. 2018.

[144] Z. Zhang, P. Zhao, G. Xiao, B. R. Watts and C. Xu, 'Sealing SU-8 microfluidic channels using PDMS,' *Biomicrofluidics*, vol. 5, no. 4, p. 046 503, Dec. 2011.

[145] Y. Ren, S.-H. Huang, S. Mosser, M. Heuschkel, A. Bertsch, P. Fraering, J.-J. Chen and P. Renaud, 'A simple and reliable PDMS and SU-8 irreversible bonding method and its application on a microfluidic-MEA device for neuroscience research,' *Micromachines*, vol. 6, no. 12, pp. 1923–1934, Dec. 2015.

[146] R. Kim and Y. Nam, 'Novel platinum black electroplating technique improving mechanical stability,' in *2013 35th Annual International Conference of the IEEE Engineering in Medicine and Biology Society (EMBC)*, Jul. 2013.

[147] V. Onesto, L. Cancedda, M. L. Coluccio, M. Nanni, M. Pesce, N. Malara, M. Cesarelli, E. D. Fabrizio, F. Amato and F. Gentile, 'Nano-topography enhances communication in neural cells networks,' *Scientific Reports*, vol. 7, no. 1, Aug. 2017.

[148] V. Onesto, M. Villani, R. Narducci, N. Malara, A. Imbrogno, M. Allione, N. Costa, N. Coppedè, A. Zappettini, C. V. Cannistraci, L. Cancedda, F. Amato, E. D. Fabrizio and F. Gentile, 'Cortical-like mini-columns of neuronal cells on zinc oxide nanowire surfaces,' *Scientific Reports*, vol. 9, no. 1, Mar. 2019.

[149] K. H. Rasmussen, S. S. Keller, F. Jensen, A. M. Jorgensen and O. Hansen, 'Su-8 etching in inductively coupled oxygen plasma,' *Microelectronic Engineering*, vol. 112, pp. 35–40, 2013.

[150] L. Bregoli, F. Chiarini, A. Gambarelli, G. Sighinolfi, A. M. Gatti, P. Santi, A. M. Martelli and L. Cocco, 'Toxicity of antimony trioxide nanoparticles on human hematopoietic progenitor cells and comparison to cell lines,' *Toxicology*, vol. 262, no. 2, pp. 121–129, Aug. 2009.

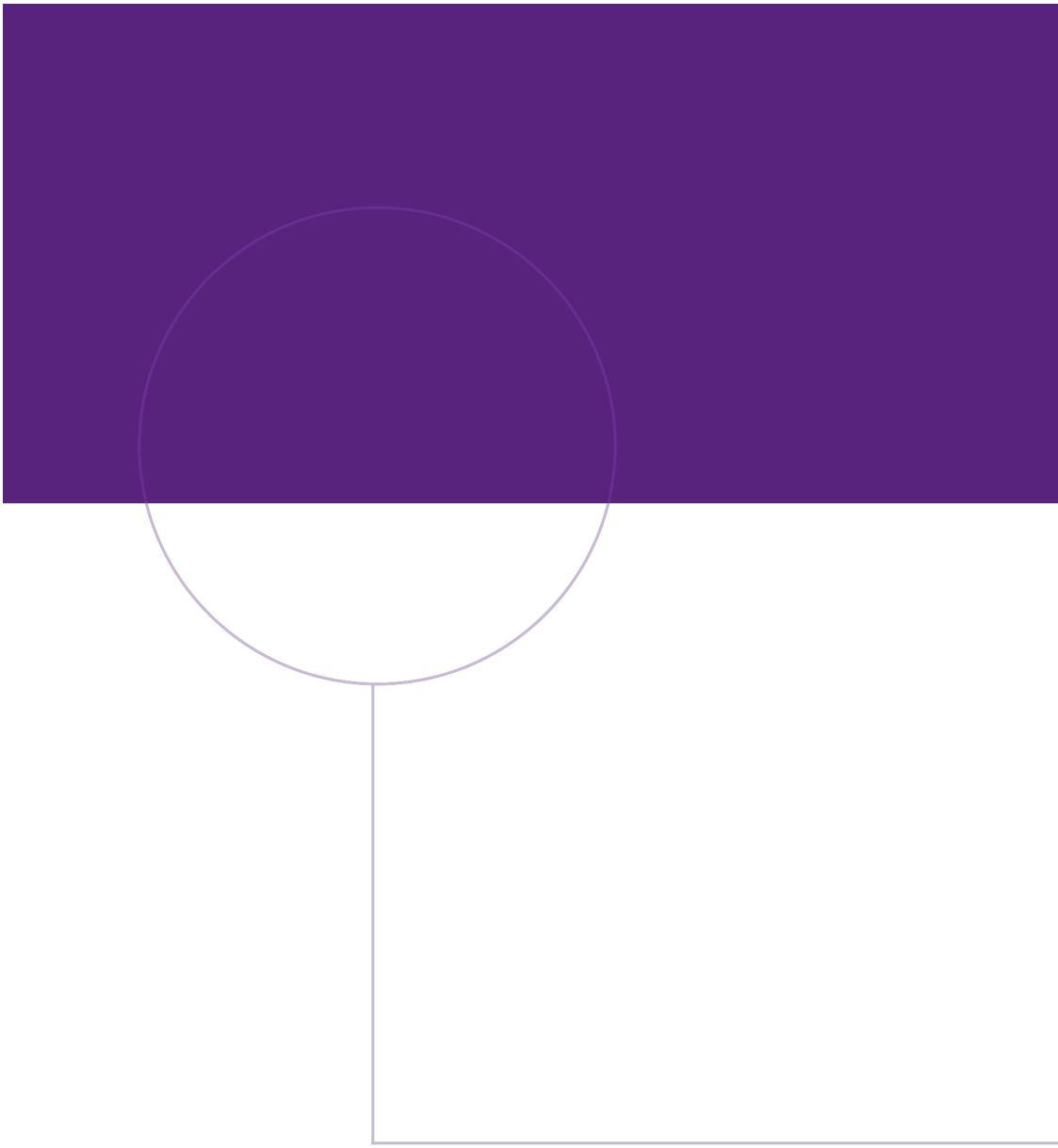

NTNU

Norwegian University of
Science and Technology